2017-07-01

Fundamental Studies and Applications of Ambient Plasma Ionization Sources for Mass Spectrometry

Wade C. Ellis
Brigham Young University

Fundamental Studies and Applications of Ambient Plasma Ionization Sources for Mass Spectrometry

Wade C. Ellis

A dissertation submitted to the faculty of
Brigham Young University
in partial fulfillment of the requirements for the degree of

Doctor of Philosophy

Paul Burton Farnsworth, Chair
Daniel E. Austin
David V. Dearden
Jaron C. Hansen
Eric T. Sevy

Department of Chemistry and Biochemistry

Brigham Young University

ABSTRACT

Fundamental Studies and Applications of Ambient Plasma
Ionization Sources for Mass Spectrometry

Wade C. Ellis
Department of Chemistry and Biochemistry, BYU
Doctor of Philosophy

The field of ambient desorption/ionization mass spectrometry (ADI-MS) has existed for over a decade. ADI-MS is a technique that offers benefits including fast analysis time, simple ionization sources that are easily constructed, and little to no required sample preparation. The research presented here describes efforts to better understand plasma-based ADI-MS sources and to explore the use of hydrogen-doped plasma gases with these sources. The use of hydrogen-doped argon (H_2/Ar) and hydrogen-doped helium (H_2/He) as plasma gases for a dielectric barrier discharge (DBD) and an AC glow discharge is presented first. When using the DBD, the intensity of the signal obtained when analyzing organic molecules in positive ion mode was increased by factors up to 37 times. In negative ion mode, only H_2/Ar was shown to enhance the signal of an organic analyte. The limits of detection for caffeine when using hydrogen-doped plasma gases were found to decrease by factors of 78 and 1.9 for H_2/Ar and H_2/He respectively. The same phenomenon was observed when using H_2/Ar with the AC discharge, but no signal enhancement was observed when using hydrogen-doped helium with the AC discharge. Similarly, if the DBD was allowed to ground through a wire rather than through the air, no signal enhancement was observed for H_2/He. Using H_2/Ar with metal samples is presented second. By using the metal sample as the grounded electrode for the AC glow discharge, many different metals could be detected directly with a time-of-flight mass spectrometer (TOF-MS) in the form of atomic ions both on their own and in combination with water and ammonia from the discharge. Any refractory metals tested did not yield signal. In addition to direct analysis with a TOF-MS, the AC discharge was used as a sampling method for an inductively coupled plasma mass spectrometer (ICP-MS). When coupled with an ICP-MS, the AC glow discharge was found capable of sampling even refractory elements, though the power of the ICP was required for ionization and detection. Scanning electron microscope (SEM) images of a copper surface exposed to the plasma discharge showed signs of melting when using the H_2/Ar. Finally, a computer simulation of the chemistry and flow dynamics of a DC glow discharge generated in helium is presented. The simulation explores many of the fundamental processes at work and how they depend on the composition of the plasma gas. The generation of important species in the plasma was found to depend more on the amount of N_2 and H_2O impurities in the plasma gas rather than on the humidity or air pressure.

Keywords: ambient desorption/ionization, mass spectrometry, inductively coupled plasma, glow discharge, dielectric barrier discharge, hydrogen doping, computer simulation, metal sampling

ACKNOWLEDGEMENTS

I gratefully acknowledge the mentorship of my advisor, Paul Farnsworth, as well as the support of my coworkers in the Farnsworth Lab. I thank the members of my graduate committee for their time and attention. I thank Ross Spencer for the many hours he spent helping in the development of the computer simulation that I describe in this work. I especially thank my wife, Terra, for her support and encouragement throughout my education.

Funding for the research described in this dissertation was provided principally by the Department of Chemistry and Biochemistry at Brigham Young University. My personal financial support was provided through two fellowships. For the first three years of my graduate work, I was a recipient of the High Impact Doctoral Research Assistantship administered by Graduate Studies at BYU. For my last year of study, I was awarded the Charles E. and Margaret P. Maw Fellowship by the Department of Chemistry and Biochemistry at BYU. These invaluable sources of support have made getting my education possible in an expedited time frame.

TABLE OF CONTENTS

ABSTRACT ii
ACKNOWLEDGEMENTS iii
TABLE OF CONTENTS iv
LIST OF TABLES vii
LIST OF FIGURES viii
1 Introduction 1
1.1 Chemical Analysis Using Ambient Plasma Discharges 1
1.1.1 Ambient Desorption/Ionization 1
1.1.1.1 Solvent Based Ambient Desorption/Ionization 1
1.1.1.2 Plasma Based Ambient Desorption/Ionization Sources 3
1.1.1.2.1 Direct Analysis in Real Time 3
1.1.1.2.2 Flowing Atmospheric Pressure Afterglow 4
1.1.1.2.3 Dielectric Barrier Discharges 5
1.1.1.2.4 Other Plasma Based ADI Sources 5
1.1.2 Characterization of Plasma Based ADI Sources 6
1.1.2.1 Optical Spectroscopic Characterization 7
1.1.2.2 Mass Spectrometric Characterization 13
1.1.2.3 Computational Characterization 16
1.2 Elemental Analysis Using Plasma Discharges 18
1.2.1 Inductively Coupled Plasma 19
1.2.2 Glow Discharges 20
1.2.3 Laser Induced Breakdown Spectroscopy 20
1.2.4 Solution Cathode Glow Discharges 21
1.3 My Research Focus 22
1.4 References 22
2 The Effects of Added Hydrogen on Ambient Helium and Argon Discharges Used for Mass Spectrometry 27
2.1 Using Hydrogen Doped Plasma Gases in ADI-MS 27
2.2 Experimental Setup 29
2.2.1 Chemicals Tested 29
2.2.2 Discharge Sources 29

2.2.3 Mass Spectrometer Setup 31
2.3 Signal Enhancement with Added Hydrogen 33
2.3.1 Optimal Amount of Hydrogen in Argon 33
2.3.2 Coated Slides 34
2.3.2.1 Limit of Detection 36
2.3.2.2 Sample Area vs Sensitivity 36
2.3.2.3 Changes to the Desorption Mechanism 38
2.3.3 Gas Phase Analyte 39
2.4 Background Ion Mass Spectra 42
2.5 Potential Changes to Ionization Mechanism 43
2.6 Conclusions 44
2.7 References 44
3 Metal Sampling Using Ambient Plasma Discharges 47
3.1 Sampling Solid Metals at Atmospheric Pressure by Plasma Discharge 47
3.2 Experimental 48
3.2.1 Glow Discharge 48
3.2.2 Dielectric Barrier Discharge 49
3.2.3 Time-of-Flight Mass Spectrometer Set Up 50
3.2.4 Metal Samples 50
3.2.5 Inductively Coupled Plasma Mass Spectrometer Set Up 52
3.2.6 Scanning Electron Microscope Images 53
3.3 Results and Discussion 53
3.3.1 Detectable Metals 53
3.3.2 Effects of Changing the Percent Hydrogen in Argon 56
3.3.3 ICP-MS Analysis with the Glow Discharge 57
3.3.4 ICP-MS Analysis using the Dielectric Barrier Discharge 58
3.3.5 Sampling Mechanism Changes 59
3.3.6 Classification of Brass Samples 63
3.4 Conclusions 64
3.5 References 65
4 Computer Model of a DC Glow Discharge Used for ADI-MS 67
4.1 Scope of the Simulation 67
4.2 Experimental 68

4.2.1 DC Discharge 68
4.2.2 Software and Simulation Conditions 69
4.3 Theory 70
4.4 Results and Discussion 75
4.4.1 Experimental Measurements of the Helium Metastable Atoms Densities 75
4.4.2 Simulation Results 76
4.4.3 The Role of Impurities in the Plasma Gas 80
4.4.4 The Effect of Changing Relative Humidity 83
4.4.5 The Effect of Changing Air Pressure 84
4.5 Conclusions 85
4.6 References 86
5 Future Work 87
5.1 Future Directions for the Work Described 87
5.2 The Future of Ambient Desorption/Ionization Mass Spectrometry 88
5.3 References 88
6 Appendix: DC Discharge Simulation Matlab Code 89
6.1 DC Discharge Simulation Matlab Code 89
6.1.1 Main Script 89
6.1.2 Functions 97
6.1.2.1 Smoother 97
6.1.2.2 DiffusionTemp 100
6.1.2.3 Leftedge 101
6.1.2.4 S0res 103
6.1.2.5 CDoperator 104
6.1.2.6 Implicitsolverres 107
6.1.2.7 ImplicitsolverS0 113

LIST OF TABLES

Table 3-1 55
Table 4-1 73

LIST OF FIGURES

Figure 2-1 30
Figure 2-2 32
Figure 2-3 35
Figure 2-4 37
Figure 2-5 40
Figure 3-1 49
Figure 3-2 52
Figure 3-3 57
Figure 3-4 60
Figure 3-5 61
Figure 3-6 63
Figure 4-1 69
Figure 4-2 76
Figure 4-3 77
Figure 4-4 77
Figure 4-5 79
Figure 4-6 80
Figure 4-7 81
Figure 4-8 84

1 INTRODUCTION

1.1 Chemical Analysis Using Ambient Plasma Discharges

1.1.1 Ambient Desorption/Ionization

Since the first introductions of desorption electrospray ionization (DESI)[1] and direct analysis in real time (DART)[2] in 2004 and 2005 respectively, ambient desorption/ionization (ADI) sources for mass spectrometry have become integral parts of the mass spectrometry toolbox for analyzing organic molecules under atmospheric conditions. Generally speaking, these sources are able to perform analyses quickly and with little to no sample preparation.[3] They are also simple to construct and fairly small, making some of them suitable for field-based studies when coupled with miniature mass spectrometers.[4, 5] The main mechanism of operation for an ADI source is that energetic or reactive ions, atoms, or molecules are directed towards a surface such that the desired analyte is desorbed off the surface into the gas phase and subsequently ionized by the same stream of reactive species. The methods for generating the reactive species include generating an electrospray from a solvent or solvent mixture or igniting a plasma discharge. These two methods will be described in detail below.

1.1.1.1 Solvent Based Ambient Desorption/Ionization

DESI, the first solvent based ADI source, utilizes an electrospray ionization (ESI) source to both desorb analyte from a surface and ionize it. An ESI sprayer is pointed at a surface that

contains or is coated with the desired analyte and is placed near a mass spectrometer inlet. The capillary through which the ESI solvent is flowed resides in a second, larger capillary. The larger capillary allows for the flow of an inert gas—usually N_2—that gives sufficient energy to the droplets emitted by the ESI source to remove analyte from the surface. The important factors for positioning the sprayer include the angle it makes with the surface under study, the distance from the sprayer tip to the surface, the distance from the sprayer to the mass spectrometer inlet, the solvent used to form the electrospray, and the voltage applied to the solvent. These parameters have been studied in detail.[6] An important use for DESI has been in performing mass spectral imaging of surfaces. Images are formed by rastering the sprayer across a surface while collecting mass spectra. This technique has been applied mostly to biological samples—including both animal tissue and plant foliage—to detect the distribution of proteins, lipids, pharmaceuticals, and other important compounds.[6-9] The resolution of the images produced using DESI is typically tens to hundreds of μm per pixel. Although resolution with DESI imaging is not as good as that obtained using other imaging techniques, it is still adequate to provide useful information about the systems studied with the added benefit of performing the analysis under ambient conditions. In addition to imaging applications, DESI has been used for quantitative and qualitative analyses of surfaces without any rastering.

The mechanism of operation for DESI has been described as small microjets ejected from the surface caused by high velocity impact of primary droplets from the sprayer[10] and as the formation of ions in rivulets extending away from the main solvent area.[11]

A daughter technique to DESI is nanoDESI. For nanoDESI, solvent is delivered to the sample surface through a small capillary where it forms a small drop and dissolves chemicals from the surface. A second capillary is placed in the drop on the surface and the analyte-

containing solution is drawn up by capillary action. The end of the second capillary is placed near the mass spectrometer inlet where a nanospray is formed due to a high potential applied to the system, and ions are generated. The change in configuration results in several improvements to the technique including increased resolution, decreased solvent consumption, and increased sensitivity.[12]

1.1.1.2 Plasma Based Ambient Desorption/Ionization Sources

The second method for generating excited species is the formation of a plasma discharge. Generally, two electrodes are needed to form a discharge. High voltage is applied to one while the other is held at ground, resulting in the formation of plasma composed of the ionized gas between the electrodes. Gas is often flowed through the space between the electrodes to carry the generated excited species toward the sample surface. Plasma-based ADI sources, when compared to other ionization sources such as atmospheric pressure chemical ionization (APCI) or ESI, have been found to be best at ionizing both polar and nonpolar molecules that have fairly low molecular weights.[13] Several different plasma discharges have been used with a wide variety of geometries and plasma gases. Some of these are described in detail below.

1.1.1.2.1 Direct Analysis in Real Time

The first plasma discharge based ADI source that appeared in the literature was the DART. The main component of the DART source is a plasma discharge formed between two electrodes as helium gas is flowed through the electrode area. A DC potential is applied to one of the electrodes at a few hundred volts and current is limited to about 5 mA. The other electrode is held at ground, making a glow discharge. Following the active discharge region are two other electrodes designed to remove electrons from the gas stream to prevent the loss of

reactive species due to recombination. Also included downstream from the active discharge is a gas heater that can be used to enhance thermal desorption of analyte from the sample surface..[2] The initial publications by the inventors of the DART reported that a wide variety of compounds—from explosives to pharmaceuticals—could be desorbed and ionized by DART and subsequently detected by a mass spectrometer. They attributed the ionization to the formation of excited helium metastable state atoms by the plasma discharge and their direct interaction with the analyte or species in the air such as oxygen and nitrogen.[2, 14]

DART is the only plasma-based ADI source that has been successfully commercialized to date. It has found a place in a variety of applications including food safety,[15] counterfeit pharmaceutical identification,[16] plant species identification,[17] and as an ion source for ion mobility spectrometry.[18]

1.1.1.2.2 Flowing Atmospheric Pressure Afterglow

The flowing atmospheric pressure afterglow (FAPA) was designed in the Hieftje lab at Indiana University.[19] Like the DART, it is a DC glow discharge. However, it is typically operated at a current of around 25 mA rather than the 5 mA used in the DART source. The FAPA has been experimented with in many ways, including changing its electrode geometry,[20] the method of sample introduction,[20, 21] and the continuity of the gas flow.[22, 23] However, in most regards it operates in a very similar way to DART. In addition to the uses found for the DART, the FAPA has also been shown to detect counterfeit electrical components.[24]

1.1.1.2.3 Dielectric Barrier Discharges

Dielectric barrier discharges (DBD) are commonly used as ADI sources but have a different electrode configuration than FAPA or DART. For a DBD, the electrode to which alternating current (AC) is applied is separated from the ground electrode by a dielectric barrier that prevents current from flowing directly between the two electrodes. DBDs come in several electrode configurations. Notable ones include coating one electrode with glass, separating the two electrodes by a sheet of glass, having one electrode inside a glass tube and the other outside the tube, having both electrodes outside the glass tube, and having a single electrode on the outside of a glass tube. In the last case where there is no ground electrode, the environment surrounding the discharge serves as the ground, and the discharge may ground through the air or through a nearby metal object. For DBDs that utilize a glass tube as the dielectric, it is common for a plume of plasma to extend beyond the tip of the glass tube. This configuration is the one most commonly used in ADI-MS. The plasma plume is allowed to interact with the surface under study to perform desorption and ionization.

The two most notable ADI sources that are DBDs include the low temperature plasma (LTP)[25] and the dielectric barrier discharge ionization (DBDI).[26] These two DBDs differ from one another primarily in the diameter of the glass tube used and in the frequency and voltage of the applied voltage, although the names are sometimes used interchangeably.

1.1.1.2.4 Other Plasma Based ADI Sources

Due to the large range of conditions under which a plasma discharge can be ignited, a large number of sources have been developed and named. Generally speaking, most are adaptations of the four sources already cited. One notable example includes the plasma assisted

desorption ionization (PADI) source.[27] It is a corona discharge operated at a lower current than either the DART or the FAPA.

1.1.2 Characterization of Plasma Based ADI Sources

As ADI sources have been developed, a great deal of fundamental research has been done to determine what mechanisms drive the formation of the ions detected by the mass spectrometer. The mechanism of operation was initially theorized to be similar to that of atmospheric pressure chemical ionization (APCI) sources.[28] For APCI sources, the main mechanism for formation of protonated analyte ions ($[M+H]^+$) begins with the formation of excited state helium atoms (He_m) in the discharge and continues as follows. M represents the analyte molecule.

$$He_m + N_2 \rightarrow {N_2}^+ + He + e^- \quad (1\text{-}1)$$

$$2N_2 + {N_2}^+ \rightarrow {N_4}^+ + N_2 \quad (1\text{-}2)$$

$${N_4}^+ + H_2O \rightarrow H_2O^+ + 2N_2 \quad (1\text{-}3)$$

$$H_2O^+ + H_2O \rightarrow H_3O^+ + OH \quad (1\text{-}4)$$

$$H_3O^+ + H_2O \rightarrow H{(H_2O)_2}^+ \quad (1\text{-}5)$$

$$H{(H_2O)_n}^+ + H_2O \rightarrow H{(H_2O)_{n+1}}^+ \quad (1\text{-}6)$$

$$H{(H_2O)_n}^+ + M \rightarrow [M+H]^+ + (H_2O)_n \quad (1\text{-}7)$$

The series of reactions indicates that the main energy carrier is a helium metastable state atom. Those atoms interact with nitrogen and water from the air to ultimately generate the $[M+H]^+$ ions detected by a mass spectrometer. However, this mechanism is obviously incomplete considering that it is not uncommon to observe molecular ions (M^+) in the mass spectra. Also, the mechanism does not take into account any reactions involving O_2, which is

present in significant amounts in air. One of the goals of fundamental research in this field is to validate and expand upon this reaction mechanism to thoroughly describe all the ionization processes that occur. The research entails looking for the atoms and ions included in the mechanism and also exploring side reactions that can occur along with their implications. Experiments to characterize the sources generally use one or more of three methods: optical spectroscopy, mass spectrometry, or computer simulation. Each type of experiment has yielded important insight into how ions are formed.

1.1.2.1 Optical Spectroscopic Characterization

Various spectroscopic techniques, including emission, fluorescence, and absorbance have been used to measure the abundances of species of interest in helium plasma discharges.

For the FAPA, Shelley et al. conducted a fairly comprehensive study monitoring the spatial distribution of selected species in the plasma discharge using emission spectroscopy.[29] The emission was monitored between the pin and plate electrodes and in the afterglow region for various flow rates of helium as well as several discharge voltages. Emission was detected from species that are listed in equations 1-1 to 1-7 in the active discharge region between the electrodes. These included helium, N_2, N_2^+, and hydroxyl radicals ($OH^{\cdot}$). Other species detected included oxygen atoms, hydrogen atoms, He_2 molecules, CO^+ ions, and NO molecules. In the afterglow, emission was detected only from $OH^{\cdot}$ and N_2^+. Using the rotational temperatures of the OH radicals and the N_2 molecules, the measured temperature in the active discharge region was approximately 1100 K at the pin electrode; whereas the temperature in the afterglow region was on average around 500 K. Increases in the discharge current increased the densities of species in the active discharge region significantly. As the flow rate of the helium plasma gas

was increased, significant increases in emission were measured in the afterglow region of the discharge. However, all measurements in this study were only qualitative. No quantitative values could be assigned from the data. Also, no conclusions were drawn about the validity of the proposed mechanism for ion formation because no analytes were introduced as part of this study.

Several other studies of similar plasma sources have actively attempted to test the proposed mechanism of reaction spectroscopically. These include a study that employed both laser induced fluorescence and emission measurements to measure the temporal and spatial locations of helium metastable atoms, N_2, and N_2^+ in a DBD[30] and two studies that utilized emission measurements to determine the spatial distributions of important species in the LTP using both helium and argon as plasma gases.[31, 32] For helium as the plasma gas, the predominant emission lines from the LTP were attributed to He, N_2, N_2^+, OH, O, and H, similar to what was found in the helium FAPA. These lines were found to decrease in intensity when water was added to the plasma gas, suggesting that water reacts with species generated in the plasma. When pure argon was used as the plasma gas, the main emission was from Ar, with only weak emission being observed from OH and nitrogen containing species. One significant difference in what was proposed in the studies using the LTP compared to the APCI mechanism cited above was that the authors attributed the generation of N_2^+ ions predominantly to charge transfer reactions between N_2 and He_2^+ ions rather than the Penning ionization between helium metastable atoms and N_2 that is shown in equation 1-1.

In the paper that used the DBD, Heywood et al. monitored both the spatial and temporal distributions of He_m using laser induced fluorescence. The plasma was found to be discontinuous. It operated by emitting bullets of plasma that propagated faster than the flow of

the plasma gas. The He_m fluorescence measurements were then compared to emission from N_2^+ ions and N_2 molecules. The spatial distributions of the fluorescence and emission signals showed a decrease in the helium metastable atom fluorescence as the emission from the N_2^+ increased and a subsequent decrease in the N_2^+ emission as the N_2 emission increased. This sequence suggested that a significant reason for the decrease in helium fluorescence was a reaction of helium with N_2 from the air such as is described in equation 1-1 above. The following emission signal from N_2 could then be attributed to reactions of N_2^+ with other species in the air including other N_2 molecules, water, or perhaps something else that neutralized the charge of N_2^+ through charge transfer. The major conclusion from this study was that Penning ionization does play an important role in the ionization mechanism involved in plasma based ADI sources. The addition of hydrogen gas to the helium DBD was shown to effectively quench the helium metastable atoms while increasing the number of analyte ions generated. This was observed by analyzing caffeine deposited on a glass slide. The analysis when using hydrogen-doped helium yielded signals that were more intense than with pure helium.

In another study,[33] the absolute number density of helium metastable atoms was measured using absorption spectroscopy for four types of plasma based ADI sources: a DBD, an LTP, an AC glow discharge, and a DC glow discharge. The DC glow discharge used was similar to the FAPA in terms of voltage and current settings. The measurements taken were time averaged over many cycles of the alternating current for the DBD, LTP, and AC discharge. The number densities for the four discharges were in the range of 1.39×10^{12} cm^{-3} for a point 1 mm downstream from the end of the capillary in the DBD to 1.11×10^{10} cm^{-3} for the same measurement for the LTP. For the glow discharge sources, no significant numbers of helium metastable atoms were detected downstream from the grounded plate electrode. When

comparing the densities of helium metastable atoms to those of atmospheric species such as nitrogen, oxygen, and water at atmospheric pressure, it is clear that the helium metastable atoms are the limiting reactant for the formation of analyte ions. For example, at 30 % relative humidity, the number density of water in air is approximately 2.4×10^{17} cm^{-3} with the number densities of oxygen and nitrogen being 1 to 2 orders of magnitude higher than that. The large difference in number densities between helium metastable atoms and other species in the air implies that the ability of a discharge source to ionize analyte particles depends principally on its ability to generate helium metastable atoms. Understanding the way they are generated or finding a way to more effectively utilize them to ionize analyte particles is essential for developing a more effective and efficient plasma ADI source.

Other spectroscopic studies focused more on the temporal behavior of plasma discharges rather than searching for any particular species. In particular, the work of Joachim Franzke and coworkers has explored this behavior. For instance, they studied how different voltage settings can change the mode of operation of a DBD from a homogeneous discharge to a filamentary one,[34] as well as the implications of those modes on the performance of the DBD as an ionization source.[35] The change in discharge mode from homogeneous to filamentary at higher applied voltages was found to increase the number density of excited helium species as well as excited nitrogen and nitrogen ions, but only in the discharge region upstream from the tip of the glass capillary used to form the discharge. Downstream number densities of excited species in filamentary mode were found to be the same or lower than those in homogeneous mode. The study correlating these operation modes to mass spectrometric performance found that the filamentary mode gives much poorer signal intensity than the homogeneous mode. The

differences in signal intensity were attributed to differences in electron number density and the densities of other species in the discharge.

Another study from the Franzke lab monitored the evolution of the emission signals for important species in a DBD with respect to time and space.[36] By monitoring the current along with the emission signals, they were able to correlate the two. They found that there were two current spikes per cycle of the applied voltage. The first, which they called the displacement current, sent a wave of plasma in both the upstream and downstream directions from the high voltage electrode. The initial current was followed by the discharge current which coincided with a jet of plasma travelling from the grounded electrode upstream towards the exit of the capillary tube and into the open air. These plasma bursts, or bullets, were found to travel at over 65 km per second. Although plasma bullets had been observed previously in DBD sources,[30, 37-39] the authors were also able to monitor the dissociation of a model analyte in the plasma by doping the helium gas with a few ppm of $CHClF_2$. By monitoring emission from fluoride, they were able to determine that the $CHClF_2$ was ionized during both current spikes but only fragmented during the discharge current portion of the cycle. The displacement current generates a "softer" plasma that is not powerful enough to break covalent bonds, but the discharge current has more power such that fragmentation is possible. Furthermore, they found that by lowering the applied voltage, they could prevent the discharge current spike from occurring and turn the DBD into a softer source more appropriate for use in molecular mass spectrometry. However, if elemental analysis was to be performed, the voltage could be increased to cause the second, more powerful discharge to ignite with each cycle of the voltage and cause dissociation.

Finally, the role of impurities on the chemistry of the discharge was investigated.[40] The role of nitrogen as an impurity—whether from impurities in the gas cylinder or from the atmosphere—in helium discharges was explored. According to equation 1-1 above, nitrogen from any source is an important intermediate for ionizing analyte molecules. It is possible for a helium discharge to ionize nitrogen due to the high energy of the helium metastable atom compared to the ionization energy of nitrogen. The internal energy of a helium metastable atom is 19.81 eV, compared to the ionization potential of N_2 (15.581 eV), so Penning ionization is favored energetically. However, in an argon discharge, the argon metastable atoms do not have enough energy, 11.54 eV, to ionize nitrogen. The Franzke group found that adding a small amount of propane (ionization energy: 10.94 eV) to the argon reduced the required operating voltage for the DBD to a range similar to that required for helium. This implied that the propane in effect took on the role of nitrogen as the main species to which energy could be transferred from the metastable atoms generated in the plasma. In addition, they found that as more nitrogen was added to helium, the plasma transitions to have more properties of a nitrogen plasma. The emission from helium species and nitrogen ions decreases while the emission from nitrogen molecules increases.

As can be seen, spectroscopy has provided many important insights into the use and mechanism of reaction that occur in ambient plasma discharges. However, there are many important aspects of the chemistry in these discharges that cannot be observed easily using spectroscopic techniques. In particular, most water-containing species do not emit light outside the infrared range of the electromagnetic spectrum. As these types of species are thought to be important for the formation of analyte ions, many studies have utilized mass spectrometry to detect water containing species.

1.1.2.2 Mass Spectrometric Characterization

There are two main ways of characterizing ADI sources with mass spectrometry. First, by directing a discharge towards the inlet of the mass spectrometer while introducing an analyte, one can investigate the type of analyte ions formed as well as the efficiency of the source. Second, a discharge can be directed at the mass spectrometer inlet without an analyte present to take a look at reagent ions, such as protonated water clusters ($H(H_2O)_n^+$) to determine their relative abundances.

A 2012 study compared the ionization ability of the LTP to ESI and APCI.[13] The authors reported that the LTP is better able to ionize and detect lower mass, nonpolar molecules than either ESI or APCI. However, the LTP was unable to detect ionic compounds like an ESI source could. Also, the range of molecular masses that an LTP source can ionize is fairly limited compared to both APCI and ESI. The sources are complementary to each other. They each have important applications for which they are nicely suited.

In two papers, Newsome et al.[41, 42] examined the effects of humidity on the ionization behavior of the DART. An enclosure was built around the inlet of the mass spectrometer into which the DART could be inserted. A probe was used to measure the humidity inside the enclosure, and the humidity was controlled using a test atmosphere generator. The test analyte used was hexamethylene triperoxide diamine (HTMD), a pressure sensitive explosive. Changes in humidity primarily affected source "hardness." As the humidity was decreased, the ratio of a key fragment peak to the $[M+H]^+$ peak of HTMD increased. Conversely, as the humidity was increased, the ratio decreased. The reason for this change in fragmentation could be attributed to changes in the relative abundances of $H(H_2O)_n^+$ and N_2^+. The protonation reaction with $H(H_2O)_n^+$ is low energy. It does not have much potential to break bonds due to the relatively

high proton affinity of water clusters. However, a charge transfer reaction with N_2^+ can result in a less stable ion that is more prone to fragmentation. So, reducing the humidity increases the abundance of N_2^+, which suggests that it is an important precursor to $H(H_2O)_n^+$ in a helium based discharge.

Several other studies have used mass spectrometry to measure the relative amounts of protonated water cluster ions and other species in the downstream regions of atmospheric plasma discharges. Three studies in particular did this with the FAPA[43, 44] and with a variant of the DBD.[45] In the FAPA, a series of protonated water cluster ions were found including H_3O^+ $H(H_2O)_2^+$, $H(H_2O)_3^+$, $H(H_2O)_4^+$, and $H(H_2O)_5^+$. However, the two studies differed on the relative abundances of these ions. One listed the n=2 water cluster ion as the most abundant whereas the second listed the n=3 ion as the most abundant. Other notable ions detected using the FAPA included O_2^+, NO^+, O_3^+, N_2^+, and CO_2^+. In addition to these ions, many other ions were detected that were attributed to species from the laboratory air that were ionized by the discharge. These included common solvents such as acetone, ethyl acetate, and acetonitrile as well as ubiquitous polyethers and polymers such as phthalate esters, polyethylene glycol, and common plasticizers. The detection of these molecules from the air highlights one of the difficulties of this type of mass spectrometry. It is essentially impossible to perform an analysis with an ambient plasma discharge without encountering these interfering peaks from ubiquitous contaminants. They can significantly complicate the interpretation of mass spectra if the analyte has a peak or peaks in the area of a contaminant ion peak. The study on the DBD showed many similar ions to those found in the FAPA, including the protonated water clusters, N_2^+, O_2^+, and O_3^+, but also showed cluster ions with the formula $O_3(H_2O)_n^+$ with n = 1 and 2. In all three cases, the relative abundances of each ion depended greatly on the power applied to the discharge as well as the

flow rate of the plasma gas and the distance from the discharge exit to the mass spectrometer inlet.

The effect of interfering ionization pathways has also been examined.[46] Shelley and coworkers observed ionization suppression of $[M+H]^+$ ions forming analytes based on relative proton affinities. This was done using the FAPA, DART and LTP by introducing gas phase methyl salicylate as a test analyte. When a small amount of a matrix species that had a larger proton affinity than methyl salicylate was introduced as a matrix into the analyte gas stream, the signal from the $[M+H]^+$ peak of methyl salicylate became less intense while the signal from the interfering analyte increased. Test matrices included naphthalene, acetophenone, and triethyl phosphate. The implications of these results are that the ability of an ADI discharge to ionize an analyte depends directly on the proton affinity of the analyte. Also, when analyzing mixtures of molecules, it is essential to take into account the potential for ionization suppression of the analytes with the lowest proton affinities.

Researchers in the Farnsworth lab reported that the signal intensity for analytes can be improved greatly by the addition of a small amount of hydrogen gas into the helium plasma gas when using a DBD.[30, 47] Signal enhancements of up to 68 times were seen for test analytes including caffeine, anthracene, diphenylamine, and coumarin 460. The ideal amount of hydrogen addition was found to be 0.9 % in helium. The enhancement was observed without a corresponding increase in the signal of background ions such as those from the lab air.

These mass spectrometric studies furthered the understanding of what happens in an ambient plasma discharge. As expected, protonated water cluster ions were abundant in large numbers. The presence of side reactions was also confirmed by the detection of ions such as O_2^+, O_3^+, CO_2^+, and others. It is apparent that the chemistry involved in these sources is complex

and warrants further study. The final principle method for doing this type of fundamental study of ambient plasmas is developing computer simulations.

1.1.2.3 Computational Characterization

One of the major drawbacks to using mass spectrometry to detect the background reagent ions in an ADI plasma discharge is that the ions detected as well as the measured relative abundances of those ions do not always provide a good picture of what actually happens in the discharge. Before reaching the mass analyzer of a mass spectrometer, ions often must first pass through a heated capillary inlet, several vacuum chambers, and layers of ion optics. This introduces the possibility of reactions occurring that would change the ion distribution. For instance, the size of the protonated water clusters may change when they are heated or cooled before being analyzed. Some ions that are particularly unstable, such as N_4^+, may not even reach the mass analyzer before decomposing. Many of these ions are also not detectable using optical spectroscopic means, so they essentially cannot be detected reliably using experimental methods. Although mass spectrometry and optical spectroscopy are still useful techniques for doing this type of analysis, it is beneficial to get a snapshot of what is happening in the active discharge region based on kinetics and flow dynamics using computer models.

The Bogaerts group in Antwerp simulated the reactions that happen in the active discharge region of a FAPA source.[48] A Monte Carlo simulation was used to model the random collisions of electrons with helium in the gas to form helium metastable atoms and other species, including atomic helium ions (He^+), molecular helium ions (He_2^+), and helium excimers (He_2^*). Those species were then tracked using kinetic rate equations to model the reactions with N_2 to form N_2^+ and N_4^+. In total, 21 different reactions were monitored. The results showed that most

of the helium that was excited existed in the metastable state, but that significant populations existed as He_2^+. The calculations indicated that 77 % of the N_2^+ was generated by charge transfer reactions between He_2^+ and N_2, while only 13 % and 9 % of the production of N_2^+ was due to Penning ionization from collisions with He_m and He_2^* respectively. The remaining N_2^+ generation was attributed to the decomposition of N_4^+. The majority of the N_2^+ was removed by recombination with electrons, and only a small portion reacted further to become N_4^+. It may be inferred that since the simulation did not include any water or water containing species that the inclusion of alternate reaction pathways of N_2^+ and N_4^+ with water to ultimately make protonated water clusters would have a significant influence on the populations of all the species involved. However, this study did make effective predictions that coupled the generation of helium species in the discharge to the ionization of N_2, which has been shown before to be a key process in the plasma chemistry.

In another simulation from the Bogaerts group, a direct current discharge using 1% H_2 in Ar was simulated.[49] This type of discharge is used as a sputtering device. The addition of H_2 was done with the intent of changing the sputtering characteristics, but has significant implications for any H_2 doped ADI source. They found that the Ar^+ ions generated from the plasma discharge reacted efficiently with H_2 molecules to form species such as ArH^+, H, H_2^+, and H_3^+. However, the argon metastable atom was the only particle that was capable of ionizing copper atoms sputtered from the target.

A final simulation by Karakas and coworkers modeled the propagation of plasma bullets in a DBD as a function of helium mole fraction.[37] Experimental results indicated that the length of the plume on a DBD depends largely on the flow rate of the helium and the applied voltage. These results were validated in the simulation. As the velocity of the helium gas increases, the

mole fraction of helium downstream from the exit of the DBD discharge tube increases. The increase in the mole fraction corresponded to a longer plasma bullet. The plasma bullet requires a minimum amount of helium to propagate through the air. However, as the applied voltage was increased, the required mole fraction of helium decreased. This effect was attributed to the increase in the power channeled into the plasma, allowing the bullet to propagate further in the air.

Each of the above mentioned studies has contributed significant new insights into the behavior of a plasma discharge in its native state without probing it with light or looking at what species survive the passage through a mass spectrometer. Although there is certainly more to be done to understand the fundamental operation modes of ADI sources, results to date have been largely successful.

1.2 Elemental Analysis Using Plasma Discharges

Elemental analysis is the measurement of the amount of each element present in a given sample. A number of different types of plasma discharge have been used to perform elemental analysis. The most widely used techniques that utilize a discharge for elemental analysis include the inductively coupled plasma (ICP), glow discharges (GD), and laser induced breakdown spectroscopy (LIBS). More recently, a few groups have experimented with plasma discharges that do elemental analysis using an aqueous solution as the cathode of a glow discharge. The use of each method includes several benefits and disadvantages, but all have proven useful.

1.2.1 Inductively Coupled Plasma

The inductively coupled plasma (ICP) is the gold standard for trace elemental analysis. It has been in existence for many decades.[50] The basic principle of operation is that a high-power argon plasma discharge is generated in a glass torch composed of three concentric channels. Starting with the central channel, the channels are for nebulizer flow, intermediate flow, and outer flow respectively. The high voltage alternating current is applied via a copper coil wrapped around the outside of the torch. Samples are typically introduced by nebulizing aqueous solutions.[51] The fine aerosol generated by a nebulizer is carried into the plasma by flowing argon through the central channel. However, it is also possible to sample solid samples using laser ablation,[52] although the use of laser ablation is not as common as solution nebulization. Detection for the ICP is achieved using either an optical emission spectrometer or a mass spectrometer. To achieve the lowest possible limits of detection, a mass spectrometer must be used as the detector. Limits of detection for some elements can be in the parts per quadrillion range.

One of the major challenges when using ICP is sampling solids. Converting a solid into a solution requires extensive sample preparation involving steps such as acid digestion, serial dilution, and filtering. Each step is time consuming and has the potential of contaminating the sample or causing sample loss. If laser ablation is used to directly sample a solid, a high-power laser system is required. Such a system can be cost prohibitive and requires additional personal protective equipment or engineering controls for the user to avoid exposure to intense laser light. In addition, both solution nebulization and laser ablation sampling methods consume the sample or at the very least damage it significantly.

1.2.2 Glow Discharges

Glow discharges are often employed in applications where material is to be removed from one surface and deposited on another. This process is known as sputtering.[53] If instead of depositing the material on another surface it is directed into a mass spectrometer, elemental analysis can be performed. The essential configuration of a glow discharge includes a high voltage electrode and a grounded sample that serves as the counter electrode. The plasma discharge exists between the two electrodes. This type of discharge is most commonly used in a vacuum chamber to avoid interferences with atmospheric gases and to facilitate the transport of sputtered material either to the surface upon which it is deposited or into the mass spectrometer.[54] Alternatively, the elements present can be detected by optical spectroscopy.[55]

Glow discharge mass spectrometry has found a place in the mass spectrometrist's repertoire largely due to its ability to determine the thickness of thin layers as part of analyzing a surface.[55, 56] This ability is essential for characterizing functionalized surfaces and determining the depth and uniformity of surface coatings. However, the requirement that the analysis occur under vacuum puts a significant limitation on the number of samples that can be analyzed in a given time period. The sputtering also causes some damage to the sample surface.

1.2.3 Laser Induced Breakdown Spectroscopy

Laser induced breakdown spectroscopy (LIBS) is a method that achieves the direct analysis of solid samples. This is accomplished by ablating a small amount of the sample using a high power laser and detecting the emission from the small plasma that is generated during the laser ablation event. This technique has been used in many applications including the analysis of organic material,[57] geological samples,[58, 59] biological samples,[60, 61] and others. The analysis is

relatively quick and direct. Little sample preparation is required, although a flat surface is preferred for performing the analysis.[62] This technique has been developed to the extent that a LIBS instrument was included on the Curiosity rover that was sent to Mars by NASA.[63]

The main limitation when using LIBS for elemental analysis is reproducibility. Shot to shot variations in laser power, interference from atmospheric species, as well as the heterogeneity of samples results at times in highly variable data.[64, 65] This liability is overcome most often through the averaging of many samples taken at various places over the sample surface.

1.2.4 Solution Cathode Glow Discharges

In a solution cathode glow discharge, rather than having a grounded metal counter electrode, an electrolyte-containing solution is used as the grounded electrode. The discharge is formed between the high voltage electrode and the solution surface. As solution is evaporated by the discharge, the analytes in the solution are exposed to the discharge and emit light characteristic of their elemental composition. Two such sources that have been reported in the literature include one from the Hieftje lab[66, 67] and one developed in the Marcus lab.[68-70]

The source developed by Hieftje et al. was designed to serve as the detector for ion chromatography systems. The effluent of the chromatography column exits the capillary into a small reservoir. A grounded graphite electrode is immersed in the solution. The researchers characterized the performance of the discharge by observing the spatial behavior of the plasma, measuring the temperature of the species in the plasma, and measuring the limits of detection. In general, the emission was found to be most intense closer to the electrodes. The temperature of the discharge, as measured based on the rotation temperature of the OH radicals in the plasma,

was in the range of 2500 to 3500 K with the highest temperature observed near the cathode. Limits of detection were measured in 10-100 ppb range.

The liquid sampling atmospheric pressure glow discharge (LS-APGD) developed by Marcus et al. operates by using a small capillary through which solution is flowing as the cathode. As with the Hieftje source, elements are identified by observing the emission from the evaporating solution, but a mass spectrometer can also be used as the detector. The performance of the source has been found to depend greatly on the pH, pNa, or pLi of the solution. However, this source has not been reported as being as sensitive as other elemental analysis sources. Solution is flowed at ~3 mL min^{-1} and limits of detection are in the ~10 ppm range. Another use that has very recently been discovered for this source is the measurement of isotope ratios. By coupling the source to an Orbitrap mass spectrometer, the isotope ratios of uranium samples have been measured.

1.3 My Research Focus

The research I present in this dissertation focuses on gaining a more thorough understanding of the fundamental processes that occur in ambient plasma discharges used for ionizing samples. I have also done experiments furthering the work of H_2 doping of plasma gases to observe their effects on the performance of plasma discharges as ionization sources. I have also designed a computer simulation that has provided insight into the chemistry of a helium-based discharge.

1.4 References

1. Takats, Z.; Wiseman, J. M.; Gologan, B.; Cooks, R. G., *Science* **2004,** *306*, 471-473.
2. Cody, R. B.; Laramée, J. A.; Durst, H. D., *Anal. Chem.* **2005,** *77*, 2297-2302.

3. Monge, M. E.; Harris, G. A.; Dwivedi, P.; Fernández, F. M., *Chem. Rev.* **2013,** *113*, 2269-2308.
4. Pulliam, C.; Bain, R.; Wiley, J.; Ouyang, Z.; Cooks, R. G., *J. Am. Soc. Mass. Spectrom.* **2015,** *26*, 224-230.
5. Soparawalla, S.; Tadjimukhamedov, F. K.; Wiley, J. S.; Ouyang, Z.; Cooks, R. G., *Analyst* **2011,** *136*, 4392-4396.
6. Tillner, J.; McKenzie, J. S.; Jones, E. A.; Speller, A. V. M.; Walsh, J. L.; Veselkov, K. A.; Bunch, J.; Takats, Z.; Gilmore, I. S., *Anal. Chem.* **2016,** *88*, 4808-4816.
7. Li, B.; Bjarnholt, N.; Hansen, S. H.; Janfelt, C., *J. Mass Spectrom.* **2011,** *46*, 1241-1246.
8. Wu, C.; Ifa, D. R.; Manicke, N. E.; Cooks, R. G., *Analyst* **2010,** *135*, 28-32.
9. Yao, Z.-P., *Mass Spectrom. Rev.* **2012,** *31*, 437-447.
10. Takáts, Z.; Wiseman, J. M.; Cooks, R. G., *J. Mass Spectrom.* **2005,** *40*, 1261-1275.
11. Wood, M. C.; Busby, D. K.; Farnsworth, P. B., *Anal. Chem.* **2009,** *81*, 6407-6415.
12. Roach, P. J.; Laskin, J.; Laskin, A., *Analyst* **2010,** *135*, 2233-2236.
13. Albert, A.; Engelhard, C., *Anal. Chem.* **2012,** *84*, 10657-10664.
14. Cody, R. B., *Anal. Chem.* **2008,** *81*, 1101-1107.
15. Dane, A. J.; Cody, R. B., *Analyst* **2010,** *135*, 696-699.
16. Fernández, F. M.; Cody, R. B.; Green, M. D.; Hampton, C. Y.; McGready, R.; Sengaloundeth, S.; White, N. J.; Newton, P. N., *ChemMedChem* **2006,** *1*, 702-705.
17. Lesiak, A. D.; Cody, R. B.; Dane, A. J.; Musah, R. A., *Anal. Chem.* **2015,** *87*, 8748-8757.
18. Keelor, J.; Dwivedi, P.; Fernández, F., *J. Am. Soc. Mass. Spectrom.* **2014,** *25*, 1538-1548.
19. Andrade, F. J.; Shelley, J. T.; Wetzel, W. C.; Webb, M. R.; Gamez, G.; Ray, S. J.; Hieftje, G. M., *Anal. Chem.* **2008,** *80*, 2654-2663.
20. Pfeuffer, K. P.; Schaper, J. N.; Shelley, J. T.; Ray, S. J.; Chan, G. C. Y.; Bings, N. H.; Hieftje, G. M., *Anal. Chem.* **2013,** *85*, 7512-7518.
21. Schaper, J. N.; Pfeuffer, K. P.; Shelley, J. T.; Bings, N. H.; Hieftje, G. M., *Anal. Chem.* **2012,** *84*, 9246-9252.
22. Storey, A. P.; Zeiri, O. M.; Ray, S. J.; Hieftje, G. M., *J. Anal. At. Spectrom.* **2015,** *30*, 2017-2023.
23. Storey, A. P.; Zeiri, O. M.; Ray, S. J.; Hieftje, G. M., *J. Am. Soc. Mass. Spectrom.* **2016,** *28*, 263-269.
24. Pfeuffer, K. P.; Caldwell, J.; Shelley, J. T.; Ray, S. J.; Hieftje, G. M., *Analyst* **2014,** *139*, 4505-4511.
25. Harper, J. D.; Charipar, N. A.; Mulligan, C. C.; Zhang, X.; Cooks, R. G.; Ouyang, Z., *Anal. Chem.* **2008,** *80*, 9097-9104.
26. Na, N.; Zhao, M.; Zhang, S.; Yang, C.; Zhang, X., *J. Am. Soc. Mass. Spectrom.* **2007,** *18*, 1859-1862.
27. Bowfield, A.; Barrett, D. A.; Alexander, M. R.; Ortori, C. A.; Rutten, F. M.; Salter, T. L.; Gilmore, I. S.; Bradley, J. W., *Rev. Sci. Instrum.* **2012,** *83*, 063503-1-063503-7.
28. Herrera, L. C.; Grossert, J. S.; Ramaley, L., *J. Am. Soc. Mass. Spectrom.* **2008,** *19*, 1926-1941.
29. Shelley, J.; Chan, G. Y.; Hieftje, G., *J. Am. Soc. Mass. Spectrom.* **2012,** *23*, 407-417.
30. Heywood, M. S.; Taylor, N.; Farnsworth, P. B., *Anal. Chem.* **2011,** *83*, 6493-6499.
31. Chan, G. C. Y.; Shelley, J. T.; Jackson, A. U.; Wiley, J. S.; Engelhard, C.; Cooks, R. G.; Hieftje, G. M., *J. Anal. At. Spectrom.* **2011,** *26*, 1434-1444.

32. Chan, G. C. Y.; Shelley, J. T.; Wiley, J. S.; Engelhard, C.; Jackson, A. U.; Cooks, R. G.; Hieftje, G. M., *Anal. Chem.* **2011,** *83*, 3675-3686.
33. Reininger, C.; Woodfield, K.; Keelor, J. D.; Kaylor, A.; Fernández, F. M.; Farnsworth, P. B., *Spectrochim. Acta B* **2014,** *100*, 98-104.
34. Müller, S.; Krähling, T.; Veza, D.; Horvatic, V.; Vadla, C.; Franzke, J., *Spectrochim. Acta B* **2013,** *85*, 104-111.
35. Meyer, C.; Müller, S.; Gilbert-Lopez, B.; Franzke, J., *Anal. Bioanal. Chem.* **2013,** *405*, 4729-4735.
36. Klute, F. D.; Michels, A.; Schutz, A.; Vadla, C.; Horvatic, V.; Franzke, J., *Anal. Chem.* **2016,** *88*, 4701-5.
37. Karakas, E.; Koklu, M.; Laroussi, M., *J. Phys. D: Appl. Phys.* **2010,** *43*, 155202.
38. Naidis, G. V., *J. Phys. D: Appl. Phys.* **2010,** *43*, 402001.
39. Sakiyama, Y.; Graves, D. B.; Jarrige, J.; Laroussi, M., *Appl. Phys. Lett.* **2010,** *96*, 041501.
40. Klute, F. D.; Schutz, A.; Michels, A.; Vadla, C.; Veza, D.; Horvatic, V.; Franzke, J., *Analyst* **2016,** *141*, 5842-5848.
41. Newsome, G. A.; Ackerman, L. K.; Johnson, K. J., *Anal. Chem.* **2014,** *86*, 11977-11980.
42. Newsome, G. A.; Ackerman, L. K.; Johnson, K. J., *J. Am. Soc. Mass. Spectrom.* **2015,** *27*, 135-143.
43. Brüggemann, M.; Karu, E.; Hoffmann, T., *J. Mass Spectrom.* **2016,** *51*, 141-149.
44. Shelley, J. T.; Stindt, A.; Riedel, J.; Engelhard, C., *J. Anal. At. Spectrom.* **2014,** *29*, 359-366.
45. McKay, K.; Walsh, J. L.; Bradley, J. W., *Plasma Sources Sci. Technol.* **2013,** *22*, 035005.
46. Shelley, J. T.; Hieftje, G. M., *J. Anal. At. Spectrom.* **2010,** *25*, 345-350.
47. Wright, J. P.; Heywood, M. S.; Thurston, G. K.; Farnsworth, P. B., *J. Am. Soc. Mass. Spectrom.* **2013,** *24*, 335-340.
48. Martens, T.; Mihailova, D.; van Dijk, J.; Bogaerts, A., *Anal. Chem.* **2009,** *81*, 9096-9108.
49. Bogaerts, A.; Gijbels, R., *Spectrochim. Acta B* **2002,** *57*, 1071-1099.
50. Houk, R. S.; Fassel, V. A.; Flesch, G. D.; Svec, H. J.; Gray, A. L.; Taylor, C. E., *Anal. Chem.* **1980,** *52*, 2283-2289.
51. Hubbard, J. A.; Zigmond, J. A., *Spectrochim. Acta B* **2016,** *119*, 50-64.
52. Günther, D.; Jackson, S. E.; Longerich, H. P., *Spectrochim. Acta B* **1999,** *54*, 381-409.
53. Chung, J.-L.; Chen, J.-C.; Tseng, C.-J., *Appl. Surf. Sci.* **2008,** *255*, 2494-2499.
54. Bings, N. H.; Bogaerts, A.; Broekaert, J. A. C., *Anal. Chem.* **2004,** *76*, 3313-3336.
55. Bengtson, A.; Lundholm, M., *J. Anal. At. Spectrom.* **1988,** *3*, 879-882.
56. Laidani, N.; Bartali, R.; Tosi, P.; Anderle, M., *J. Phys. D: Appl. Phys.* **2004,** *37*, 2593.
57. Baudelet, M.; Boueri, M.; Yu, J.; Mao, S. S.; Piscitelli, V.; Mao, X.; Russo, R. E., *Spectrochim. Acta B* **2007,** *62*, 1329-1334.
58. Bicchieri, M.; Nardone, M.; Russo, P. A.; Sodo, A.; Corsi, M.; Cristoforetti, G.; Palleschi, V.; Salvetti, A.; Tognoni, E., *Spectrochim. Acta B* **2001,** *56*, 915-922.
59. Sirven, J.-B.; Salle, B.; Mauchien, P.; Lacour, J.-L.; Maurice, S.; Manhes, G., *J. Anal. At. Spectrom.* **2007,** *22*, 1471-1480.
60. Kaiser, J.; Novotný, K.; Martin, M. Z.; Hrdlička, A.; Malina, R.; Hartl, M.; Adam, V.; Kizek, R., *Surf. Sci. Rep.* **2012,** *67*, 233-243.
61. Kumar, A.; Yueh, F.-Y.; Singh, J. P.; Burgess, S., *Appl. Opt.* **2004,** *43*, 5399-5403.
62. Mao, S. S.; Zeng, X.; Mao, X.; Russo, R. E., *J. Anal. At. Spectrom.* **2004,** *19*, 495-498.

63. Wiens, R. C.; Maurice, S.; Lasue, J.; Forni, O.; Anderson, R. B.; Clegg, S.; Bender, S.; Blaney, D.; Barraclough, B. L.; Cousin, A.; Deflores, L.; Delapp, D.; Dyar, M. D.; Fabre, C.; Gasnault, O.; Lanza, N.; Mazoyer, J.; Melikechi, N.; Meslin, P. Y.; Newsom, H.; Ollila, A.; Perez, R.; Tokar, R. L.; Vaniman, D., *Spectrochim. Acta B* **2013,** *82*, 1-27.
64. Dong, F.-Z.; Chen, X.-L.; Wang, Q.; Sun, L.-X.; Yu, H.-B.; Liang, Y.-X.; Wang, J.-G.; Ni, Z.-B.; Du, Z.-H.; Ma, Y.-W.; Lu, J.-D., *Front. Phys.* **2012,** *7*, 679-689.
65. Kasem, M. A.; Gonzalez, J. J.; Russo, R. E.; Harith, M. A., *Spectrochim. Acta B* **2014,** *101*, 26-31.
66. Schwartz, A. J.; Wang, Z.; Ray, S. J.; Hieftje, G. M., *Anal. Chem.* **2013,** *85*, 129-137.
67. Webb, M. R.; Andrade, F. J.; Gamez, G.; McCrindle, R.; Hieftje, G. M., *J. Anal. At. Spectrom.* **2005,** *20*, 1218-1225.
68. Hoegg, E. D.; Barinaga, C. J.; Hager, G. J.; Hart, G. L.; Koppenaal, D. W.; Marcus, R. K., *J. Am. Soc. Mass. Spectrom.* **2016,** *27*, 1393-403.
69. Hoegg, E. D.; Barinaga, C. J.; Hager, G. J.; Hart, G. L.; Koppenaal, D. W.; Marcus, R. K., *J. Anal. At. Spectrom.* **2016,** *31*, 2355-2362.
70. Marcus, R. K.; Davis, W. C., *Anal. Chem.* **2001,** *73*, 2903-2910.

2 THE EFFECTS OF ADDED HYDROGEN ON AMBIENT HELIUM AND ARGON DISCHARGES USED FOR MASS SPECTROMETRY

2.1 Using Hydrogen Doped Plasma Gases in ADI-MS

When doing molecular mass spectrometry using ADI-MS in positive ion mode, the mass spectra obtained consist primarily of intact ions, either in the form of M^+ or $[M+H]^+$. $[M+H]^+$ ions are the most common. The amount of fragmentation observed for analyte molecules is minimal. Increasing the intensity of the signal obtained using any ionization source is an important goal. It increases the sensitivity of the source while decreasing the limit of detection. In order to accomplish this with a source that generates mostly protonated analyte ions, it is logical to assume that the addition of more hydrogen to the plasma gas would help when trying to increase the signal intensity. The simplest hydrogen-containing species that could be added to the gas would be molecular hydrogen, H_2. The use of hydrogen-doped helium has been experimented with previously in two publications from the Farnsworth group.[1, 2] The results indicated that there was a significant signal enhancement effect by adding 0.9 % H_2 to helium for a set of four chemicals in positive ion mode: caffeine, anthracene, diphenylamine, and coumarin 460. In negative ion mode, 1,3-dinitrobenzene was tested, but no signal enhancement was observed. However, the effects observed were not fully characterized in a quantitative manner.

Previous attempts to use argon as the plasma gas of the LTP have shown it to be inferior to helium in terms of signal intensity. The signals obtained using an argon LTP were 10 to 100

times less intense that those obtained with a helium LTP.[3] Although this lack of signal may appear to disqualify argon as a serious plasma gas option, there are also some considerable challenges faced when using helium. First, helium is a non-renewable resource. Once helium is released into the atmosphere, it is difficult to recapture due to its extremely low boiling point. In addition, due to its low atomic mass, it has the ability to escape from Earth's atmosphere. Second, due to its low mass and incompressibility, helium is more difficult than other gases to remove from a vacuum chamber using turbo molecular pumps such as are used commonly in many mass spectrometers. So, using helium can lead to higher operating pressures in the mass spectrometer, which can negatively impact the resolution and accuracy of the measurements. Finally, helium can be fairly expensive to purchase given that its supply is not always consistent. In these regards, argon is a much better option due to it being a renewable resource, easy to remove from a chamber via turbo molecular pump, and generally less expensive than helium. We theorized that the addition of hydrogen to argon may overcome the low signal intensity by increasing its ionization efficiency.

The chemistry between argon ions and H_2 has been well documented in research performed in the inductively coupled plasma mass spectrometry (ICP-MS) community. Ar^+ is a significant interfering species when performing ICP-MS analyses. It was found in work done at the Pacific Northwest National Laboratory that the addition of H_2 to a collision cell in an ICP-MS instrument greatly reduced the number of Ar^+ ions.[4, 5] The reaction between Ar^+ and H_2 has a fairly large collisional cross section and results in the formation of H_2^+, H_3^+, and ArH^+ ions. These results further support the idea that doping argon with H_2 would potentially yield positive results in ADI-MS.

Additionally, we wanted to test the effect of hydrogen addition to discharge configurations other than the DBD. The following studies sought to further explore the idea of hydrogen addition in argon with another discharge type, and in a more quantifiable way. This work has been published in the Journal of the American Society for Mass Spectrometry.[6]

2.2 Experimental Setup

2.2.1 Chemicals Tested

The same group of chemicals tested by Wright et al.[1] was used. The five chemicals tested included caffeine (Sigma Aldrich, Steinheim, Germany), anthracene (Spectrum Chemical Mfg Corp, Gardena, CA), diphenylamine (Brigham Young University chemical surplus, source unknown), coumarin 460 (Exciton, Dayton, OH), and 1,3,-dinitrobenzene (The Matheson Company, East Ruthersford, NJ). For analyzing caffeine, anthracene, diphenylamine, and coumarin 460, solutions were made with concentrations of 100 mg L^{-1} in HPLC grade methanol. For 1,3,-dinitrobenzene, a solution with a concentration of 1 g L^{-1} was made in HPLC grade methanol. For the experiments described below, in which the limit of detection was determined for caffeine, HPLC grade acetonitrile was used as the solvent.

2.2.2 Discharge Sources

Two discharge sources were used in these experiments. The configurations are described here and shown schematically in figure 2-1. They included a DBD and an AC glow discharge. The DBD was generated in a fused quartz tube (id 1 mm, od 3 mm) with a copper ring electrode attached to the outside of the tube 10 mm away from the end of the tube and a hypodermic needle electrode inside the glass tube. High voltage alternating current was applied to the copper

ring electrode while the needle electrode was grounded. The power applied to the discharge was 31 W when using helium and 10 W when using argon at a frequency of 325 kHz. The tube and the electrodes were all held together using a 1/8 inch steel Swagelok T.

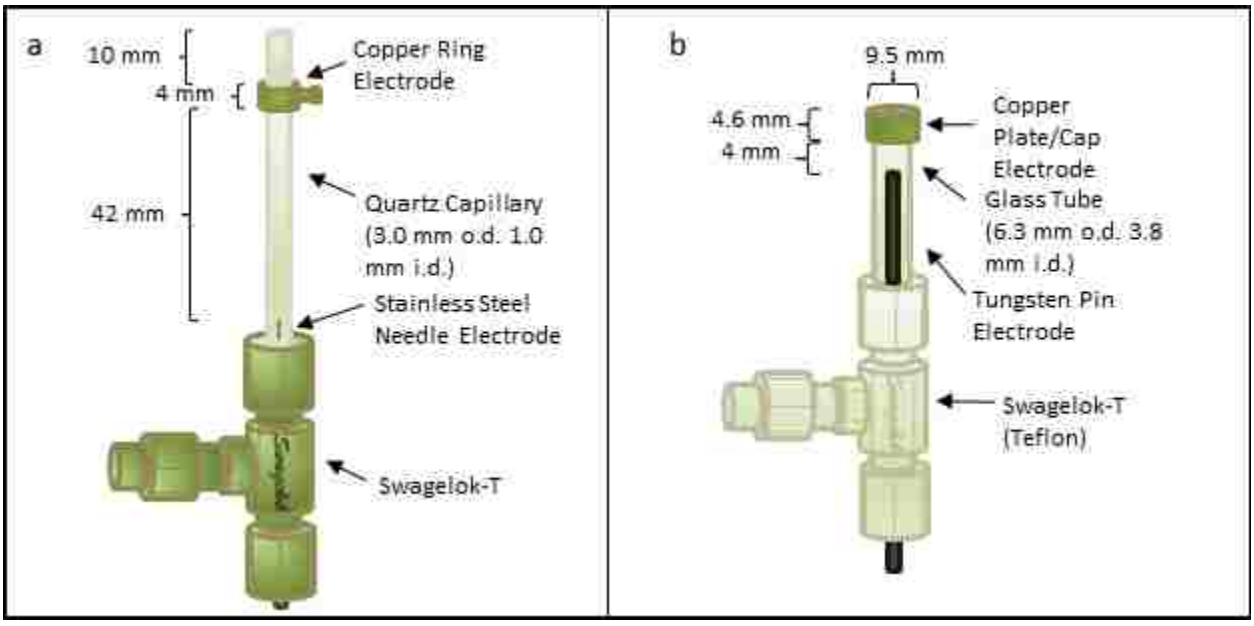

Figure 2-1 : Schematic representations of the dielectric barrier discharge (a) and AC glow discharge (b) used in these studies.

The AC discharge used consisted of a glass tube (id 3.8 mm, od 6.4 mm) with a copper plate electrode attached to the end and a 1- mm-diameter tungsten pin positioned coaxially inside the tube. The copper plate had a 2-mm hole in the center coaxial with the tube and the tungsten pin. High voltage was applied to the tungsten pin while the copper plate was grounded. The power applied to the discharge was 10 W for all plasma gases at a frequency of 325 kHz. All the discharge components were held together using a 1/4 inch nylon Swagelok T.

Power was supplied by a ENI HPG-2 radio frequency power supply (MKS Instruments, Andover, MA). The plasma gases included ultra-high purity argon (99.999 % Ar) (Airgas, Radnor, PA), 2.90 % H_2 in argon (Airgas), ultra-high purity helium (99.999 % He) (Airgas), and 1.0 % H_2 in helium (Airgas). Gas flow rates were controlled by a pair of mass flow controllers

(MKS1170A, MKS, Andover, MA) with their corresponding power supplies/readouts (MKS246C, MKS, Andover, MA). Plasma gas was flowed at a rate of 2 L min^{-1}. By using the two mass flow controllers in tandem, a range of H_2 concentrations could be obtained by mixing the gas streams in the correct ratios.

2.2.3 Mass Spectrometer Setup

All experiments were performed on a time-of-flight mass spectrometer (MicrOTOF II, Bruker Daltonics, Billerica, MA). The mass spectrometer was modified in two ways. First, the electrospray ionization source and the spray shield were removed to expose the atmospheric pressure inlet. Second, an additional mechanical vacuum pump was attached to the first vacuum stage to reduce the strain on the vacuum system when using helium or H_2/He as the plasma gas. This extra pump was always operational regardless of the plasma gas used in order to maintain consistent vacuum conditions.

Analyte was introduced into the mass spectrometer is one of two ways. First, to allow for both desorption and ionization to occur, glass microscope slides were dipped in the analyte containing solutions. They were withdrawn at a rate of 0.5 cm s^{-1} in order to deposit a uniform coating on the surface of the desired analyte.[7] This constant withdrawal rate was achieved using a stepper motor controlled by LabVIEW (National Instruments, Austin, TX). The coated slides were then placed in front of the mass spectrometer inlet with the discharge source above them. The discharge was positioned using an x, y, z, θ stage. When using argon or H_2/Ar, the DBD was positioned 1.5 mm above the slide and 14 mm away from the inlet, with the discharge forming an angle of 35° with the glass slide. When using helium or H_2/He, the DBD was positioned perpendicular to the axis of the mass spectrometer inlet. The tip of the discharge was

12 mm above the slide, 10 mm from the inlet, and 7 mm off center. The perpendicular positioning was necessary to avoid the introduction of excess helium into the mass spectrometer. Excess helium caused a shutdown of the mass spectrometer due to elevated pressure in the high vacuum chamber when introducing helium, even with the use of the extra vacuum pump. The discharge formed an angle of 45° with the slide. For each experiment with a coated slide, data were acquired for 120 seconds to monitor the removal of the analyte from the slide.

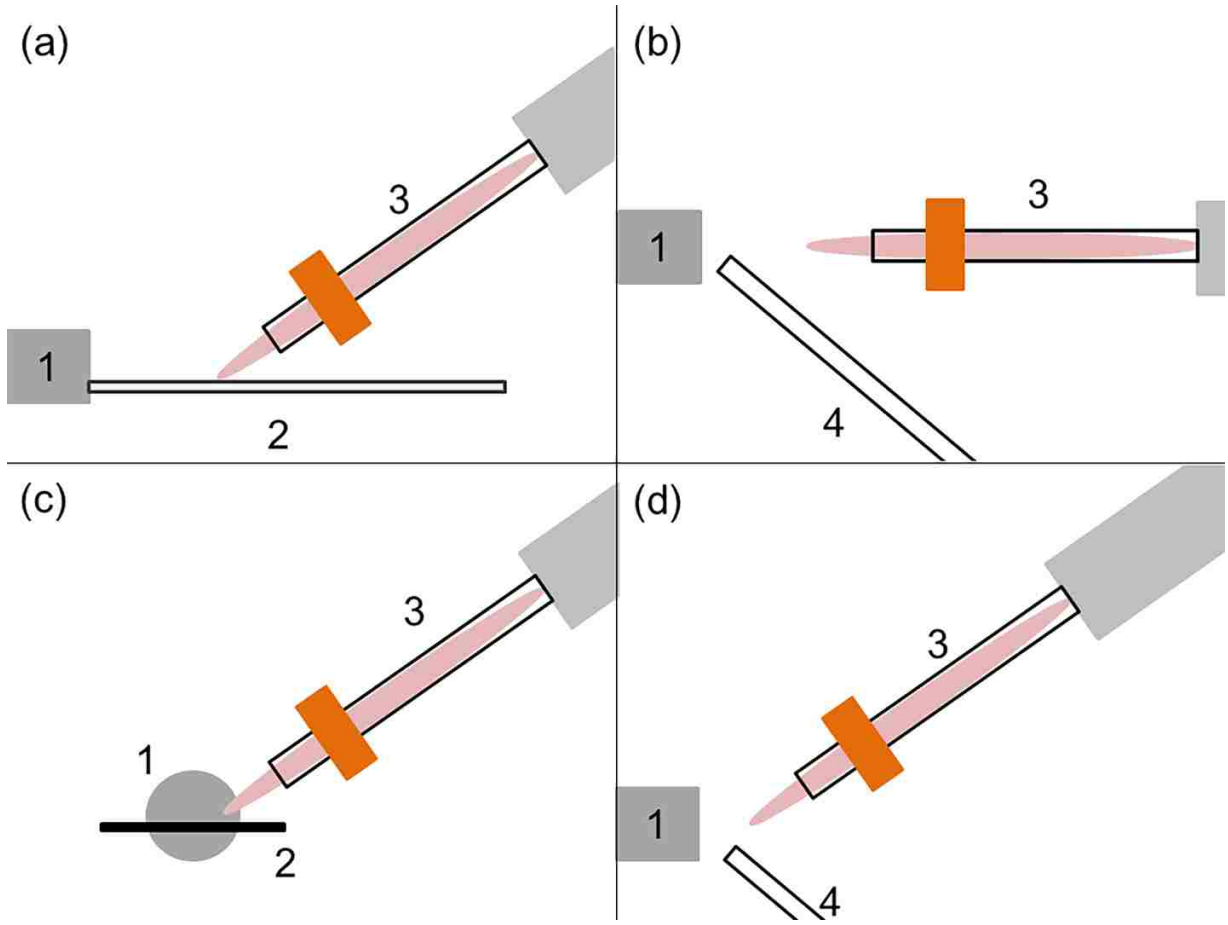

Figure 2-2 : Experimental setup for each experiment described. (a) Side on view of the coated slide setup when using Ar or H2/Ar. (b) Side on view of the gaseous analyte setup when using Ar and H2/Ar. (c) View looking straight on the MS inlet of the coated slide setup when using He or H2/He. Note that the discharge is perpendicular to the orientation used with Ar. (d) Side on view of the gaseous analyte setup using He or H2/He. The numbers represent the following: 1 – MS inlet, 2 – Glass microscope slide coated in analyte, 3 – Discharge (either DBD or AC glow discharge), and 4 – Tube used to introduce gaseous caffeine. (Figure used by permission from ref. 6)

The second sample introduction method involved introducing the sample as a gas. To generate gas phase analyte, N_2 gas was flowed over a small amount of solid analyte in a round bottom flask. The flow of N_2 was then directed to the inlet of the mass spectrometer using a 1/8 inch polypropylene tube. The discharge was positioned in front of the mass spectrometer pointing straight at the inlet for argon and H_2/Ar, but had to be positioned at an angle when using helium or H_2/He, to once again avoid over pressurizing the vacuum chamber. In this configuration, it was easier to experiment with several parameters, including adjusting the amount of H_2 in the plasma gas rapidly. See figure 2-2 for a schematic representation of the various sample introduction methods.

2.3 Signal Enhancement with Added Hydrogen

2.3.1 Optimal Amount of Hydrogen in Argon

By performing experiments where the concentration of hydrogen in argon was varied, we were able to best ascertain the concentration at which to perform the other experiments. The data from these experiments are shown in shown in figure 2-3. For caffeine, the signal increased until approximately 1.5 % H_2, after which a plateau was reached. For anthracene, the signal increased gradually throughout the range of H_2 concentrations tested. For coumarin 460, the signal increased until approximately 2.2 % H_2 in argon, then fell off. The lack of a plateau in the anthracene data emphasizes the differences in mechanism for the signal enhancement of $[M+H]^+$ ion forming species and those that for an M^+ ion. Based on these data, the remaining experiments were carried out at 2.9 % H_2 in argon to avoid the use of multiple mass flow controllers. Diphenylamine was not included in these experiments because it thermally

decomposed prior to reaching the mass spectrometer inlet, making it impossible to get reproducible and accurate results.

2.3.2 Coated Slides

The signal enhancement for the analytes used when using H_2/He has already been documented,[1] so I performed this type of experiment only with H_2/Ar and pure argon. When using these two plasma gases with the DBD, there was a significant increase in signal intensity when using 2.90 % H_2 in argon. Figure 2-4 shows a comparison of the signal of argon vs H_2/Ar for the four analytes tested in positive ion mode. The signal intensity was measured by summing the counts for the desired peak over the time the discharge was on. Using this method, the signal enhancements for caffeine, anthracene, diphenylamine, and coumarin 460 were 6, 2, 3, and 40 times, respectively, when compared to the signal when using pure argon. The peaks monitored for each analyte were the $[M+H]^+$ peaks for caffeine, diphenylamine, and coumarin 460 and the M^+ peak for anthracene. The m/z values for these peaks were 195.09, 170.23, 232.30, and 178.23 respectively for caffeine, diphenylamine, coumarin 460, and anthracene.

In negative ion mode, only 1,3-dinitrobenzene gave signal of any kind. To obtain signal with intensity comparable to the positive ion mode analyes, slides had to be coated with a solution that was 10 times more concentrated than the solutions of analytes for positive ion mode. The peaks observed included the M^- peak at 168.01 m/z and the $[M-H+O]^-$ peak at 183.00 m/z. When using 2.90 % H_2 in argon as the plasma gas, the integrated signal of the $[M-H+O]^-$ peak increased by a factor of 6 compared to the signal obtained using pure argon.

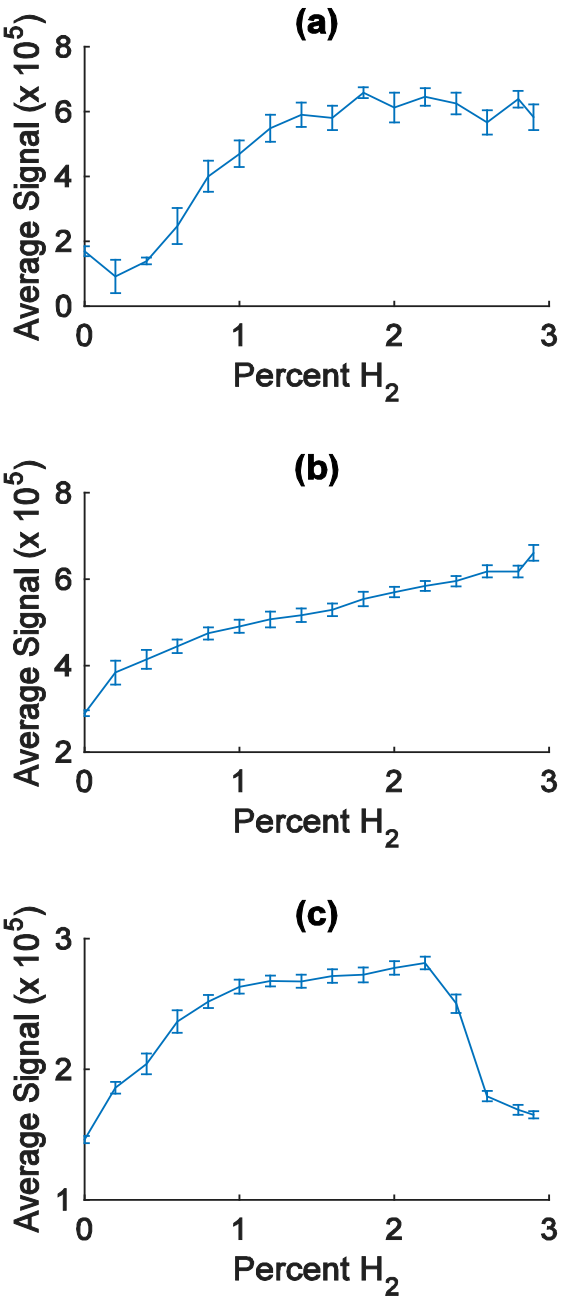

Figure 2-3 : Mass spectrometric signal intensities for different percentages of hydrogen in argon for (a) caffeine, (b) anthracene, and (c) courmarin 460. For (a) and (c), the traces are of the $[M+H]^+$ peak. For (b) the trace is of the M^+ peak. The error bars are the standard deviations of sixty one-second integrations, and are indicative of the short-term stability of the signal. Each curve was measured twice to check the reproducibility of the shape. (Figure used by permission from ref. 6)

When using the AC discharge with coated slides, signal was observed when using pure argon with a caffeine coated slide, but when H_2/Ar was used, no signal enhancement was observed.

2.3.2.1 Limit of Detection

The limit of detection for each plasma gas with the DBD was measured using the same set up as was used for the coated slides. However, in these experiments, a drop of caffeine solution was placed on the slide rather than coating the whole slide. The caffeine was dissolved in acetonitrile rather than methanol for these experiments because the acetonitrile formed a better bead of liquid on the surface of a glass slide that allowed for better reproducibility of drop placement. A series of caffeine solutions was made to cover at least three decades above the minimal detectable concentration. By placing a droplet of a known volume on the slide and allowing it to dry, a known mass of caffeine was thus placed on the slide for analysis. For the blank measurements, a drop of pure acetonitrile was allowed to dry on the slide and then analyzed with the DBD. The limit of detection was calculated as three times the standard deviation of a blank sample divided by the slope of the calibration curve. These experiments were based on a method developed by Cooks et al.[8] The results for the DBD showed absolute limits of detection for caffeine of 18 ng and 230 pg for argon and H_2/Ar and 290 pg and 150 pg for helium and H_2/He.

2.3.2.2 Sample Area vs Sensitivity

To determine if there was any correlation between the sensitivity of the DBD and the area it sampled on a slide, the sampled area was measured by coating a slide using a 1000 ppm solution of coumarin 460 in methanol. Coumarin 460 is a laser dye that absorbs light in the ultraviolet range between 365 nm and 375 nm and subsequently fluoresces in the visible range at

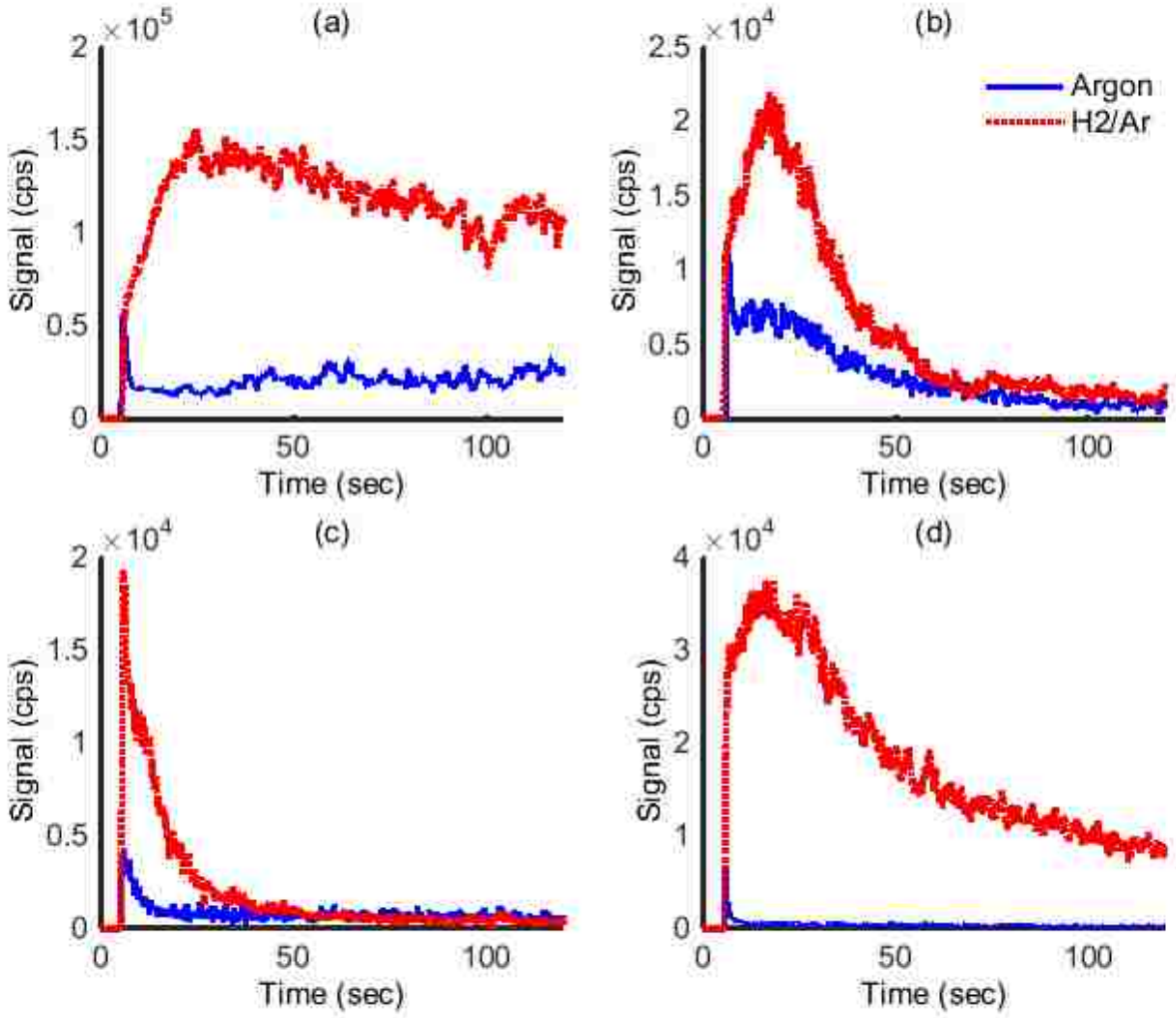

Figure 2-4 : Chronograms for (a) caffeine, (b) anthracene, (c) diphenylamine, and (d) coumarin 460. For (a), (c), and (d), the traces are of the [M + H]+ peak. For (b) the trace is of the M+ peak. Zero time is the beginning of data acquisition. The plasma was ignited at 6 s. (Figure used by permission from ref. 6)

460 nm. To measure the size of the spot where sample was removed, the coated slide was exposed to the plasma discharge in the same configuration as described above for coated slides with the exception that the discharge was only left on for 30 seconds. After being exposed, the slide was bathed in light from a UV lamp. The non-fluorescent areas then represented the area where the plasma had removed sample. These areas were measured using a ruler to approximate

the area sampled by the discharge. This was done using all four gas compositions with the DBD: pure argon, H_2/Ar, pure helium, and H_2/He.

It was found that the area sampled by the argon, H_2/Ar, helium, and H_2/He DBDs were ~1.1 cm^2, ~0.77 cm^2, ~1.85 cm^2, and ~1.14 cm^2, respectively. It is readily apparent that each hydrogen doped gas samples a smaller area than the pure gas. There is therefore an inverse correlation between sensitivity and the sampled area. This suggests that the hydrogen doped plasmas are able to generate more detectable ions from a smaller amount of sample.

2.3.2.3 Changes to the Desorption Mechanism

As can be seen in figure 2-4 and in reference 1, the addition of hydrogen changed the temporal profile of the graphs showing the removal of analyte from a slide. These differences suggest that there is a change to the desorption mechanism when hydrogen is added to the plasma gas. Generally, it is assumed that the main cause of desorption when using these plasma discharges is heating of the surface, which causes evaporation of sample. However, by measuring the temperature of slides exposed to the DBD using the different gas mixtures, we found that thermal desorption is not the only mechanism involved.

To measure the temperature of slides, a thermal imager (Ti27, Fluke, Everett, WA) was used. A glass slide was placed under the active discharge until it reached a constant temperature, at which point a picture was taken. Slides exposed to the argon, H_2/Ar, helium, and H_2/He DBDs were found to reach temperatures of 35.2, 43.5, 101.1, and 82.1 °C respectively. This shows that there is no correlation between the relative temperatures of the discharges and the observed signal intensity or temporal profile. Although these data clearly show that some non-thermal desorption mechanism occurs, it does not offer any evidence as to what might be

happening. Possible options for removal of analyte non-thermally include chemical sputtering or field desorption. In chemical sputtering, the collision of high energy particles with a surface causes the ejection of particles from the surface. In the instance of field desorption, the electric field of the discharge would presumably cause ionization of molecules while still on the surface, causing them to be removed from the surface.

2.3.3 Gas Phase Analyte

When performing experiments with the gas phase analyte setup, the plasma gas could be switched between pure argon and H_2/Ar within the same data acquisition using the pair of mass flow controllers. The results of these experiments for both caffeine and anthracene when using the DBD are seen in figure 2-5. The signal of caffeine was increased by a factor of 5 and the signal of anthracene was increased by a factor of 4 over that of pure argon when using H_2/Ar. These experiments remove the desorption step from the sampling process and show that the addition of hydrogen directly affects the ionization process in some way.

When using the AC discharge, a similar signal increase was observed when using H_2/Ar. However, the degree of signal enhancement depended greatly on the distance between the discharge and the mass spectrometer inlet. At just 1 cm away from the inlet, no signal increase was observed for caffeine. In fact, when H_2/Ar was used the signal dropped to a level lower than that when using pure argon. However, when the discharge was placed 2 cm away from the inlet, an increase in signal was observed. When the discharge was moved to be 3 cm away from the

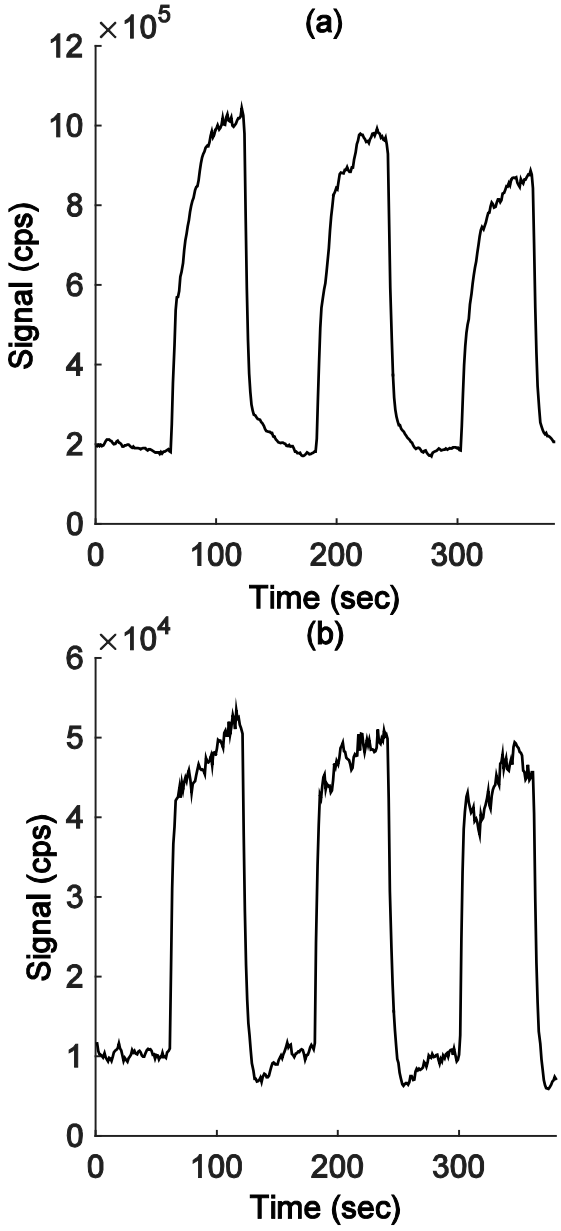

Figure 2-5 : The results from the experiments in which gaseous analyte was introduced directly at the inlet for caffeine (a) and anthracene (b). The support gas was changed every 60 seconds from argon to argon/hydrogen, starting with argon at time zero. (Figure used by permission from ref. 6)

inlet, once again no signal increase was observed. There are many factors which could be influencing this change in observed signal. These include interactions with the atmosphere, changes in the amount of the gas stream leaving the discharge that reaches the inlet, and changes to the gas-phase kinetics. When performing this same type of experiment with helium and

H_2/He, no conditions were found under which signal increase was observed using the AC discharge. This suggested that the differences in discharge configuration and geometry between a glow discharge and a DBD may be influencing the signal enhancement phenomenon.

One major difference between the two types of discharges is how the plasma is grounded. The AC discharge is given an easy ground in the form of the grounded copper plate electrode downstream from the tungsten pin. However, the DBD has no such obvious ground. The grounded electrode is separated from the high voltage electrode by a glass barrier. Although there is certainly some grounding that occurs through that electrode, the presence of a plume of plasma that extends beyond the end of the glass tube shows that the DBD grounds in a different way. The discharge is in part grounded through the air or through any metal objects that are near the plasma plume. If a metal object, such as the mass spectrometer inlet, is brought into close proximity with the DBD plume, it will arc to it and become much brighter and more intense. The plume does not extend beyond the metal object. To observe what effects this type of forced grounding had on the ionization, the gas phase analyte experiments were repeated with a grounded wire placed in the path of the DBD such that the plume arced to it.

The results obtained from these experiments matched those obtained with the AC discharge. When comparing argon to H_2/Ar, a signal increase was observed. However, when comparing helium to H_2/He, no signal enhancement was observed. To further explore this phenomenon, a voltage was applied to the wire instead of grounding it. This was done by connecting the wire to a DC power supply (Model IP-17, Heathkit, Santa Cruz, CA). In order to isolate the applied voltage from the ground, a resistor (3.3 kΩ) and a capacitor (20 μF) were placed in the circuit in series with the power supply. In all cases where a voltage was applied to the wire, no signal increase was observed for any gas composition.

2.4 Background Ion Mass Spectra

Changes to the ionization or desorption mechanisms must be related to changes in the reagent ions formed by the discharge when hydrogen is added to the plasma gas. To determine what changes occurred, mass spectra were taken of the background ions for both the DBD and the AC discharge using the same setup as was used for the gas phase analyte studies, with the exception that no analyte was introduced. The mass spectrometer was tuned to observe lower mass ions. The lowest mass observable by the micrOTOF II is ~35 m/z.

For the DBD, the most abundant ions in the background mass spectra were protonated water cluster ions ($H(H_2O)_n^+$). The most abundant cluster in all plasma gas compositions was the n=3 ion, but the n=2, 4, 5, and 6 ions were also observed. Other abundant ions that I was able to identify were the $[M+H]^+$ ions of acetone, ethyl acetate, methyl acetate, $CH_3CN(H_2O)$, and $CH_3CN(CH_3OH)$. These are all solvents that were present in the lab at the time of recording these background spectra, so likely came from the lab air. There were many other ions observed that I was unable to identify due to a lack of MS/MS capabilities. It is significant to note that the abundance of all protonated water cluster ions decreased when hydrogen was added to the plasma gas. The predominant ion remained the n=3 protonated water cluster, but the intensity of each peak decreased significantly.

For the AC discharge, in addition to the ions observed in the DBD background, we observed ions generated from the copper electrode. These included Cu^+, $Cu(NH_3)_2^+$, $Cu(NH_3)(H_2O)^+$, and $Cu(H_2O)_2^+$. These ions were present in the background spectra for all gas compositions, but were most abundant in the background spectra for the H_2/Ar AC discharge. The intensity of these metal containing peaks also depended greatly on the distance between the discharge and the mass spectrometer inlet. They were more abundant as the discharge was

moved further away. These ions were assumed to have been removed through a process such as chemical sputtering. This leads us to believe that the addition of hydrogen increases the sputtering efficiency or the ionization efficiency of the sputtered material. This phenomenon will be described in greater detail in the following chapter.

2.5 Potential Changes to Ionization Mechanism

In addition to changes in the desorption mechanism already mentioned, these experiments show clearly that there are also changes that occur to the ionization with the addition of hydrogen. For M^+ ion formation, it is not clear what changes to the plasma would increase the ionization efficiency. In a helium DBD, the main process by which M^+ ions are formed is through charge transfer with N_2^+ and O_2^+.[9, 10] However, it has been seen that the addition of hydrogen to helium quenches both N_2^+ and O_2^+ ion populations.[3] It is therefore still unclear what causes the increase in signal for anthracene when using hydrogen doped plasma gases.

For $[M+H]^+$ ion formation, the increase in signal can more easily be ascribed to an increase in proton donating species in the plasma when hydrogen is added. As noted above, in an argon discharge these proton donors may include ArH^+, H_2^+, H_3^+, or others. In a helium discharge, ions such as HeH^+, H_2^+, or H_3^+ could be formed. It could also be possible that the addition of hydrogen causes an increase in the amount of water that is protonated and formed into protonated water clusters. However, the background mass spectra, if assumed to be representative of what is really occurring in the discharge, do not support the idea of an increased abundance of protonated water clusters. H_3^+, HeH^+, and ArH^+ remain possible candidates for the increase in signal, but this is also not likely due to the lack of any increase in fragmentation of analytes. The large difference in proton affinity between H_2, He, Ar, and the analyte molecules

used would tend to produce greater amounts of fragmentation.[11, 12] It thus remains somewhat of a mystery what happens to the discharge to cause such a significant increase in signal. However, the effect is consistently reproducible.

2.6 Conclusions

Doping helium and argon with hydrogen is an effective way to increase the intensity of the obtained signal and lower the limit of detection. This type of enhancement to the analytical capabilities of ambient plasma discharges could have an important effect on studies and industries that use this type of analysis. However, it is evident from the data presented here that the parameters used in the analysis have a strong impact on the performance of the source. If one does not thoroughly understand the surroundings of a DBD, the increase in signal may not be observed due to improper grounding. These results are further evidence of the complexity of this type of discharge, and of our lack of understanding of the fundamental processes that govern their operation. Although much has been learned, there is still much to be discovered. Although these sources certainly have a place in the tool box of any analytical chemist, they may not be ideal for use in circumstances that require a more predictable ionization source that depends less on the erratic nature of ambient conditions and the surrounding environment under which the analysis takes place. However, the addition of hydrogen can be expected to enhance the analysis of many compounds under many circumstances.

2.7 References

1. Wright, J. P.; Heywood, M. S.; Thurston, G. K.; Farnsworth, P. B., *J. Am. Soc. Mass. Spectrom.* **2013,** *24*, 335-340.
2. Heywood, M. S.; Taylor, N.; Farnsworth, P. B., *Anal. Chem.* **2011,** *83*, 6493-6499.

3. Chan, G. C. Y.; Shelley, J. T.; Jackson, A. U.; Wiley, J. S.; Engelhard, C.; Cooks, R. G.; Hieftje, G. M., *J. Anal. At. Spectrom.* **2011,** *26*, 1434-1444.
4. Eiden, G. C.; Barinaga, C. J.; Koppenaal, D. W., *J. Anal. At. Spectrom.* **1996,** *11*, 317-322.
5. Koppenaal, D. W.; Eiden, G. C.; Barinaga, C. J., *J. Anal. At. Spectrom.* **2004,** *19*, 561-570.
6. Ellis, W. C.; Lewis, C. R.; Openshaw, A. P.; Farnsworth, P. B., *J. Am. Soc. Mass. Spectrom.* **2016,** *27*, 1539-1549.
7. Hanley, D. C.; Harris, J. M., *Anal. Chem.* **2001,** *73*, 5030-5037.
8. Jackson, A. U.; Garcia-Reyes, J. F.; Harper, J. D.; Wiley, J. S.; Molina-Diaz, A.; Ouyang, Z.; Cooks, R. G., *Analyst* **2010,** *135*, 927-933.
9. Venter, A. R.; Douglass, K. A.; Shelley, J. T.; Hasman, G.; Honarvar, E., *Anal. Chem.* **2013,** *86*, 233-249.
10. Shelley, J. T.; Wiley, J. S.; Chan, G. C.; Schilling, G. D.; Ray, S. J.; Hieftje, G. M., *J. Am. Soc. Mass. Spectrom.* **2009,** *20*, 837-844.
11. Herman, J. A.; Harrison, A. G., *Can. J. Chem.* **1981,** *59*, 2125-2132.
12. Herman, J. A.; Harrison, A. G., *Org. Mass Spectrom.* **1981,** *16*, 423-427.

3 METAL SAMPLING USING AMBIENT PLASMA DISCHARGES

3.1 Sampling Solid Metals at Atmospheric Pressure by Plasma Discharge

One of the unexpected results from the work experimenting with the use of hydrogen-doped argon to increase the signal intensity of organic analytes was the presence of metal and metal-containing ions in the background mass spectra of the AC glow discharge. Specifically, due to the use of a copper ground electrode, copper ions as well as various adduct ions with water and ammonia were observed in the mass spectra. The number of these ions generated by the discharge increased substantially when using H_2/Ar compared to pure argon. The same ions were observed when using helium and H_2/He as the plasma gases for the AC discharge; however, the number of ions generated was not significantly different when using H_2/He as compared to pure helium.[1] We theorized that this effect might prove useful for sampling solid metals under ambient conditions and for performing elemental analysis of metals. In addition, the source had potential for being used as a sampling source for an inductively coupled plasma (ICP) to avoid having to dissolve and digest solid metal samples.

As mentioned in the introductory chapter, metals have been sampled for the purpose of doing elemental analysis by introducing aqueous solutions into an ICP, sputtering solid metals using low pressure glow discharges, and ablating solid samples using laser induced breakdown spectroscopy (LIBS). In addition, metal sampling has been demonstrated by Xing et al.[2] using a

small dielectric barrier discharge (DBD). They used a DBD generated in a fused silica capillary to remove metal from a surface. The discharge and sample were contained in a small flow cell. The metal was then flowed into an ICP-MS for detection. According to their paper, they were able to quantify the trace elements in stainless steel standards. They also used their set up to measure the thickness of thin layers deposited on a surface. This method proved the ability of a plasma discharge to remove material from a metallic surface under ambient conditions. However, the need for a flow cell and a secondary ionization source placed some limits on the capabilities and applications of this source. We also performed experiments using a micro DBD similar to that described by Xing et al. to compare its performance to that of a H_2/Ar AC glow discharge both directly with a time-of-flight mass spectrometer and with an ICP-MS.

Signal enhancement for elemental analysis using H_2-doped argon with low pressure glow discharges has been observed by other researchers. This so called "hydrogen effect" has been characterized by those working with glow discharges under reduced pressure for elemental analysis via mass spectrometry and optical emission spectroscopy.[3-12] They have found that the addition of hydrogen increases both the number of ions detected by a mass spectrometer as well as the intensity of emitted light from a surface exposed to a plasma discharge. We have taken this concept further by performing the analysis at atmospheric pressure and with samples with varying shapes and sizes rather than just flat surfaces that are ideal for analysis.

3.2 Experimental

3.2.1 Glow Discharge

The AC glow discharge used in this study has been described previously,[1, 13] and is described briefly here. The discharge was formed in a glass tube (3.8 mm id, 6.4 mm od),

between a tungsten needle (1 mm diameter) and a metal sample as shown schematically in figure 3-1. Voltage was applied to the tungsten pin by a radio frequency power supply (ENI HPG-2, MKS Instruments, Andover, MA). The sample metal was grounded. The power applied to the discharge was 10 W at a frequency of 325 kHz. The plasma gas was 2.90 % H_2 in Ar (Airgas, Radnor, PA). Gas flow was maintained at 2 L min^{-1} when using the time-of-flight mass spectrometer (TOF-MS) and 1 L min^{-1} when using the inductively coupled plasma mass spectrometer (ICP-MS) using a mass flow controller (MKS1170A, MKS Instruments) with its corresponding power supply/readout (MKS246C, MKS Instruments). Ultra-high purity argon (99.999 % Ar) (Airgas) was also used in some experiments. A second MKS mass flow controller with a power supply/readout was used to control the flow output when required. The outputs of the two mass flow controllers then came together before going to the discharge.

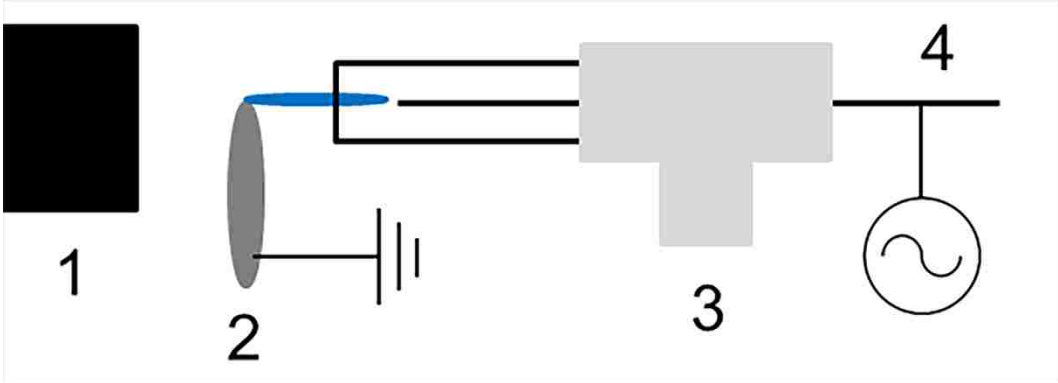

Figure 3-1 : Schematic representation of the AC glow discharge being used with a metal sample. The numbers represent the mass spectrometer inlet (1), the grounded metal sample (2), the Teflon Swagelok T (3), and the tungsten pin to which voltage was applied (4).

3.2.2 Dielectric Barrier Discharge

The DBD used in this study is based on the design used by Xing et al.,[2] but was adjusted slightly. The discharge was generated in a fused silica capillary (id 182 µm, od 354 µm). Two copper tape electrodes were attached to the outside of the capillary. Each electrode was 6 mm

wide. The electrodes were spaced 10 mm apart. The downstream electrode was between 1.5 and 2 mm from the end of the capillary. Voltage was applied to the downstream electrode while the upstream electrode was grounded. Voltage was applied by a power supply built in house utilizing an automobile ignition coil. The voltage output was 9.7 kV_{pp} at a frequency of 4.5 kHz. Helium flow was controlled using the MKS mass flow controllers and was set at 200 mL min^{-1} when using the TOF-MS and 300 mL min^{-1} when using the ICP-MS.

3.2.3 Time-of-Flight Mass Spectrometer Set Up

A time-of-flight mass spectrometer (micrOTOF II, Bruker Daltonics, Billerica, MA) was used to acquire mass spectra. To accommodate the plasma ionization source, the ESI source and the spray shield were removed unless otherwise noted. A second mechanical vacuum pump was attached to the first vacuum stage to alleviate the strain placed on the vacuum system when introducing helium. Once a sample was analyzed, the elements present as well as any adducts were identified based on m/z value and the isotope distribution. ChemCalc.org was used to match the isotope distributions observed to the actual distributions and to compare the obtained m/z value to the literature values.[14] In all cases, the sample was put in position before igniting the discharge to prevent the plasma from arcing to the MS inlet and damaging the MS inlet capillary or electronics systems.

3.2.4 Metal Samples

Samples included metal pieces that were varied in terms of their shape and composition. They included iron wire, nickel chromium wire, an aluminum ingot containing 2 % scandium, a silver ring, a titanium ring, a glass microscope slide coated with gold, a piece of stainless steel, and pieces of pure copper, magnesium, zinc, antimony, calcium, scandium, chromium, lead,

bismuth, cadmium, tin, cobalt, and tungsten. When performing the sampling with the time-of-flight mass spectrometer, the pieces were placed between the MS inlet and the discharge tube. Two metal salts were also analyzed. Solutions of each salt in HPLC grade methanol were made at a concentration of 1000 ppm. A few mL of the solution were deposited on the edge of a stainless steel slide and allowed to dry before performing the analysis. The salts analyzed included copper(II) chloride and zinc chloride.

To determine if the source could differentiate between brass types, 6 different alloys of brass and 1 type of bronze (McMaster-Carr, Santa Fe Springs, CA) were analyzed. The alloys included brasses 260, 353, 360, 385, 464, 485, and bronze 316. Each alloy consisted mostly of copper and differed from other alloys primarily in the relative abundances of zinc, lead, and tin. Each type of brass was analyzed 10 times for 60 seconds each. Prior to analysis, brass samples were rinsed in acetone to remove any surface contaminants. An average mass spectrum was then generated for each analysis, giving 10 mass spectra per sample. The results were processed using principal component analysis (PCA) using PLS Toolbox software (Eigenvector Research Inc., Manson, WA). Five components accounted for over 93 % of the variance. Each mass spectrum was normalized to unit area, mean centered, and Poisson scaled[15] prior to performing PCA. Also, all peaks with a positive mass deficit were considered chemical noise from organic contaminants and were removed from the analysis. One spectrum of brass 260 was considered an outlier and not included in the analysis.

Thermal images of copper exposed to the plasma were taken with a Ti27 thermal imager (Fluke, Everett, WA, USA). The emissivity setting was set to 0.65 for unpolished copper. The temperature was recorded after it stopped rising, which took between 1 and 2 minutes.

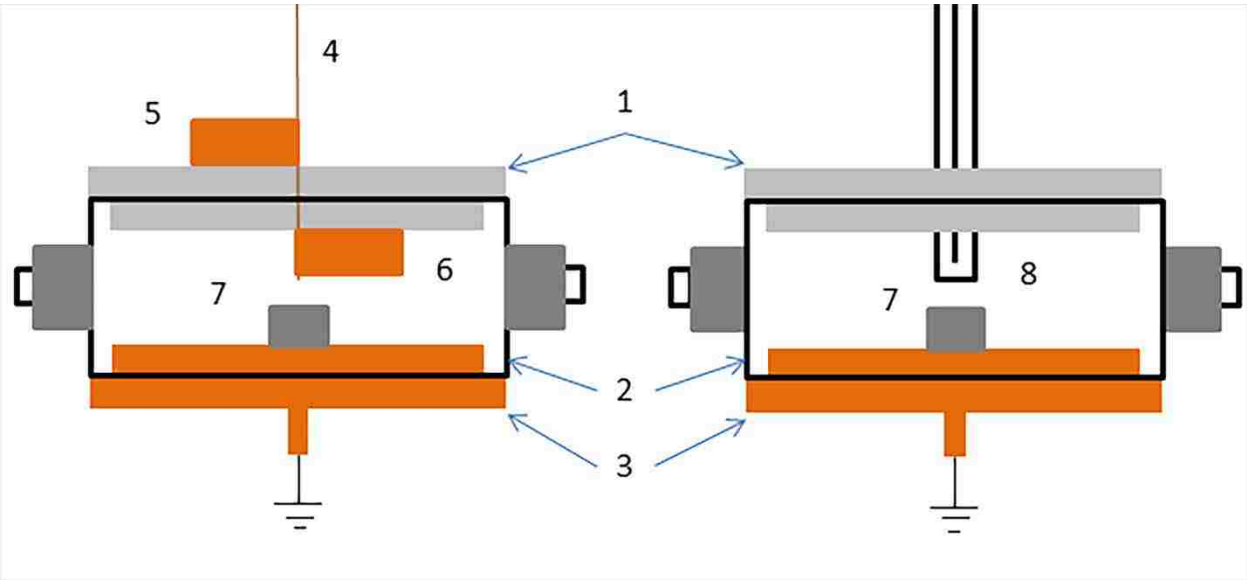

Figure 3-2 : A schematic representation of the flow used with the DBD (left side) and AC glow discharge (right side). The numbers correspond to the lid of the flow cell (1), the Teflon body of the cell (2), the copper floor of the cell (3), the fused silica capillary of the DBD (4), the copper ground electrode for the DBD (5), the copper high voltage electrode for the DBD (6), the metal sample (7), and the glow discharge tube (8).

3.2.5 Inductively Coupled Plasma Mass Spectrometer Set Up

Experiments were performed where the glow discharge and DBD sources were used to perform sampling for an ICP-MS instrument (820-MS, Varian, Walnut Creek, CA). For these experiments, the ICP nebulizer was removed, and a small flow cell, built in house, was used to house the plasma discharge and sample. The flow cell was cylindrical in shape with an inside diameter of ~ 1.5 inches and a height of 1 inch. The body of the cell was composed of Teflon. The lid of the cell was composed of poly(methyl methacrylate). One lid was built to accommodate the glow discharge, and another was built to accommodate the DBD source. The

floor of the cell was made of copper to allow grounding of metal samples. The nebulizer flow from the ICP-MS was directed through this cell to sweep metal removed by the plasma sources into the ICP. The flow cell set up is shown schematically in figure 3-2.

3.2.6 Scanning Electron Microscope Images

Scanning electron microscope (SEM) images were taken on a Helios 600 NanoLab DualBeam instrument (FEI, Hillsboro, OR). The electron beam energy was set to 5 kV. The surfaces imaged were pure copper pieces in the shape of microscope slides. For one set of images, the slide was polished to a mirror finish using a polishing wheel with 0.3-µm alumina polishing powder. A second surface was left as found and only rinsed with acetone to remove any surface contamination that would interfere with the imaging. Six different spots on each slide were exposed to the plasma for varying amounts of time: 5 sec, 15 sec, 30 sec, 1 min, 2 min, and 5 min. The slide was 3 mm away from the end of the discharge tube when exposed. These experiments were performed once for pure argon and once for 2.90 % H_2/Ar plasma gases.

3.3 Results and Discussion

3.3.1 Detectable Metals

In positive ion mode, the elements that were detected by the TOF-MS using the glow discharge as the ionization source included magnesium, aluminum, calcium, iron, cobalt, copper, zinc, silver, cadmium, tin, antimony, gold, lead, and bismuth. In negative ion mode, only tin was detectable. In many cases, atomic ions were generated; however, in all cases adducts of the metal ions with water and ammonia from the plasma discharge were formed in various combinations and sizes. For example when analyzing cadmium, the ions observed included Cd^+,

$Cd(NH_3)^+$, $Cd(H_2O)^+$, $Cd(NH_3)_2^+$, $Cd(NH_3)(H_2O)^+$, $Cd(H_2O)_2^+$ and other higher mass adducts. When analyzing salts, the same adducts were detected as with the solid metal samples. Table 3-1 summarizes the detected adducts for each metal analyzed. The metals that were not detected were scandium, titanium, chromium, nickel, and tungsten. The metals that were not detected tended to be those with the highest melting points, though this was not true in the case of nickel whose melting point is lower than those of both cobalt and iron. Cobalt and iron were both detectable.

The detection of adduct peaks leads to more involved interpretation and deconvolution of mass spectra; however, even without exact mass measurements the metals being sampled can be identified based largely on the isotope distributions and the differences in mass between peaks. The mass spectrometer used in this study was not equipped with the capability to perform MS/MS analyses; however, it is reasonable to assume that if a collision cell were used it would significantly increase the amount of atomic ions observed by breaking up the adduct ions and make the interpretation of the spectra easier.

The helium DBD described showed similar results to the glow discharge source in terms of showing both atomic ions and adducts. It was able to sample more types of metals including a stainless steel sample that contained chromium and nickel. However, we found that there was a small filament of visible plasma that connected the high voltage electrode and the sample under the operating conditions described. When a DBD was used with a capillary that extended 1 cm beyond the high voltage electrode the filament was no longer observed, but the signal from metal ions and adducts also no longer appeared in the mass spectra. This shows that the DBD we used does not sample metal unless it is aided by a filament when it is in the open air. This filament changes the characteristics of the discharge to be more similar to a glow discharge.

Table 3-1 : Listing of the ions observed for each metal sampled with the AC glow discharge using the TOF-MS. Elements are listed in order of increasing atomic number. All ions were singly charged.

Element	Positive ions	Negative ions
Magnesium	$Mg(NH_3)(H_2O)$, $Mg(NH_3)(H_2O)_2$, $Mg(NH_3)_4$, $Mg(NH_3)_3(H_2O)$, $Mg(NH_3)(H_2O)_3$, $Mg(NH_3)_4(H_2O)$, $Mg(NH_3)_3(H_2O)_2$	
Aluminum	$Al(NH_3)_2(H_2O)$, $Al(NH_3)_4$, $Al(NH_3)_3(H_2O)$, $Al(NH_3)_2(H_2O)_2$	
Calcium	$CaNH_3$, $Ca(NH_3)_2(H_2O)$, $Ca(NH_3)(H_2O)_2$, $Ca(H_2O)_3$	
Iron	FeO, $Fe(NH_3)$	
Cobalt	$Co(NH_3)_2$, $Co(NH_3)(H_2O)$, $Co(NH_3)_3$, $Co(NH_3)_2(H_2O)$, $Co(NH_3)(H_2O)_2$	
Copper	Cu, $CuNH_3$, CuH_2O, $Cu(NH_3)_2$, $Cu(NH_3)(H_2O)$, $Cu(H_2O)_2$	
Zinc	Zn, $ZnNH_3$, ZnH_2O, $Zn(NH_3)_2$, $ZnNH_3H_2O$, $Zn(H_2O)_2$, $Zn(NH_3)_3$, $Zn(NH_3)_2(H_2O)$, $Zn(H_2O)_2(NH_3)$, $Zn(H_2O)_3$	
Silver	Ag, $Ag(NH_3)$, $Ag(H_2O)$	
Cadmium	Cd, $CdNH_3$, CdH_2O, $Cd(NH_3)_2$, $Cd(NH_3)(H_2O)$, $Cd(H_2O)_2$, $Cd(NH_3)_3$	
Tin	Sn, $SnNH_3$, $Sn(NH_3)(H_2O)$, $Sn(NH_3)(H_2O)_2$, $Sn(NH_3)_4$, $Sn(NH_3)_4(H_2O)$	$SnO_2(H_2O)$,$SnHO_2(H_2O)$,$Sn(O_2)_2(H_2O)$, $SnH(O_2)(H_2O)$
Antimony	Sb, $Sb(NH_3)$, $Sb(NH_3)_2$, $Sb(NH_3)_3$, $Sb(NH_3)_2(H_2O)$, $Sb(NH_3)_4$, $Sb(NH_3)_3(H_2O)$, $Sb(NH_3)_2(H_2O)_2$, $Sb(NH_3)_5$, $Sb(NH_3)_4(H_2O)$, $Sb(NH_3)_6$, $Sb(NH_3)_5(H_2O)$	
Lead	Pb, $PbNH_3$, $Pb(NH_3)_2$, $Pb(NH_3)(H_2O)$, $Pb(NH_3)_3$.	
Bismuth	Bi, $Bi(NH_3)_2$, $Bi(NH_3)_3$, $Bi(NH_3)_2(H_2O)$, $Bi(NH_3)_3(H_2O)$, $Bi(NH_3)_2(H_2O)_2$, BiO, $BiNH_3$, $Bi(H_2O)$, $BiO(NH_3)$	

As is the case when using many other ambient ionization sources, a high chemical background was observed in the mass spectra due to the presence of various impurities in the lab air. These include ubiquitous substances found in laboratories such as vacuum pump oil,

plasticizers, and volatile solvents.[16] However, due to the negative mass defects of most metals, these peaks did not interfere strongly with the analysis. With the resolving power of most modern mass spectrometers, the peaks for metal ions and adducts appear as separate peaks with slightly lower m/z values than those corresponding to the chemical background. The best signal to background was obtained by analyzing a sharp edge or corner of the sample.

3.3.2 Effects of Changing the Percent Hydrogen in Argon

By changing the percent H_2 in argon from 0 % to 2.9 %, we were able to observe the effect of H_2 concentration on the detected signal. For these experiments, the copper electrode used in previous studies[1, 13] was attached to the end of the glow discharge tube to eliminate the effect sample positioning has on the signal intensity. The results, presented in figure 3-3, showed that varying the amount of H_2 in the plasma gas had relatively small effects on the signal intensity. However, when pure argon was used as the plasma gas, the signal decreased to a very low value, showing that the H_2 addition is essential for observing the effects we describe. A significant copper signal was attainable with only 0.1 % H_2 added to argon. This experiment was repeated with a brass sample. Copper and zinc behaved similar to the trend in figure 3-3, but the lead ions increased in intensity with each increase in H_2 concentration. So, even though not all elements respond in the same way to the increase in H_2 concentration, increasing the amount of H_2 was shown to increase the signal for several elements. The change in H_2 concentration affected both the atomic ion peaks and the adduct peaks equally. It should be noted that the orientation of the sample relative to the discharge and the MS inlet has significant effects on the signal obtained. For this reason, we used 2.9 % H_2 in Ar for all analyses to assure the presence of adequate amounts of H_2 in the area of the analysis.

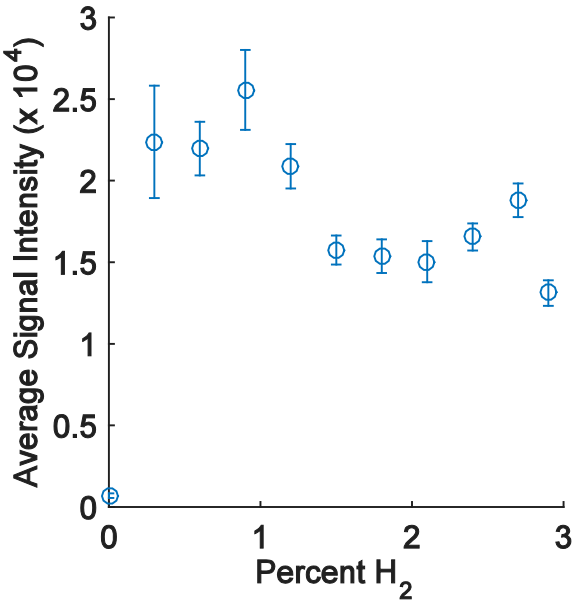

Figure 3-3 : Graph showing the change in signal intensity of the $Cu(NH_3)(H_2O)^+$ ion as a function of H_2 concentration in argon. The error bars represent 1 standard deviation.

3.3.3 ICP-MS Analysis with the Glow Discharge

Those elements that were not detectable using the TOF-MS with the glow discharge source included chromium, titanium, scandium, tungsten, and nickel. These are all relatively high melting point metals that are considered refractory. In particular, the H_2/Ar glow discharge was unable to detect any elements from a stainless steel sample when used with the TOF-MS. We theorized that these elements may still be sampled by the plasma, but that the discharge may not have enough power to ionize them. To test this hypothesis, we used an ICP-MS to detect any of these elements that were not ionized and to observe the sampling tendencies of the discharge generally.

The analyses of brass using the ICP-MS showed the sampling of all the components of the brass including a small amount of tin. However, the sampling did not reflect the true percent abundances that should exist in a sample of brass 360. We found that the counts for zinc and

lead were higher than expected. Either copper was undersampled or zinc and lead were oversampled relative to the true values. It is notable that tin was detected although brass 360 has a nominal tin composition of 0%. It is likely present because tin is a common element found in brasses. This shows that even trace elements are sampled by the H_2/Ar discharge.

Brass and copper were each analyzed while the percent of H_2 in in the plasma gas was varied. The results we obtained were nearly identical to those in figure 3-3 for copper and zinc for points where H_2 was added. The traces for lead and tin also match those of copper and zinc in terms of their shape. The major exception was that the signal intensity obtained using pure argon was as intense as or more intense as that obtained when using 2.90% H_2. This shows that the pure argon discharge is still capable of removing metal atoms from the surface, but that it does not produce ions detectable by the TOF-MS without the addition of H_2.

Some refractory elements were detected using the glow discharge source with the ICP-MS. In the brass mass spectrum, tungsten ions from the needle electrode of the glow discharge were observed. Scandium was detected in the 2% scandium in aluminum sample. Although these elements were not detected using the time-of-flight mass spectrometer, it appears they are still removed from the surface by the plasma. However, the chemistry of the discharge apparently does not favor ionization of these elements. When analyzing a stainless steel sample, no ions from the steel were detected. This suggests that the perhaps the corrosion resistive properties of the steel also resist the chemical sputtering of the H_2/Ar discharge.

3.3.4 ICP-MS Analysis using the Dielectric Barrier Discharge

As reported by Xing et al.[2] the helium DBD used is able to sample stainless steel samples quantitatively and has been characterized fairly well. According to the reported results, the

authors were able to perform several types of analyses with this source including depth profiling of thin layers. Our primary purpose in performing experiments with this source was to observe the effects of adding hydrogen to the helium plasma gas in terms of signal intensity and sensitivity. Our results indicated that there is an increase in signal when using H_2/He with the DBD, but the increase was not as dramatic as was observed in the case of the argon glow discharge. The helium and H_2/He DBD were both able to sample all the elements present in the steel sample including iron, chromium, nickel, lead, molybdenum, and niobium. This again highlights the sensitivity of these discharges for sampling metals as the percent abundances of molybdenum and niobium in the steel sample analyzed were 0.391 % and 0.029 % respectively.

3.3.5 Sampling Mechanism Changes

Comparing the SEM images shows important differences in how the argon and H_2/Ar plasmas remove material from a metal surface. A comparison of the images taken of the polished copper slide exposed to argon and H_2/Ar is shown in figure 3-4. Figure 3-5 shows a comparison of the spots exposed to the pure argon and H_2/Ar plasmas for the unpolished copper slide.

For the polished slide images, the main difference between the spot exposed to pure argon (figure 3-5 panels a and c) and the spot exposed to H_2/Ar (figure 3-5 panels b and d) is the evidence of melting that can be observed for the spot exposed to H_2/Ar. The spot exposed to the pure argon discharge instead shows a smooth surface that upon closer inspection shows the formation of small craters in the surface. This difference—craters vs melting—highlights the operation of different mechanisms for removing copper atoms from the surface. The images

indicate that the H_2/Ar plasma removed material by a thermal mechanism, but show evidence for a more non-thermal sampling mechanism for the pure argon discharge.

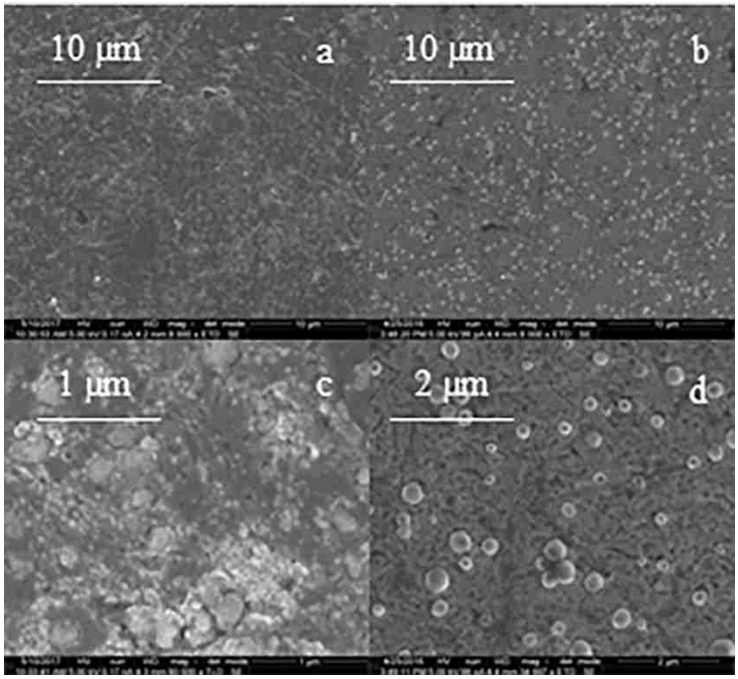

Figure 3-4 : SEM images taken of a polished pure copper slide after 300 seconds of exposure to a pure argon plasma (a and c), and a H_2/Ar plasma (b and d).

The images of the unpolished slide show similar features. The spot exposed to the pure argon discharge has craters eroded into it (see figure 3-6 panels a and c). The zoomed in images of the crater walls shows what may be some evidence of limited melting on the crater walls. However, for the spot exposed to the H_2/Ar plasma, no such craters are seen (figure 3-6 panels b and d). There is not clear evidence of melting like was seen for the polished slide after 300 seconds of exposure, but signs of melting are visible in the images of spots exposed to the discharge for less time.

In general terms, exposure to the H_2/Ar plasma appeared to do more to smooth out the surface of the unpolished slide. It melted away the microscopic peaks and valleys present on the

surface as well as removing the copper oxide layer that had formed due to extended exposure to air. The pure argon plasma did not do as much to smooth the unpolished surface in the time it was exposed to the discharge.

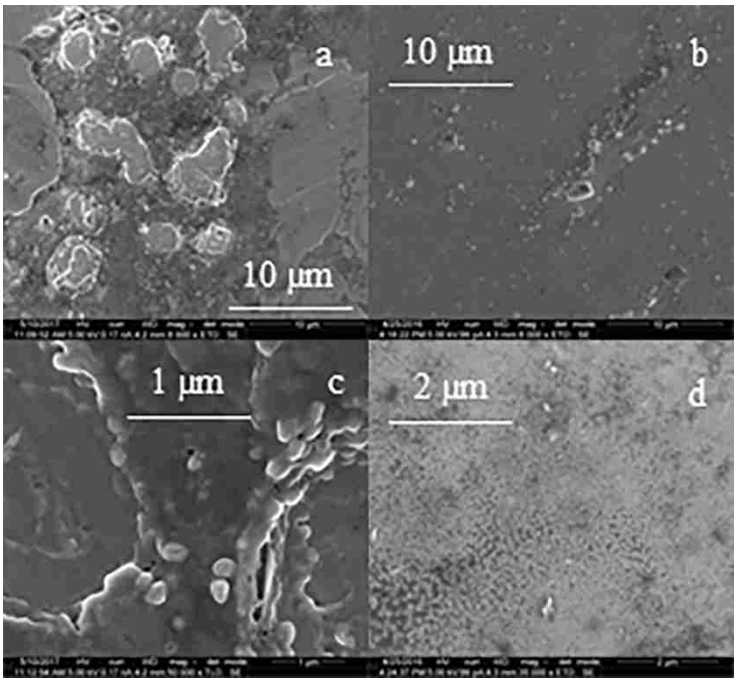

Figure 3-5 : SEM images of an unpolished copper surface exposed for 300 seconds to a pure argon discharge (a and c) and a H_2/Ar discharge (b and d).

The melting observed in these images suggests that there is a definite thermal component to the removal of the copper atoms from the surface for both the argon plasma and the H_2/Ar plasma, though the thermal component appears to be more pronounced for the H_2/Ar plasma. It may be that copper is simply evaporating off the surface such that the gas phase atoms can interact with reactive species in the plasma to become ionized and form clusters with the abundant NH_3 and H_2O molecules and ions in the active plasma discharge. However, it appears that some of the analyte removal occurs due to nonthermal processes. This is especially true of the spots exposed to the pure argon plasma. The craters that were observed were likely formed

by chemical sputtering. The same is likely true of the smaller craters formed by the H_2/Ar plasma.

When measuring the temperature of a copper slide exposed to the discharge, the maximum temperature of a slide exposed to the pure argon plasma was higher than that of a slide exposed to the H_2/Ar plasma. The temperatures were 143.5 °C and 119.5 °C respectively. The decrease in temperature when using H_2/Ar is the opposite of what one would expect if the addition of H_2 to argon enhanced the thermal sampling mechanism as is suggested by the SEM images, especially when considering the significant increase in signal with the addition of H_2. It may be that the small craters that form when the surface is exposed to the H_2/Ar plasma are the result of more widespread chemical sputtering than occurs upon exposure to the pure argon discharge. However, without the ability to precisely measure the temperature at each point on a sample with respect to time, we cannot prove whether chemical sputtering is occurring or whether localized heating causes faster evaporation with the addition of hydrogen. The localized heating may be caused by current concentrating on small spots on the sample. It is evident that some localized heating must have occurred to melt the copper since the maximum measured slide temperature was well below the melting point of pure copper (1085 °C).

Overall, the evidence is clear that the addition of H_2 to the argon plasma gas is responsible for the increase in signal when sampling solid metals. This suggests that one or more species that are more abundant in the H_2/Ar plasma than in a pure argon discharge contribute to either the thermal or nonthermal components of analyte removal or to increased ionization efficiency of the metal atoms. A computer simulation of a 1.0 % H_2/Ar glow discharge[17] calculated the formation of significant amounts of ArH^+ and H_3^+ with the addition of H_2. Others have found that the extra kinetic energy of ArH^+ ions causes sputtering to occur at a

higher rate than for Ar^+.[18] Considering these results, it might be assumed that these species play an important role in the changing sampling mechanism; however, we have no experimental evidence to show that these species are responsible for the effects observed.

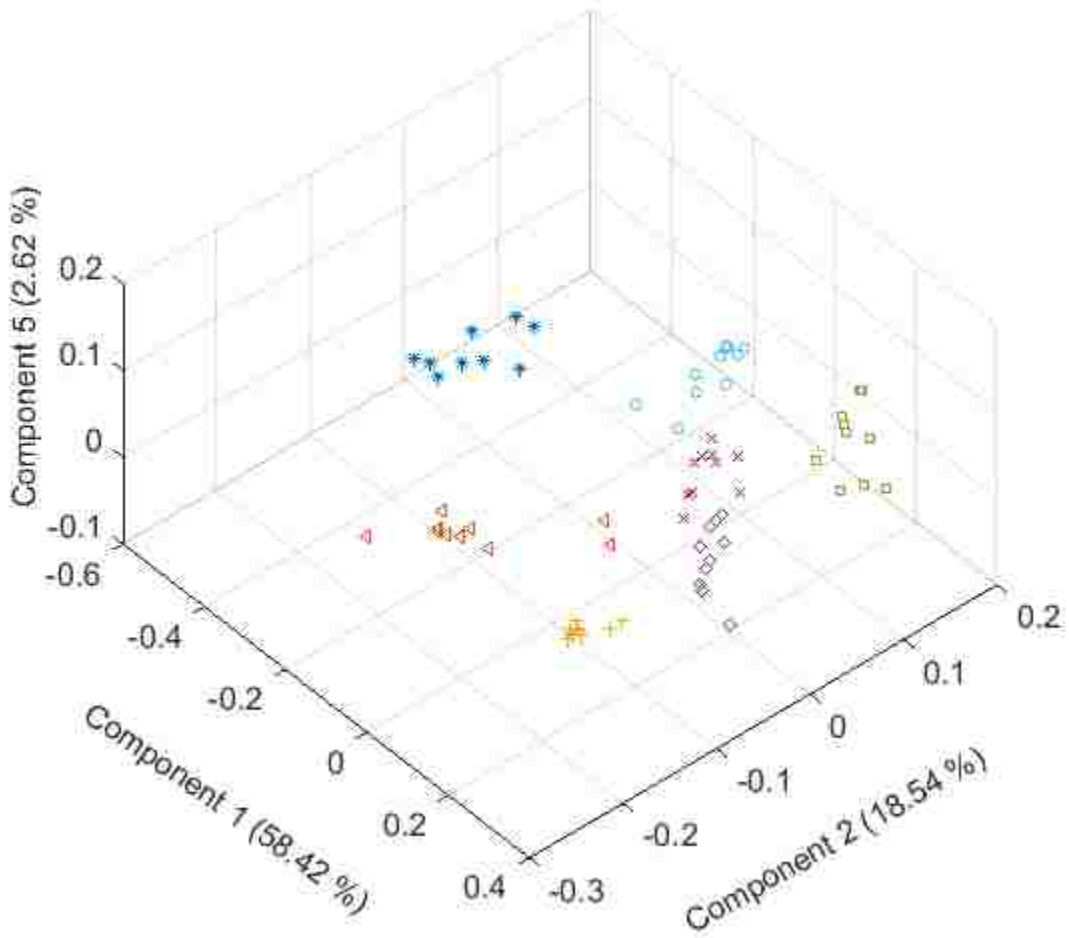

Figure 3-6 : Results of the PCA analysis of the mass spectra from analyzing different brass alloys: brass 260 (*), brass 353 (◄), brass 360 (+), brass 385 (◊), brass 464 (□), brass 485 (o), and bronze 316 (x)

3.3.6 Classification of Brass Samples

It is possible to differentiate between different alloys of the same metals based on the relative abundances of the metal ions present in the mass spectra. We analyzed 7 different brass

alloys to prove this concept. The results of the PCA analysis are shown in a plot of the scores for components 1, 2 and 5 in figure 3-6. They are satisfactorily separated on these three components. The implication of these results is that the discharge is sensitive enough to small differences in alloy composition to differentiate samples that are very similar to each other. As shown above with the ICP-MS experiments, the sampling may not reflect the true composition of the sample, but these results show that the signal intensity for each element is consistent and unique for a given alloy.

3.4 Conclusions

We have characterized a technique for the direct sampling of metal and metal salt samples under ambient conditions. This may be an important step towards the rapid qualitative sampling of unknown metals under ambient conditions to ascertain what elements are present. The potential applications for this technique may include fields such as forensics, material science, metallurgy, and quality control.

This technique can also be used with some adjustment as a method for sample introduction in ICP-MS to provide easy, rapid introduction of solid metal samples into an ICP-MS without time-consuming sample preparation steps or the need of a laser system.

The findings also suggest a potential non-thermal analyte removal mechanism when using H_2/Ar as the plasma gas. However, due to a lack of direct evidence, we were unable to definitely determine the processes occurring to remove analyte from the surface. It is evident that the chemistry involved is complex and will require more study to fully elucidate the mechanisms involved.

3.5 References

1. Ellis, W. C.; Lewis, C. R.; Openshaw, A. P.; Farnsworth, P. B., *J. Am. Soc. Mass. Spectrom.* **2016,** *27*, 1539-1549.
2. Xing, Z.; Wang, J.; Han, G.; Kuermaiti, B.; Zhang, S.; Zhang, X., *Anal. Chem.* **2010,** *82*, 5872-5877.
3. Bings, N. H.; Bogaerts, A.; Broekaert, J. A. C., *Anal. Chem.* **2004,** *76*, 3313-3336.
4. Bogaerts, A., *J. Anal. At. Spectrom.* **2002,** *17*, 768-779.
5. Fernandez, B.; Bordel, N.; Pereiro, R.; Sanz-Medel, A., *J. Anal. At. Spectrom.* **2003,** *18*, 151-156.
6. Fernandez, B.; Bordel, N.; Perez, C.; Pereiro, R.; Sanz-Medel, A., *J. Anal. At. Spectrom.* **2002,** *17*, 1549-1555.
7. Hodoroaba, V.-D.; Hoffmann, V.; Steers, E. B. M.; Wetzig, K., *J. Anal. At. Spectrom.* **2000,** *15*, 951-958.
8. Hodoroaba, V.-D.; Hoffmann, V.; Steers, E. B. M.; Wetzig, K., *J. Anal. At. Spectrom.* **2000,** *15*, 1075-1080.
9. Hodoroaba, V.-D.; Steers, E. B. M.; Hoffmann, V.; Unger, W. E. S.; Paatsch, W.; Wetzig, K., *J. Anal. At. Spectrom.* **2003,** *18*, 521-526.
10. Hodoroaba, V.-D.; Steers, E. B. M.; Hoffmann, V.; Wetzig, K., *J. Anal. At. Spectrom.* **2001,** *16*, 43-49.
11. Mason, R. S.; Miller, P. D.; Mortimer, I.; Mitchell, D. J.; Dash, N. A., *Phys. Rev. E: Stat. Phys., Plasmas, Fluids,* **2003,** *68*, 016408.
12. Menendez, A.; Pisonero, J.; Pereiro, R.; Bordel, N.; Sanz-Medel, A., *J. Anal. At. Spectrom.* **2003,** *18*, 557-563.
13. Reininger, C.; Woodfield, K.; Keelor, J. D.; Kaylor, A.; Fernández, F. M.; Farnsworth, P. B., *Spectrochim. Acta B* **2014,** *100*, 98-104.
14. Patiny, L.; Borel, A., *J. Chem. Inf. Model.* **2013,** *53*, 1223-1228.
15. Keenan, M. R.; Kotula, P. G., *Surf. Interface Anal.* **2004,** *36*, 203-212.
16. Brüggemann, M.; Karu, E.; Hoffmann, T., *J. Mass Spectrom.* **2016,** *51*, 141-149.
17. Bogaerts, A.; Gijbels, R., *Spectrochim. Acta B* **2002,** *57*, 1071-1099.
18. Budtz-Jørgensen, C.; Kringhøj, P.; Bøttiger, J., *Surf. Coat. Technol.* **1999,** *116*, 938-943.

4 COMPUTER MODEL OF A DC GLOW DISCHARGE USED FOR ADI-MS

4.1 Scope of the Simulation

As described in the first chapter, carrying out computer simulations is often a good method for exploring the fundamental processes of gas flow and chemistry in plasma discharges. The computational study of the FAPA done by Bogaerts et al.[1] provided insight into the chemistry that happens between helium and nitrogen species in the active discharge region of a DC glow discharge. However, most samples interact with species from the plasma in the afterglow region of the discharge rather than in the active discharge region. Also, to form a more complete picture of the chemistry that occurs both in the active discharge region and in the afterglow, reactions with water need to be included. To have the most significant impact possible, the simulation described in this chapter was designed to include reactions involving water and several centimeters of space in the afterglow region of the discharge. To give the simulation a foundation, experimental data measuring the absolute number densities of He_m atoms in the DC discharge were used as an anchor to which calculated densities could be tied. This work essentially extends the work of Bogaerts and coworkers in a way that provides more detailed information and insight into the function of a plasma-based ADI source.

4.2 Experimental

4.2.1 DC Discharge

The DC discharge used for this model has been described in detail elsewhere.[2] Briefly, the discharge was created in a glass tube (3.8 mm i.d., 6.3 mm o.d.) between a high voltage tungsten pin electrode (1 mm diameter) and a grounded copper electrode attached to the end of the glass tube. The copper electrode had a 2 mm hole to allow for the flow of gas. The voltage applied to the tungsten pin was approximately -444 V with a constant current of 25.0 mA applied by a high voltage DC power supply (BHK 1000-0.2 MG, KEPCO, Inc., Flushing, NY, USA). Ultra-high purity helium (99.999 % He) (Airgas, Radnor, PA, USA) was used as the plasma gas. It was flowed at a rate of 2 L min^{-1} regulated by a mass flow controller (MKS1170A, MKS Instruments, Andover, MA, USA) with its power supply/readout (MKS246C, MKS Instruments, Andover, MA, USA).

The absolute number densities of He_m were measured by Charlotte Reininger in our lab using an atomic absorption spectrometer that is described in detail in reference 15. The limit of detection for the absorption spectrometer was approximately 3 x 10^{15} m^{-3}. Values for the number densities of He_m were obtained at 13 points along the axial length of the active discharge region between the tungsten pin electrode and the copper plate electrode. The numbers obtained were line-of-sight averages. He_m densities downstream from the copper electrode were below the detection limit.

These experimental data points were used as a basis for the computational work. The line-of-sight averages were converted into number densities at given points in the simulated region by multiplying measured value by the path length of the discharge tube and treating the

result as an integral from which a Gaussian distribution was calculated in the radial direction. The width of the Gaussian was assumed to be the width of the visible plasma. A Gaussian distribution was calculated for each 0.0625 mm step along the axis of the discharge.

4.2.2 Software and Simulation Conditions

The simulation was assumed to be axisymmetric, so, one x y plane in cylindrical coordinates was considered to be representative of all azimuthal angles. The area of the discharged modeled in the simulation is shown in figure 4-1.

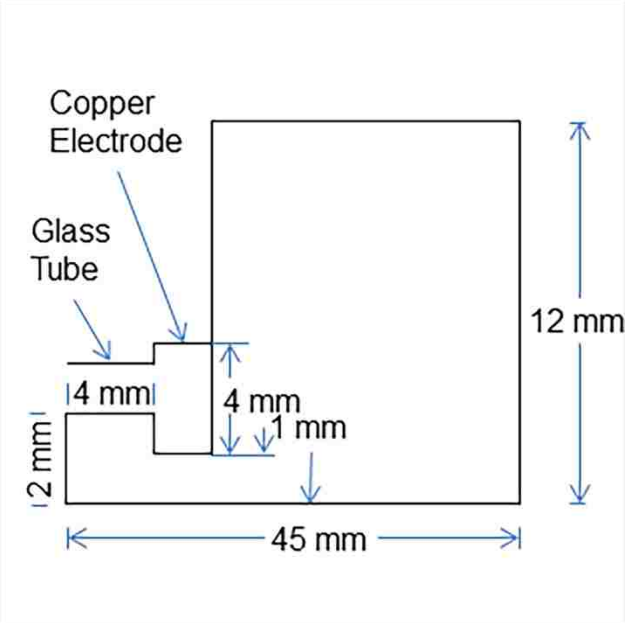

Figure 4-1 : A representation of the area simulated including the active discharge region and the afterglow of the DC discharge. The drawing is not to scale. The gas flow goes from left to right in the figure.

The simulation was carried out using two pieces of software. The flow dynamics of the helium flowing into air were calculated using Star-CCM+ (CD-adapco, Melville, NY, USA). The helium flow was mainly laminar. Based on the power applied to the discharge (11.1 W), the flow rate, and the heat capacity of helium, a temperature of 690 K was calculated for the He gas. The results obtained from Star-CCM+ included the mole fractions of air and helium at each point,

the axial and radial components of the gas velocities at each point, and the temperature. The data were exported on a uniform grid with the distance between adjacent points being 0.0625 mm along the axis and in the radial direction.

The chemical kinetics portion of the simulation was carried out using MATLAB (MathWorks, Natick, MA, USA). The equations used to model the kinetics are described in detail below in the theory section. See the appendix for the codes used.

4.3 Theory

The DC discharge modeled in this study is a continuous discharge, as opposed to the dielectric barrier discharge (DBD) and some other discharges driven by AC voltage, so the DC discharge does not produce plasma bullets[3-5] or any other discontinuous plasma events. The discharge is assumed to reach a steady state rapidly after ignition in terms of gas flow and chemical reactions.

The following models were used in the physics continuum of Star-CCM+ for the flow dynamics. The area was assumed to be axisymmetric and the simulation was run until it reached a steady state. The gases were modeled as a multi-component mixture that did not react and consisted of ideal gases. The flow and species were segregated, as was the fluid enthalpy. The flow regime was set to laminar. The air was assumed to have water content equivalent to 30 % relative humidity unless otherwise noted. The helium was assumed to contain 1 ppm water and 5 ppm nitrogen unless otherwise noted. These impurity concentrations are those reported by Airgas for its ultra-high purity helium.

The boundary conditions were as follows: the faces that correspond to glass or metal were set as walls, the faces that exist in the open air were set as pressure outlets, and the face

where the helium entered the simulation area was set as a velocity inlet. The velocity profile was assumed to follow a Poiseuille profile. The profile was calculated using the following equation:

$$u(r) = 2u_{avg}\left(1 - \frac{r^2}{R^2}\right) \quad 4\text{-}1$$

In this equation u is the velocity at a given radius, u_{avg} is the average velocity of the flow, r is the radius from the center of the tube to the point where the velocity is being measured, and R is the radius of the tube through which the gas is flowing. The value for u_{avg} was calculated using the following equation:

$$u_{avg} = \frac{(\frac{2I}{5P} + V)}{\pi R^2} \quad 4\text{-}2$$

In this equation u_{avg} is the average velocity, I is the power applied to the discharge in Watts, P is the air pressure in Pascals, V is the volumetric flow rate in $m^3\ s^{-1}$, and R is the radius of the tube through which the gas flows in meters. The factor of 2/5 accounts for the specific heat of helium. Equation 4-2 is based on the assumptions that all the power applied to the helium is uniformly deposited over the active discharge region and converted into heat, that the temperature increase is uniformly distributed radially, that the velocity is uniformly distributed radially, and that any pressure change due to heating or gas flow is negligible. Using equations 4-1 and 4-2, the velocity profile for helium was calculated and applied to the velocity inlet in the simulation in Star-CCM+.

As mentioned above, it was assumed that the plasma reaches a steady state rapidly after being ignited. The discharge then reaches a balance of flow and chemical kinetics that is approached in time by means of the following set of equations for each species i:

$$\frac{\partial n_i}{\partial t} = -\nabla \cdot (\vec{v} n_i)) + \nabla \cdot (D_i \nabla n_i) + C_{ij} n_j \qquad 4\text{-}3$$

In this equation, n_i is the number density of a given species, t is time, D_i is the diffusion constant for species n_i, $\vec{v}$ is the velocity as obtained from the Star-CCM+ simulation, and $C_{ij}n_j$ represents the sum of all sources and losses from chemical reactions. The diffusion constants were calculated using the Fuller-Schetler-Giddings equation for diffusion of each species in both helium and air.[6] The two diffusion constants for each species were then combined using a density weighted average at each point in the simulation. Equation 4-3 represents a sum of three factors: the first is diffusion, the second is convection, and the third takes into account a given species being generated or lost due to chemical reactions. The list of chemical reactions used in this model is included in table 4-1. Rate constants were taken from literature sources.[1, 7-16]

In equation 4-3 there is no implied sum on i in the diffusion term, but in the chemical reaction term $C_{ij}n_j$, the implied sum on j indicates matrix multiplication, which couples the various species equations together. Under the conditions of this study the rates of change produced by the terms of the matrix C_{ij} are much larger than those of the flow and diffusion terms. This makes it possible to find the steady-state solution of equation 4-3 by using time-explicit second-order accurate centered finite-differences on a uniform radial and axial grid for the convection and diffusion terms, and by making the chemical reaction term implicit, as follows:

$$\frac{n_i^{m+1} - n_i^m}{\Delta t} = L_{CD}(n_i^m) + C_{ij} n_j^{m+1} \rightarrow n_i^{m+1} = \left(I_{ij} - C_{ij}\Delta t\right)^{-1}(n_j^m + \Delta t L_{CD} n_j^m) \qquad 4\text{-}4$$

Table 4-1 : List of reactions and rate constants used in the simulation from the literature. An "*" denotes that the rate constant was estimated from similar reactions found in the literature. The rate constant for the Penning ionization of water by He_m was estimated based on the relative collisional cross sections of the Penning ionizations of water and nitrogen by He_m. Where multiple products were possible, but none were included in the simulation, "products" was listed

Reaction Num.	Reaction	Rate Constant	Ref
1	$He_m + N_2 \rightarrow N_2^+ + He + e^-$	7.11×10^{-11} cm^3 s^{-1}	14
2	$He_2^+ + N_2 \rightarrow 2He + N_2^+$	1.3×10^{-9} cm^3 s^{-1}	1
3	$He^+ + N_2 \rightarrow He + N_2$	1.6×10^{-9} cm^3 s^{-1}	1
4	$He^+ + H_2O \rightarrow He + H_2O^+ + e^-$	5.6×10^{-10} cm^3 s^{-1}	1
5	$He^+ + 2e^- \rightarrow He_m + e^-$	3×10^{-20} cm^6 s^{-1}	1
6	$He^+ + 2e^- \rightarrow He + e^-$	3×10^{-20} cm^6 s^{-1}	1
7	$He^+ + 2He \rightarrow He_2^+ + He$	1.1×10^{-31} cm^6 s^{-1}	1
8	$2He_m \rightarrow He_2^+ + e^-$	1.5×10^{-9} cm^{3}s^{-1}	1
9	$2He_m \rightarrow He^+ + He + e^-$	1.5×10^{-9} cm^{3}s^{-1}	1
10	$He_2^+ + e^- \rightarrow He_m + He$	8.9×10^{-9} cm^{3}s^{-1}	1
11	$He_m + H_2O \rightarrow He + H_2O^+ + e^-$	1.4×10^{-9} cm^3 s^{-1}	9,13
12	$N_2^+ + 2N_2 \rightarrow N_4^+ + N_2$	1.4×10^{-29} cm^6 s^{-1}	10
13	$N_2^+ + e^- \rightarrow N_2$	3.5×10^{-7} cm^3 s^{-1}	12
14	$N_2^+ + H_2O \rightarrow H_2O^+ + N_2$	2.8×10^{-9} cm^3 s^{-1}	15
15	$N_4^+ + H_2O \rightarrow H_2O^+ + 2N_2$	1.88×10^{-9} cm^3 s^{-1}	7
16	$N_4^+ + e^- \rightarrow 2N_2$	2.60×10^{-6} cm^3 s^{-1}	11
17	$N_4^+ + N_2 \rightarrow N_2^+ + 2N_2$	2.5×10^{-15} cm^{3}s^{-1}	1
18	$N_4^+ + He \rightarrow N_2^+ + N_2 + He$	2.5×10^{-15} cm^{3}s^{-1}	1
19	$H_2O^+ + H_2O \rightarrow H_3O^+ + OH^\cdot$	1.67×10^{-9} cm^3 s^{-1}	7
20	$H_3O^+ + H_2O + He \rightarrow (H_2O)_2H^+ + He$	6.65×10^{-28} cm^6 s^{-1}	7
21	$H_3O^+ + H_2O + N_2 \rightarrow (H_2O)_2H^+ + N_2$	3.4×10^{-27} cm^6 s^{-1}	10
22	$(H_2O)_2H^+ + He \rightarrow H_3O^+ + H_2O + He$	7×10^{-26} cm^3 s^{-1}	*
23	$(H_2O)_2H^+ + N_2 \rightarrow H_3O^+ + H_2O + N_2$	7×10^{-26} cm^3 s^{-1}	10
24	$(H_2O)_2H^+ + H_2O + He \rightarrow (H_2O)_3H^+ + He$	1.51×10^{-26} cm^6 s^{-1}	8
25	$(H_2O)_2H^+ + H_2O + N_2 \rightarrow (H_2O)_3H^+ + N_2$	2.3×10^{-27} cm^6 s^{-1}	10
26	$(H_2O)_3H^+ + He \rightarrow (H_2O)_2H^+ + H_2O + He$	4×10^{-15} cm^3 s^{-1}	8
27	$(H_2O)_3H^+ + N_2 \rightarrow (H_2O)_2H^+ + H_2O + N_2$	7×10^{-18} cm^3 s^{-1}	10
28	$(H_2O)_3H^+ + H_2O + He \rightarrow (H_2O)_4H^+ + He$	1.5×10^{-27} cm^6 s^{-1}	8
29	$(H_2O)_3H^+ + H_2O + N_2 \rightarrow (H_2O)_4H^+ + N_2$	2.4×10^{-27} cm^6 s^{-1}	10
30	$(H_2O)_4H^+ + He \rightarrow (H_2O)_3H^+ + H_2O + He$	4×10^{-15} cm^3 s^{-1}	7
31	$(H_2O)_4H^+ + N_2 \rightarrow (H_2O)_3H^+ + H_2O + N_2$	4×10^{-14} cm^3 s^{-1}	10
32	$(H_2O)_4H^+ + H_2O + He \rightarrow (H_2O)_5H^+ + He$	1×10^{-26} cm^6 s^{-1}	*
33	$(H_2O)_4H^+ + H_2O + N_2 \rightarrow (H_2O)_5H^+ + N_2$	2.5×10^{-27} cm^6 s^{-1}	10
34	$(H_2O)_5H^+ + He \rightarrow (H_2O)_4H^+ + H_2O + He$	2×10^{-10} cm^3 s^{-1}	*
35	$(H_2O)_5H^+ + N_2 \rightarrow (H_2O)_4H^+ + H_2O + N_2$	4×10^{-10} cm^3 s^{-1}	10
36	$H_3O^+ + e^- \rightarrow$ products	1.0×10^{-6} cm^3 s^{-1}	16
37	$(H_2O)_2H^+ + e^- \rightarrow$ products	2.2×10^{-6} cm^3 s^{-1}	16
38	$(H_2O)_3H^+ + e^- \rightarrow$ products	3.8×10^{-6} cm^3 s^{-1}	16
39	$(H_2O)_4H^+ + e^- \rightarrow$ products	4.9×10^{-6} cm^3 s^{-1}	16
40	$(H_2O)_5H^+ + e^- \rightarrow$ products	6.0×10^{-6} cm^3 s^{-1}	16

where the superscript m indicates time level and where L_{CD} represents the convection and diffusion terms in equation 4-3, spatially differenced on the rz grid. With $C_{ij} = 0$ it is well known that such a forward-time/centered-space scheme for equation 4-4 is absolutely unstable, but if the eigenvalues of the matrix C_{ij} are negative, then this implicit method can be shown to stable, which we find to be the case in practice. An appropriate time step Δt is chosen (microsecond sized, or smaller), and the simulation of the various species is begun with upstream values on the left edge of the simulation assumed to be given by solving $C_{ij}n_j = 0$ at this left edge. The species densities propagate across the grid from left to right, and when they are roughed in, the time step is reduced to obtain smooth and accurate values. The second-order spatial differencing used in this solution results in much less numerical diffusion than is obtained with upwind differencing or with the Scharfetter-Gummel scheme. The species tracked by equation 4-4 included He_m, He_2^+, He^+, N_2^+, N_4^+, H_2O^+, H_3O^+, $(H_2O)_2H^+$, $(H_2O)_3H^+$, $(H_2O)_4H^+$, and $(H_2O)_5H^+$. He_m densities were considered to be fixed in time and space in the active discharge region because they were measured experimentally at the steady state reached by the discharge. They were not allowed to diffuse, flow, or react until they entered the nozzle in the copper electrode.

We found that the reactions involving He_m did not satisfy the steady state condition we imposed on the simulation. This was due to the loss terms for He_m—including Penning ionization with water and nitrogen—being much larger than the source terms. This made it necessary to include with the reactions involving He_m an extra source term that encompassed contributions from electron impact reactions with ground state helium. A similar term was included for the generation of He^+ by electron impact. This source term was estimated from the experimental data in the active discharge region by assuming that the overall change in density

of He_m was 0 and adding an extra term to force this condition to be met. The source term was then extrapolated into the region of the nozzle using an exponential decay. Our experimental results showed no detectable He_m beyond the end of the copper electrode. The exponential decay was designed to match that observation by ensuring that the density of He_m was below the detection limit of the absorption spectrometer past the end of the copper electrode. For those simulations run with changing impurity and humidity levels, the He_m and He^+ source terms were kept constant, but the densities were allowed to change to estimate the changes that would occur with changing N_2 and H_2O densities.

4.4 Results and Discussion

4.4.1 Experimental Measurements of the Helium Metastable Atoms Densities

The measured number densities of He_m taken using atomic absorption spectroscopy are shown in figure 4-2. In the figure, the 0 distance point corresponds to the tip of the tungsten pin electrode. The data show a high density of He_m close to the end of the pin that drops off sharply. The number density of He_m then slightly increases before dropping off again gradually towards the copper plate electrode. The sharp initial decrease in the number density can be attributed to the loss of He_m via reaction with N_2 or H_2O impurities from the plasma gas or other trace sources. The subsequent increase in signal may be due to recombination of He_2^+ or He^+ with electrons to form He_m atoms. Measurements of the afterglow region downstream from the copper cap electrode showed that the densities of He_m were below the limit of detection of our absorption spectrometer. In general, these data show that the highest densities of He_m exist where the electric field is the highest.

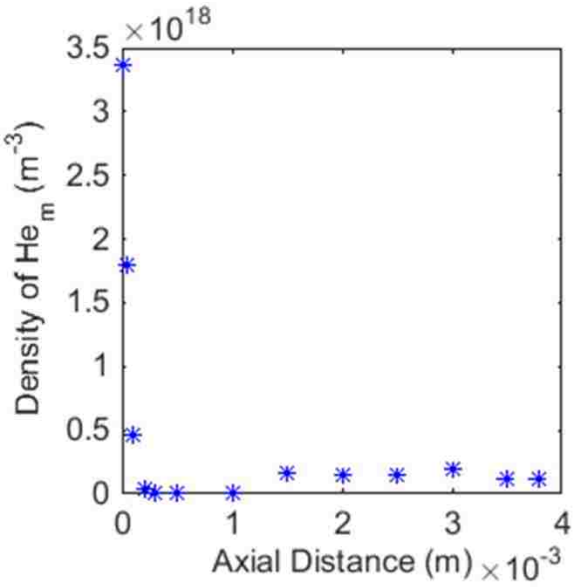

Figure 4-2 : Experimentally measured helium metastable atom densities in a DC glow discharge. The 0 point on the graph corresponds to the tip of the high voltage pin electrode. Error bars for these measurements are smaller than the data markers.

4.4.2 Simulation Results

Figure 4-3 shows the results of the flow dynamics model. Within a few millimeters of the exit of the discharge tube, air has diffused into the helium gas stream in significant amounts. The amount of air in the helium stream increases as the helium travels downstream. However, the fluid model does not show that any large amount of air diffuses back into the active discharge region of the discharge tube. At a helium flow rate of 2 L min^{-1}, convection is able to mostly overcome the effects of diffusion.

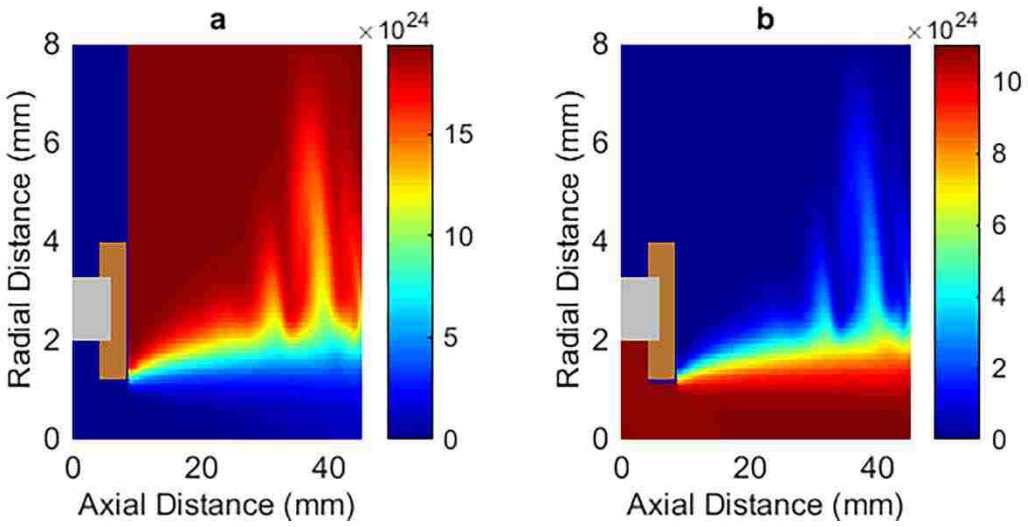

Figure 4-3 : Surface plot of the N_2 (a) and helium (b) densities in the simulated area. This shows how the N_2 diffuses into the helium stream. The aberrations in the gas flow in the last 10 mm are due to some turbulence in the gas flow. The grey and copper colored blocks show the locations of the glass and copper electrode respectively.

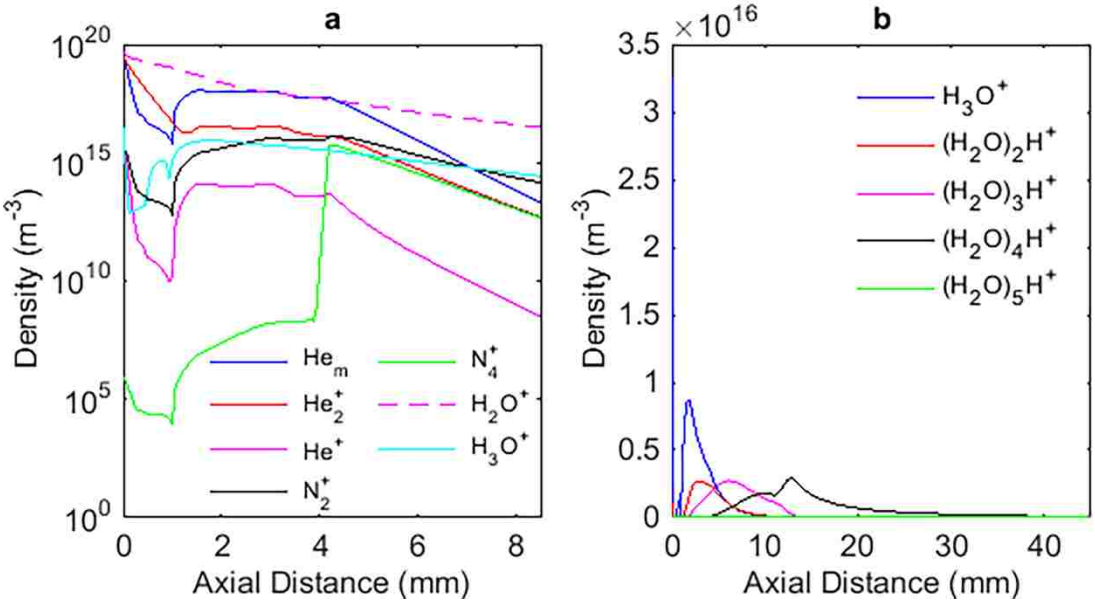

Figure 4-4 : Plots of the densities of each species tracked along the axis of the simulation. Plot **a** shows the densities of the protonated water cluster ion precursors on a semi log scale along the axis of the simulated area in the active discharge region. Plot **b** shows the densities of the protonated water cluster ions along the axis of the discharge for the full length of the simulated area.

The simulation is designed to calculate the density of each species tracked at every point in the simulation space. Figure 4-4 shows the evolution of the species along the axis of the

discharge. Figure 4-5 shows the results for each protonated water cluster ion over the full simulation area. The excited helium species quickly ionize the nitrogen and water that are present to form N_2^+ and H_2O^+ ions. The densities of all excited helium species decrease very rapidly after the pin electrode. None are found beyond 4 mm past the end of the copper plate electrode. Within 4 mm of the copper electrode, the density of He_m does not exceed the limit of detection (3×10^{15} m^{-3}) of the spectrometer at any point. The lack of He_m in the afterglow is due to the increase in N_2 and water densities, which rapidly quench any He_m through Penning ionization reactions. These data are consistent with our inability to detect any He_m atoms in the afterglow region of the discharge experimentally.

The N_2^+ ions react with N_2 to form N_4^+, which reacts readily with water to form more H_2O^+ ions. The H_2O^+ ions are then converted into H_3O^+, initiating the formation of protonated water cluster ions. The results show that the densities of H_3O^+ ions in the active discharge or the afterglow region are orders of magnitude lower than those of other species, suggesting that they are very rapidly converted into protonated water cluster ions. The higher order water clusters (n=4, 5) do not form until the gas flow enters the hole in the copper plate electrode and expands into the afterglow region. The delay in the formation of the larger water cluster ions indicates that the formation depends on the entrainment of air into the gas stream or on the diffusion of air into the active discharge region.

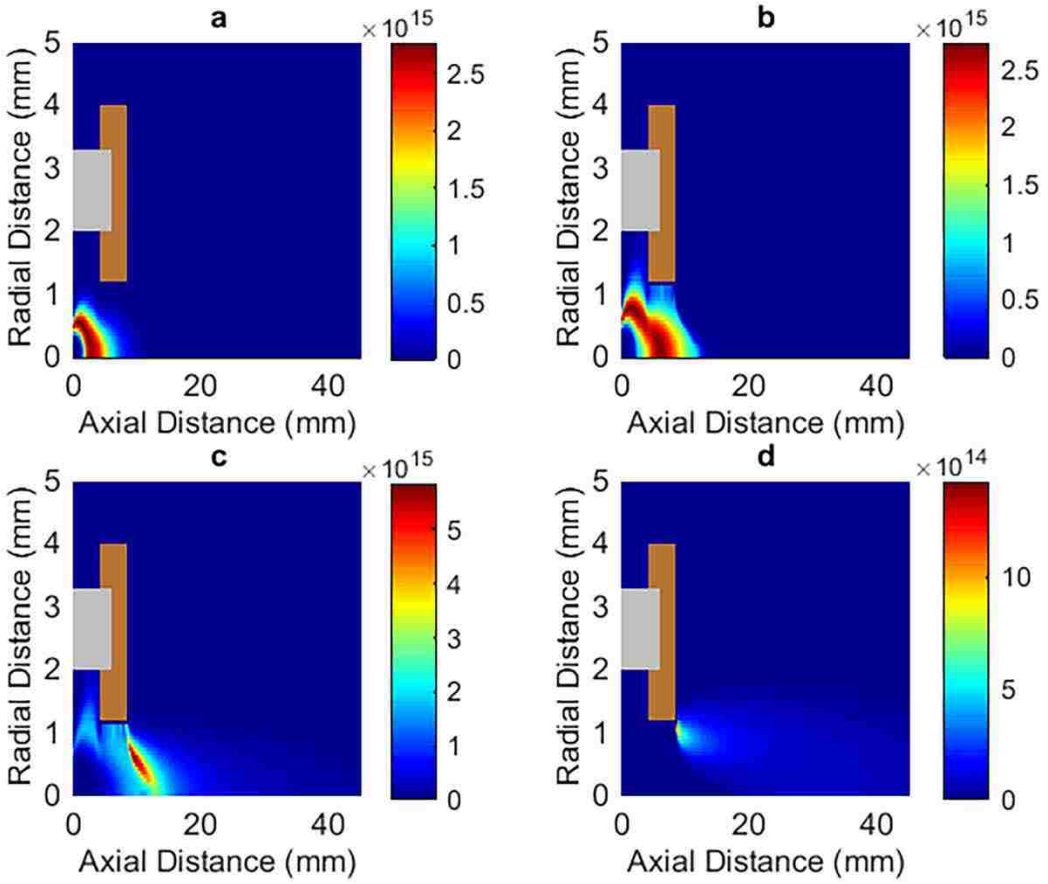

Figure 4-5 : Surface plots of the densities of $(H_2O)_2H^+$ (a), $(H_2O)_3H^+$ (b), $(H_2O)_4H^+$ (c), and $(H_2O)_5H^+$ (d). $(H_2O)_5H^+$ is the main ion in the afterglow region, but $(H_2O)_3H^+$ and $(H_2O)_4H^+$ were both present in significant amounts in the afterglow. The grey and copper colored blocks show the locations of the glass and copper electrode respectively.

The simulation provided insight into which reaction channels have the most important effect on the production of H_2O^+. There are five ways in which H_2O^+ can be made: charge transfer reactions of H_2O with He^+, He_2^+, N_2^+, or N_4^+ and Penning ionization with He_m. The data show that near the tungsten electrode, the main ways H_2O^+ is formed are through reactions with He_m and He_2^+. Downstream from the tungsten pin, He_m is still the most significant source of H_2O^+, but N_2^+ overtakes He_2^+ as the second most significant source of H_2O^+. He^+ and N_4^+ also contribute to the production of H_2O^+, but their contributions are orders of magnitude smaller than those of He_m, N_2^+, and He_2^+. These data emphasize the important role excited helium and

nitrogen species play in the performance of ADI-MS sources. They also suggest that one way to improve the ionization efficiency of the source would be to increase the number of excited helium species in the plasma.

4.4.3 The Role of Impurities in the Plasma Gas

The levels of impurities in ultra-high purity helium gas are up to 1 ppm of water and 5 ppm of N_2 as reported by Airgas. These values were used in the data shown above. To observe the effects of impurities on the chemistry of the discharge, the impurity levels were altered. In separate simulations, the N_2 and water concentrations were set to 0.01, 0.1, 1, 10, and 100 times their original values of 5 ppm for N_2 and 1 ppm for water in separate simulations.

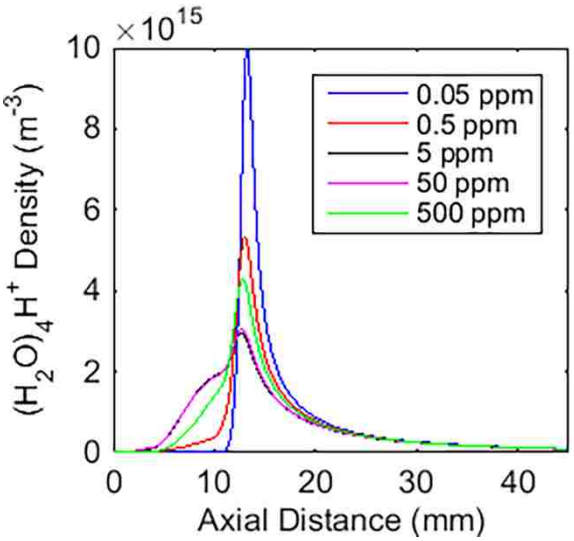

Figure 4-6 : Plot of the $(H_2O)_4H^+$ ion density along the axis of the discharge as the N_2 impurity level was varied. The $(H_2O)_4H^+$ density decreased with increasing N_2 concentration until approximately 50 ppm N_2 after which it increased.

The data for the N_2 impurity levels are presented in figure 4-6. The level of nitrogen impurity that yielded the highest density of $(H_2O)_4H^+$ was 0.05 ppm. As more nitrogen was added, the density fell, but then began to increase again with the addition of 50 ppm nitrogen.

However, even for the highest nitrogen impurity level, the total density for $(H_2O)_4H^+$ did not exceed that of the lowest impurity level. For low nitrogen densities in the active discharge region, the excited helium species are more likely to react with water. The resulting increase in reactions between helium and water leads to faster generation of a larger number of protonated water cluster ions. As the nitrogen density increases in the active discharge region, the likelihood of helium reacting with water decreases. Although the resulting nitrogen-containing species—N_2^+ and N_4^+—are able to react further to become protonated water cluster ions, there is also a significant chance that they will recombine with electrons and become nonreactive. As a result, the number of protonated water cluster ions at higher levels of nitrogen impurity is lower than at low impurity levels.

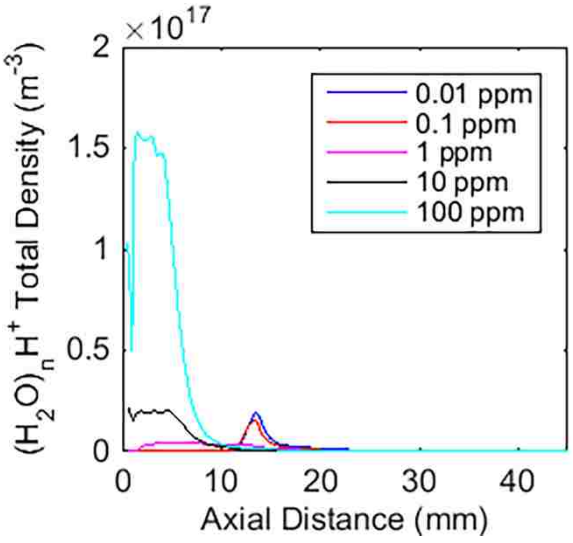

Figure 4-7 : Plot of the total protonated water cluster ion density for varying levels of water impurity in the plasma gas. The addition of water to the plasma gas causes an overall increase in the density of the protonated water cluster ions. The effect is observed the most in the active discharge region.

The results when varying the water impurity concentration are shown in figure 4-7. As more water is added to this type of discharge, it increases the probability of the reaction of water with an excited helium ion or atom. This factor increased the density for all protonated water

cluster ions in the simulated area, but especially increased the numbers observed in the active discharge region where the increased impurity levels met the excited helium species. The increase in the water impurity caused the cluster ions to increase in size faster. Under normal conditions (see figure 4-4), the $(H_2O)_3H^+$ ion was the most abundant cluster in the active discharge region. However, as the water impurity concentration increased, the $(H_2O)_4H^+$ ion became the most abundant. This emphasizes the previously-mentioned result that having more water in the active discharge region increases the probability of reaction between excited helium species and water and shows that the water impurity plays a critical role in the analytical performance of an ADI-MS source. As water was removed from the active discharge region, the densities of all water clusters were depleted by the lack of available water.

Allowing the He_m density in the active discharge region to change in the simulations that modeled impurity changes showed that for lower N_2 or water impurity concentrations, more He_m were present in the active discharge region and more He_m survive into the afterglow region. In the active discharge, the density of He_m increased by a factor of 2.2 and 1.2 when the N_2 and water impurity concentrations were reduced to their lowest levels. This is due to a lack of N_2 and water that normally would quench the He_m population. However, like in the initial simulation, the He_m density drops to zero within 1 mm of the end of the ground electrode.

Often it is assumed that extremely pure gases must be used for the plasma gases of ADI-MS sources. Although it is important to use plasma gas that is sufficiently pure to form a stable discharge, our results indicate it may in some cases be advantageous to use a plasma gas with slightly different levels of N_2 and water impurities than are normally present in ultra-high purity gases. In particular, it would be best to limit the amount of N_2 while increasing the amount of water. The limit of this effect would be the point where the energetic helium species are all

consumed by reactions with N_2 and water. Any further additions of impurities would simply change the characteristics of the plasma rather than increasing its ability to ionize a sample.

The effects of adding excess N_2 have been experimentally explored by Klute et al.[17] They found that for a dielectric barrier discharge (DBD), the addition of a few 100 ppm of extra N_2 caused the emission from the plasma to be dominated by excited N_2. An increase in OH emission would likely be observed when increasing the water impurity. The results suggest that an adjustment of the impurity concentrations in the ppm range may lead to enhanced ionization efficiency of ambient discharges without fundamentally changing the nature of the discharge.

4.4.4 The Effect of Changing Relative Humidity

Another important factor when performing ADI-MS is the relative humidity of the air surrounding the discharge. It is a parameter over which the analyst has little control, yet which greatly changes the amount of water available for the formation of reagent ions in the plasma discharge. The relative humidity for the results shown above was set at 30%. To observe the effects of changing humidity, simulations were carried out at relative humidity levels of 3%, 15%, 45%, 60%, 75%, and 90%. The results are shown in figure 4-8. The change in humidity was shown to have essentially no effect on ion formation in the active discharge region where the water from the air is only present to the extent that it diffuses in. As the helium gas is flowing against the diffusion of the water from the air, the amount of atmospheric water in the active discharge region is minimal. However, in the afterglow region, the effects are more pronounced. With increasing humidity, the overall number of protonated water clusters remained constant, but the ratio of $(H_2O)_5H^+/(H_2O)_4H^+$ increased. In addition to the changes in the type of water cluster ion formed, the amount of N_2^+ and N_4^+ present in the afterglow increased by approximately an

order of magnitude at 3 % humidity compared to 30 %. The presence of these ions in greater abundances in the afterglow may lead to a greater degree of fragmentation of analyte ions, as has been observed experimentally using the DART.[18, 19] One caveat to these results is that the simulation assumes that there is no water stuck to the walls of the discharge tube or the tubing through which the helium gas flows—conditions that would occur only when a discharge has been operating for an extended amount of time. In practice, it is difficult to eliminate all water from tubing and other sources in the discharge and gas tubing. If we were we able to model those conditions, different results may have been obtained, but in our simulation a significant effect was observed only in the afterglow region of the discharge.

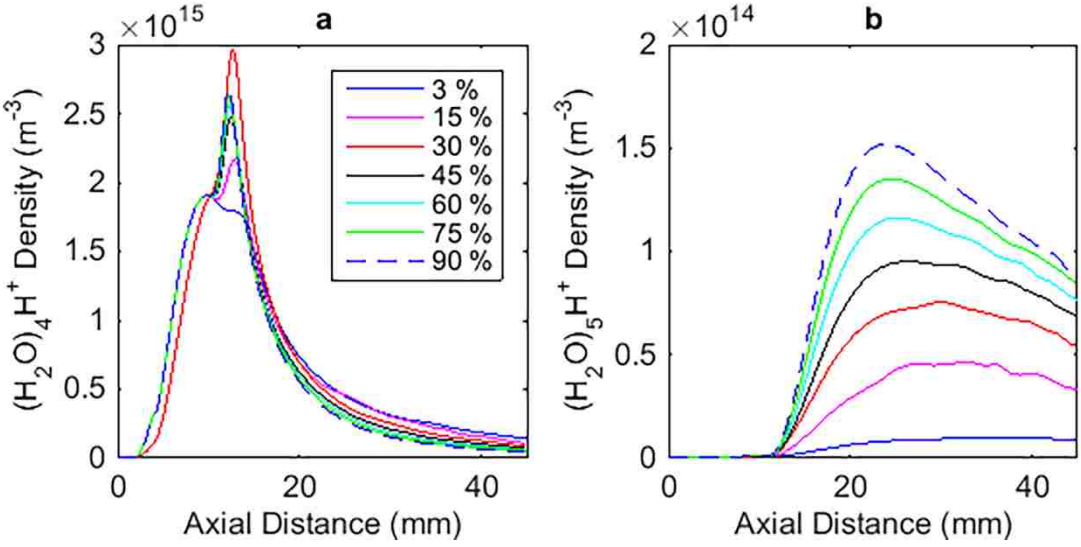

Figure 4-8 : Comparison of the densities of the $(H_2O)_4H^+$ (a) and $(H_2O)_5H^+$ (b) ions along the axis of the simulated area with varying relative humidity. With increasing humidity, the density of $(H_2O)_4H^+$ decreases while the $(H_2O)_5H^+$ density increases.

4.4.5 The Effect of Changing Air Pressure

Our laboratory is located at high elevation and a corresponding lower atmospheric pressure than at sea level. This simulation was carried out using the densities for air such as are found at sea level. To determine if a change in air pressure due to a change in elevation would affect the

chemistry of the discharge, a simulation was done assuming air densities that were approximately 85 % of those at sea level. No significant change was found between the two sets of results. Combining these results with those where the humidity was changed, it appears that environmental changes have minimal effect on the overall efficiency of the discharge in the case we modeled.

4.5 Conclusions

In this study, we have added to the understanding of how protonated water cluster ions form in a DC glow discharge used as an ADI-MS source. We have expanded the results seen by others to provide a greater understanding of the many factors that influence the performance of ADI-MS sources.

One of the unanswered questions to this point in the study of ADI-MS is how changes in the ambient conditions change the performance of the discharge in a quantitative way. Our results indicate that the formation of $(H_2O)_nH^+$ ions, and consequently the performance of the source, depends significantly more on the concentrations of the impurities found in the plasma gas than on the ambient conditions. Though changes in the ambient conditions do affect the performance of the source significantly, as has been observed experimentally,[18, 19] we calculate that changes to the impurity levels of the plasma gas would have a more significant impact. These results have some obvious limitations stemming from the assumptions made to make the simulation possible, but the data do have a strong basis in reality due to the use of experimental data as the foundation of the calculations. The dependence of the performance of the source on impurities over ambient conditions and atmospheric pressure suggests that these sources could be

used without any large disadvantages in many places around the world and in many different conditions.

The results indicating that the purity requirements for the plasma gas may not be as stringent as is assumed would allow for a significant reduction in operating costs for plasma ADI sources. This in turn might encourage their use in more commercial applications or simply make it more feasible for use with other techniques and applications.

4.6 References

1. Martens, T.; Mihailova, D.; van Dijk, J.; Bogaerts, A., *Anal. Chem.* **2009,** *81*, 9096-9108.
2. Reininger, C.; Woodfield, K.; Keelor, J. D.; Kaylor, A.; Fernández, F. M.; Farnsworth, P. B., *Spectrochim. Acta B* **2014,** *100*, 98-104.
3. Heywood, M. S.; Taylor, N.; Farnsworth, P. B., *Anal. Chem.* **2011,** *83*, 6493-6499.
4. Sakiyama, Y.; Graves, D. B.; Jarrige, J.; Laroussi, M., *Appl. Phys. Lett.* **2010,** *96*, 041501.
5. Teschke, M.; Kedzierski, J.; Finantu-Dinu, E. G.; Korzec, D.; Engemann, J., *IEEE Trans. Plasma Sci.* **2005,** *33*, 310-311.
6. Fuller, E. N.; Schettler, P. D.; Giddings, J. C., *Ind. Eng. Chem.* **1966,** *58*, 18-27.
7. Albritton, D. L., *At. Data Nucl. Data Tables* **1978,** *22*, 1-89.
8. Bierbaum, V. M.; Golde, M. F.; Kaufman, F., *J. Chem. Phys.* **1976,** *65*, 2715-2724.
9. Bolden, R. C.; Twiddy, N. D., *Faraday Discuss. Chem. Soc.* **1972,** *53*, 192-200.
10. Good, A.; Durden, D. A.; Kebarle, P., *J. Chem. Phys.* **1970,** *52*, 212-221.
11. Keister, K. E.; Wagner, C. J.; Putney, J. L.; Hewitt, J. D.; Eden, J. G., *Phys. Rev. A* **2014,** *89*, 013401.
12. Mul, P. M.; McGowan, J. W., *J. Phys. B: At. Mol. Phys.* **1979,** *12*, 1591.
13. Ohno, K.; Takami, T.; Mitsuke, K.; Ishida, T., *J. Chem. Phys.* **1991,** *94*, 2675-2687.
14. Ostrander, S. C.; Weisshaar, J. C., *Chem. Phys. Lett.* **1986,** *129*, 220-224.
15. Smith, D.; Adams, N. G.; Miller, T. M., *J. Chem. Phys.* **1978,** *69*, 308-318.
16. Leu, M. T.; Manfred, A.; Johnsen, R., *Phys. Rev. A* **1973,** *7*, 292-298.
17. Klute, F. D.; Schutz, A.; Michels, A.; Vadla, C.; Veza, D.; Horvatic, V.; Franzke, J., *Analyst* **2016,** *141*, 5842-5848.
18. Newsome, G. A.; Ackerman, L. K.; Johnson, K. J., *Anal. Chem.* **2014,** *86*, 11977-11980.
19. Newsome, G. A.; Ackerman, L. K.; Johnson, K. J., *J. Am. Soc. Mass. Spectrom.* **2015,** *27*, 135-143.

5 FUTURE WORK

5.1 Future Directions for the Work Described

The results described above regarding the use of mixed plasma gases for ambient desorption/ionization sources leads to several more questions regarding the use of other gas dopants and their potential for enhancing or changing analyses done using ADI-MS. Potential gas mixtures could include O_2, NH_3, and others in helium or argon as well as H_2 in gases such as N_2 or air. Some work in this direction has been undertaken by the group of Jacob Shelley at Rensselaer Polytechnic Institute. Specifically, they are using O_2-doped helium with the FAPA.[1] One of the interesting results they obtained was the conversion of benzene into pyrylium ions. Other interesting results are likely to come in the future.

One of the main questions that has yet to be answered is the mechanism by which H_2 addition enhances the ionization efficiency of the DBD. A number of experiments could be undertaken to expand the understanding of the subject including the use of spectroscopy to determine how a H_2-doped plasma differs from a pure gas one based on emission or florescence. It may also be possible to extend the simulation work I have done to model a H_2-doped discharge. The main difficulty to doing this is likely finding reliable kinetic data for the many reactions that could be happening in the H_2-doped discharges. However, were such data found, a computational model may offer significant insight into the changes in chemistry.

5.2 The Future of Ambient Desorption/Ionization Mass Spectrometry

The future of ADI-MS as a technique is bright. There is still a large amount of active research in the field. Much of the research is extending into the field of biochemistry and biology. It is likely that the breadth of the capabilities and the number of applications for ADI-MS will continue to grow for a number of years. It may find long term use in fields such as mass spectral imaging, law enforcement, medicine, and others.

One of the main drawbacks to the use of any ambient ionization technique is the fact that controlling the ambient conditions surrounding the analysis is not a trivial matter. Changes in air temperature, humidity, and other factors can make getting reproducible results from an ADI-MS analysis difficult. These factors limit the degree to which the techniques are able to be quantitative. However, the ability to perform analyses under ambient conditions is what will continue to make the use of ADI-MS advantageous given the lack of required sample prep and the ability to analyze samples rapidly in their native state.

5.3 References

1. Badal, S. P.; Ratcliff, T. D.; You, Y.; Breneman, C. M.; Shelley, J. T., *J. Am. Soc. Mass. Spectrom.* **2017,** *28*, 1013-1020.

6 APPENDIX: DC DISCHARGE SIMULATION MATLAB CODE

6.1 DC Discharge Simulation Matlab Code

6.1.1 Main Script

```
clear; close all
for w=1:15 %Beginning of impurity loop
%Simulation of the flow and chemistry in a DC glow discharge based in He.
% i is r, j is z.
%Read in non uniform grid data and assign it to variable.
A=dlmread('2R2Z.csv',',',1,0);
mfract1=A(:,1);
temp1=A(:,2);
velx=A(:,3);
vely=A(:,4);
x=A(:,5);
y=A(:,6);
%Define uniform grid.
dz=1.25e-4/2;
dr=1.25e-4/2;
xnew=0:dz:max(x);
Nz=length(xnew);
ynew=-0.5*dr:dr:max(y);
Nr=length(ynew)+1;
[Z,R]=meshgrid(xnew,ynew);
mfract=zeros(Nr,Nz);
vz=zeros(Nr,Nz);
vr=zeros(Nr,Nz);
temp=zeros(Nr,Nz);
%Turn x and y into indices for loading data into a grid.
x1=x./dz+1;
y1=y./dr+1.5;
x1=round(x1);
y1=round(y1);

for n=1:length(x)
   mfract((y1(n)),(x1(n)))=mfract1(n);
   vz((y1(n)),(x1(n)))=velx(n);
```

```
   vr((y1(n)),(x1(n)))=vely(n);
   temp((y1(n)),(x1(n)))=temp1(n);
end

%Make the velocity on the air/metal and air/glass boundaries pull into the
%wall instead of pulling out of it.
for n=1:67
   if vr(35,n)>0
      vr(35,n)=-vr(35,n);
   end
end
for n=38:140
   if vr(19,n)>0
      vr(19,n)=-vr(19,n);
   end
end

%Set ghost points equal to row above them.
mfract(1,:)=mfract(2,:);
temp(1,:)=temp(2,:);
vr(1,:)=-vr(2,:);
vz(1,:)=vz(2,:);

%Smooth the velocity, mole fraction, and temperature data
step=5;
wgt=2;
vz=smoother(vz,2,dr,step,wgt);
vr=smoother(vr,1,dr,step,wgt);
mfract=smoother(mfract,2,dr,step,wgt);
temp=smoother(temp,2,dr,step,wgt);

%Remove points at electrodes
vz(36:Nr,1:140)=0; vz(20:Nr,68:140)=0;
vr(36:Nr,1:140)=0; vr(20:Nr,68:140)=0;
mfract(36:Nr,1:140)=0; mfract(20:Nr,68:140)=0;
temp(36:Nr,1:140)=0; temp(20:Nr,68:140)=0;

%Make the maximum value for the mole fraction 1
for j=1:Nz;
   for i=1:Nr;
      if mfract(i,j)>1
         mfract(i,j)=1;
      end
   end
end

%Calculate diffusion coefficients using Fuller-Schettler-Giddings Eq.
vaH2O=12.7; vaN2=17.9; vaAir=20.1; vaHe=2.88; vaN4= 78; vaH2O2=20.86;
vaH2O3=30.3; vaH2O4=39.74; vaH2O5=49.18; vaH3O=11.42;
mH2O=18.02; mN2=28.02; mAir=28.74; mHe=4.04; mN4= 56.04; mH2O2=37.03;
mH2O3=55.04; mH2O4=73.05; mH2O5=91.06; mH3O=19.03;
```

```
DHeAir=DiffusionTemp(temp,mHe,mAir,vaHe,vaAir)./10000;
DN2Air=DiffusionTemp(temp,mN2,mAir,vaN2,vaAir)./10000;
DH2OAir=DiffusionTemp(temp,mH2O,mAir,vaH2O,vaAir)./10000;
DN4ionAir=DiffusionTemp(temp,mN4,mAir,vaN4,vaAir)./10000;
DH2O2Air=DiffusionTemp(temp,mH2O2,mAir,vaH2O2,vaAir)./10000;
DH2O3Air=DiffusionTemp(temp,mH2O3,mAir,vaH2O3,vaAir)./10000;
DH2O4Air=DiffusionTemp(temp,mH2O4,mAir,vaH2O4,vaAir)./10000;
DH2O5Air=DiffusionTemp(temp,mH2O5,mAir,vaH2O5,vaAir)./10000;
DH3OAir=DiffusionTemp(temp,mH3O,mAir,vaH3O,vaAir)./10000;
DHe2Air=DiffusionTemp(temp,mAir,2*mHe,vaAir,2*vaHe)./10000;

DH2OHe=DiffusionTemp(temp,mH2O,mHe,vaH2O,vaHe)./10000;
DN2He=DiffusionTemp(temp,mN2,mHe,vaN2,vaHe)./10000;
DN4ionHe=DiffusionTemp(temp,mN4,mHe,vaN4,vaHe)./10000;
DH2O2He=DiffusionTemp(temp,mH2O2,mHe,vaH2O2,vaHe)./10000;
DH2O3He=DiffusionTemp(temp,mH2O3,mHe,vaH2O3,vaHe)./10000;
DH2O4He=DiffusionTemp(temp,mH2O4,mHe,vaH2O4,vaHe)./10000;
DH2O5He=DiffusionTemp(temp,mH2O5,mHe,vaH2O5,vaHe)./10000;
DH3OHe=DiffusionTemp(temp,mH3O,mHe,vaH3O,vaHe)./10000;
DHe2He=DiffusionTemp(temp,mAir,2*mHe,vaHe,2*vaHe)./10000;
DHeHe=DiffusionTemp(temp,mHe,mHe,vaHe,vaHe)./10000;


% define a mask grid that is 1 where diffusion should be calculated
% but which is 0 where it shouldn't

mask=ones(Nr,Nz);
mask(35:Nr,1:140)=0;
mask(19:Nr,67:141)=0;
mask(66:Nr,141)=1;
mask(19,141)=1;
mask(19,67)=1;

north=zeros(Nr,Nz);
north(19,68:140)=1;
north(35,1:67)=1;
west=zeros(Nr,Nz);
west(20:65,141)=1;
east=zeros(Nr,Nz);
east(20:35,67)=1;

DHeAir=DHeAir.*mask;
DN2Air=DN2Air.*mask;
DH2OAir=DH2OAir.*mask;
DH2OHe=DH2OHe.*mask;
DN2He=DN2He.*mask;
DN4ionAir=DN4ionAir.*mask;
DH2O2Air=DH2O2Air.*mask;
DH2O3Air=DH2O3Air.*mask;
DH2O4Air=DH2O4Air.*mask;
```

```
DH2O5Air=DH2O5Air.*mask;
DH3OAir=DH3OAir.*mask;
DHe2Air=DHe2Air.*mask;
DN4ionHe=DN4ionHe.*mask;
DH2O2He=DH2O2He.*mask;
DH2O3He=DH2O3He.*mask;
DH2O4He=DH2O4He.*mask;
DH2O5He=DH2O5He.*mask;
DH3OHe=DH3OHe.*mask;
DHe2He=DHe2He.*mask;
DHeHe=DHeHe.*mask;

%Define starting densities for unknown species. Convert to m^-3.
N2ion=ones(Nr,Nz);
N4ion=ones(Nr,Nz);
H2Oion=ones(Nr,Nz);
H2O2=ones(Nr,Nz);
H2O3=ones(Nr,Nz);
H2O4=ones(Nr,Nz);
H2O5=ones(Nr,Nz);
H3O=ones(Nr,Nz);
Heion=ones(Nr,Nz);
He2ion=ones(Nr,Nz);

%Read in Hem data from spreadsheet.
B=dlmread('DBD13_LTP7_AC11_DC13_Hem.csv',',',2,0);
Hem=B(:,8);
Hemx=B(:,7)./1000;
Hemx(1)=0.00003;
%Linear interpolation of Hem
dHemx=0.125e-3/2;
Hemxnew=0:dHemx:0.004;
Hemxnew(1,1)=0.00003;
Hemlin=interp1(Hemx,Hem,Hemxnew);%,'spline');
Hemlin(62:67)=Hemlin(61);
Hemlin=Hemlin.*1e6;
%Hemlin(1)=3.36e12*1e6; Hemlin(end)=1.24e11*1e6;
%Assume plasma occupies a cone of space in the discharge, and the
%Hem are distributed according to a Gaussian distribution.  Create Hem matrix.
Hemnew=ones(Nr,Nz);

x2=-0.5*dr:0.125e-3/2:0.00209375;
x2=fliplr(x2);

%c (the std dev) can be adjusted to change the change in width of the distribution as
%it goes on through space

c=0.001/6;

   for n=1:numel(Hemlin);
      b(n)=1/(2*c^2);
```

```
        a(n)=Hemlin(n)*0.004*sqrt(b(n))/sqrt(pi);
        y2(n,:)=a(n).*exp(-b(n).*x2.^2);
        c=c+1/6/67/1000;
    end


y2=rot90(y2);
Hemnew(1:35,1:67)=y2;%(1:7,1:33);

%Set up the iterations for differing impurity and humidity levels
aa=[0.85,1,1,1,1,1,1,1,1,1,1,1,1,1,1];
bb=[1,0.01,0.1,10,100,1,1,1,1,1,1,1,1,1,1];
cc=[1,1,1,1,1,0.01,0.1,10,100,1,1,1,1,1,1];
dd=[1,1,1,1,1,1,1,1,1,0.1,0.5,1.5,2,2.5,3];

%Calculate densities of N2 H2O and He on grid including impurities
ntot=1.013e5./(1.38e-23.*temp)*aa(w);
N2imp=ntot.*(mfract).*5e-6;%(5 ppm)
H2Oimp=ntot.*(mfract).*1e-6;%(1 ppm)
Heair=ntot.*(1-mfract).*0.00000524;

N2=ntot.*(1-mfract).*0.78+N2imp*bb(w);
H2O=ntot.*(1-mfract).*0.01*dd(w)+H2Oimp*cc(w);
He=ntot.*mfract+Heair;

%Remove points at electrodes
N2(36:Nr,1:140)=0; N2(20:Nr,68:140)=0;
H2O(36:Nr,1:140)=0; H2O(20:Nr,68:140)=0;
N2ion(36:Nr,1:140)=0; N2ion(20:Nr,68:140)=0;
N4ion(36:Nr,1:140)=0;  N4ion(20:Nr,68:140)=0;
e(36:Nr,1:140)=0;  e(20:Nr,68:140)=0;
H2Oion(36:Nr,1:140)=0;  H2Oion(20:Nr,68:140)=0;
H2O2(36:Nr,1:140)=0;  H2O2(20:Nr,68:140)=0;
H2O3(36:Nr,1:140)=0;  H2O3(20:Nr,68:140)=0;
H2O4(36:Nr,1:140)=0;  H2O4(20:Nr,68:140)=0;
H2O5(36:Nr,1:140)=0;  H2O5(20:Nr,68:140)=0;
H3O(36:Nr,1:140)=0;  H3O(20:Nr,68:140)=0;
Hemnew(36:Nr,1:140)=0;  Hemnew(20:Nr,68:140)=0;
Heion(36:Nr,1:140)=0;  Heion(20:Nr,68:140)=0;
He2ion(36:Nr,1:140)=0;  He2ion(20:Nr,68:140)=0;
He(36:Nr,1:140)=0;  He(20:Nr,68:140)=0;

%Calculate density weighted diffusion constants
DHe=(He.*DHeHe+N2.*DHeAir)./(He+N2);
DHe2=(He.*DHe2He+N2.*DHe2Air)./(He+N2);
DN2=(He.*DN2He+N2.*DN2Air)./(He+N2);
DN4=(He.*DN4ionHe+N2.*DN4ionAir)./(He+N2);
DH2O=(He.*DH2OHe+N2.*DH2OAir)./(He+N2);
DH3O=(He.*DH3OHe+N2.*DH3OAir)./(He+N2);
DH2O2=(He.*DH2O2He+N2.*DH2O2Air)./(He+N2);
DH2O3=(He.*DH2O3He+N2.*DH2O3Air)./(He+N2);
```

```
DH2O4=(He.*DH2O4He+N2.*DH2O4Air)./(He+N2);
DH2O5=(He.*DH2O5He+N2.*DH2O5Air)./(He+N2);
%Remove points in the electrode space
DHe(36:Nr,1:140)=0; DHe(20:Nr,68:140)=0;
DHe2(36:Nr,1:140)=0; DHe2(20:Nr,68:140)=0;
DN2(36:Nr,1:140)=0; DN2(20:Nr,68:140)=0;
DN4(36:Nr,1:140)=0; DN4(20:Nr,68:140)=0;
DH2O(36:Nr,1:140)=0; DH2O(20:Nr,68:140)=0;
DH3O(36:Nr,1:140)=0; DH3O(20:Nr,68:140)=0;
DH2O2(36:Nr,1:140)=0; DH2O2(20:Nr,68:140)=0;
DH2O3(36:Nr,1:140)=0; DH2O3(20:Nr,68:140)=0;
DH2O4(36:Nr,1:140)=0; DH2O4(20:Nr,68:140)=0;
DH2O5(36:Nr,1:140)=0; DH2O5(20:Nr,68:140)=0;
%Preallocate space for LCD variables to speed things up
LCDHeion=zeros(Nr,Nz);
LCDHe2ion=zeros(Nr,Nz);
LCDHem=zeros(Nr,Nz);
LCDN2ion=zeros(Nr,Nz);
LCDN4ion=zeros(Nr,Nz);
LCDH2Oion=zeros(Nr,Nz);
LCDH3O=zeros(Nr,Nz);
LCDH2O2=zeros(Nr,Nz);
LCDH2O3=zeros(Nr,Nz);
LCDH2O4=zeros(Nr,Nz);
LCDH2O5=zeros(Nr,Nz);

   for zz=1:10
      % let the electron density evolve
      e = (Heion+He2ion+N2ion+N4ion+H2Oion+H3O+H2O2+H2O3+H2O4+H2O5);

      %Calculate the desities at the left edge of the simulation area

      [Heion(1:28,1),He2ion(1:28,1),N2ion(1:28,1),N4ion(1:28,1)...
            ,H2Oion(1:28,1),H3O(1:28,1),H2O2(1:28,1),H2O3(1:28,1)...
            ,H2O4(1:28,1),H2O5(1:28,1)]=leftedge(N2,N2ion,N4ion,H2O,...
            H2Oion,H2O2,H2O3,H2O4,H2O5,H3O,Heion,He2ion,Hemnew,He,e);

   end

   %Calculate source terms for Hem and Heion
   [S0Hem, S0Heion]=S0res(Hemnew,Heion,He2ion,e,N2,H2O);

%Set dt, counting variable, and error.
dt=1.25e-6;
m=0;
error=1;
%Begin iteration loop
   while error>3e-4
      tic;
      m=m+1;
```

```
% let the electron density evolve
e = (Heion+He2ion+N2ion+N4ion+H2Oion+H3O+H2O2+H2O3+H2O4+H2O5);
%Determine the amount of convection and diffusion for each species
%N2ion
[LCDN2ion]=CDoperator(2,Nr-1,1,Nz-1,dr,dz,vr,vz,DN2,N2ion,mask,north,east,west);
 %N4ion
 [LCDN4ion]=CDoperator(2,Nr-1,1,Nz-1,dr,dz,vr,vz,DN4,N4ion,mask,north,east,west);
 %H2Oion
 [LCDH2Oion]=CDoperator(2,Nr-1,1,Nz-1,dr,dz,vr,vz,DH2O,H2Oion,mask,north,east,west);
 %H3O
 [LCDH3O]=CDoperator(2,Nr-1,1,Nz-1,dr,dz,vr,vz,DH3O,H3O,mask,north,east,west);
 %H2O2
 [LCDH2O2]=CDoperator(2,Nr-1,1,Nz-1,dr,dz,vr,vz,DH2O2,H2O2,mask,north,east,west);
 %H2O3
 [LCDH2O3]=CDoperator(2,Nr-1,1,Nz-1,dr,dz,vr,vz,DH2O3,H2O3,mask,north,east,west);
 %H2O4
 [LCDH2O4]=CDoperator(2,Nr-1,1,Nz-1,dr,dz,vr,vz,DH2O4,H2O4,mask,north,east,west);
 %H2O5
 [LCDH2O5]=CDoperator(2,Nr-1,1,Nz-1,dr,dz,vr,vz,DH2O5,H2O5,mask,north,east,west);
 %Heion
 [LCDHeion]=CDoperator(2,Nr-1,1,Nz-1,dr,dz,vr,vz,DHe,Heion,mask,north,east,west);
 %He2ion
 [LCDHe2ion]=CDoperator(2,Nr-1,1,Nz-1,dr,dz,vr,vz,DHe2,He2ion,mask,north,east,west);
 %Only convect and diffuse Hem starting in the nozzle.
 %Hem
 [LCDHemnew]=CDoperator(2,Nr-1,34,Nz-1,dr,dz,vr,vz,DHe,Hemnew,mask,north,east,west);



%Remove points at electrodes
N2(36:Nr,1:140)=0; N2(20:Nr,68:140)=0;
H2O(36:Nr,1:140)=0; H2O(20:Nr,68:140)=0;
N2ion(36:Nr,1:140)=0; N2ion(20:Nr,68:140)=0;
N4ion(36:Nr,1:140)=0;  N4ion(20:Nr,68:140)=0;
e(36:Nr,1:140)=0;  e(20:Nr,68:140)=0;
H2Oion(36:Nr,1:140)=0;  H2Oion(20:Nr,68:140)=0;
H2O2(36:Nr,1:140)=0;  H2O2(20:Nr,68:140)=0;
H2O3(36:Nr,1:140)=0;  H2O3(20:Nr,68:140)=0;
H2O4(36:Nr,1:140)=0;  H2O4(20:Nr,68:140)=0;
H2O5(36:Nr,1:140)=0;  H2O5(20:Nr,68:140)=0;
H3O(36:Nr,1:140)=0;  H3O(20:Nr,68:140)=0;
Hemnew(36:Nr,1:140)=0;  Hemnew(20:Nr,68:140)=0;
Heion(36:Nr,1:140)=0;  Heion(20:Nr,68:140)=0;
He2ion(36:Nr,1:140)=0;  He2ion(20:Nr,68:140)=0;
He(36:Nr,1:140)=0;  He(20:Nr,68:140)=0;

%Solve Chemistry Implicitly.

olderror=error;
```

```
        [Heion,He2ion,Hemnew,N2ion,N4ion,H2Oion,H3O,H2O2,H2O3,H2O4,H2O5,error]=...
         implicitsolverS0(dt,N2,N2ion,N4ion,H2O,H2Oion,H2O2,H2O3,H2O4,...

H2O5,H3O,Heion,He2ion,Hemnew,He,LCDHeion,LCDHe2ion,LCDHem,LCDN2ion,LCDN4ion,LCDH
2Oion,LCDH3O,...
            LCDH2O2,LCDH2O3,LCDH2O4,LCDH2O5,e,S0Hem,S0Heion);
    aa(m)=error;

    %Set new ghost points equal to row above them
    N2(1,:)=N2(2,:);
    H2O(1,:)=H2O(2,:);
    N2ion(1,:)=N2ion(2,:);
    N4ion(1,:)=N4ion(2,:);
    e(1,:)=e(2,:);
    H2Oion(1,:)=H2Oion(2,:);
    H2O2(1,:)=H2O2(2,:);
    H2O3(1,:)=H2O3(2,:);
    H2O4(1,:)=H2O4(2,:);
    H2O5(1,:)=H2O5(2,:);
    H3O(1,:)=H3O(2,:);
    Hemnew(1,:)=Hemnew(2,:);
    Heion(1,:)=Heion(2,:);
    He2ion(1,:)=He2ion(2,:);
    He(1,:)=He(2,:);

    %Linear extrapolation to the right edge
    N2ion(:,Nz)=2*N2ion(:,Nz-1)-N2ion(:,Nz-2);
    N4ion(:,Nz)=2*N4ion(:,Nz-1)-N4ion(:,Nz-2);
    H2Oion(:,Nz)=2*H2Oion(:,Nz-1)-H2Oion(:,Nz-2);
    e(:,Nz)=2*e(:,Nz-1)-e(:,Nz-2);
    H2O2(:,Nz)=2*H2O2(:,Nz-1)-H2O2(:,Nz-2);
    H2O3(:,Nz)=2*H2O3(:,Nz-1)-H2O3(:,Nz-2);
    H2O4(:,Nz)=2*H2O4(:,Nz-1)-H2O4(:,Nz-2);
    H2O5(:,Nz)=2*H2O5(:,Nz-1)-H2O5(:,Nz-2);
    H3O(:,Nz)=2*H3O(:,Nz-1)-H3O(:,Nz-2);
    Hemnew(:,Nz)=2*Hemnew(:,Nz-1)-Hemnew(:,Nz-2);
    Hemnew=round(Hemnew);
    Heion(:,Nz)=2*Heion(:,Nz-1)-Heion(:,Nz-2);
    He2ion(:,Nz)=2*He2ion(:,Nz-1)-He2ion(:,Nz-2);

    %Slow down the time step to allow things to converge
    if m>850*2
       dt=0.25e-6;
    end

    z=toc;
     %Display a graph every so often to watch the simulation converge
     if mod(m,10)==1
       fprintf('Iteration %g Time Step: %g Error: %g  Convergence rate: %g \n',w, m,error,error/olderror)
       surf(log(1+abs(H2O4)),'EdgeColor','none')
        pause(.01)
```

```
        save('data');
      end

  end %End of iteration loop
%Save the data
filename=strcat('SourceTest',int2str(w));
save(filename)
display('Finished')
clear; close all

end %End of impurity loop
```

6.1.2 Functions

6.1.2.1 Smoother

This function smooths out the data from Star-CCM+ to make it possible to differentiate the data further on in the code.

```
function fnew=smoother(f,parity,dr,step,i37)

% 2-d smoother
% f is the 2-d data array to be smoothed, f(i,j)=f(r,z)
% parity: 0 for no origin parity, 1 for odd, 2 for even
%         patch the origin after doing the general fitting
% dr: radial step size, cell centered grid
% step: integer step size from (i,j) to make the smoothing rectangle
% i37: Over the rectangle, centered at (i,j) weight the contributions
%      of the neighbors according to exp(-(i^2+j^2)/i37^2);

% run over the data and smooth it, avoiding zero values
% using zero values

[imax,jmax]=size(f); % find the size of the data array

% run over the data poins

for i=1:imax % top of the radial index loop
  for j=1:jmax % top of the axial index loop

    % define the rectangle in the data set, avoiding stepping outside
    % of the set
    iimin=max(i-step,1);
    iimax=min(i+step,imax);
    jjmin=max(j-step,1);
    jjmax=min(j+step,jmax);
```

```
        % pull the data into ftmp, a local rectangle starting at (1,1)
        ftmp=f(iimin:iimax,jjmin:jjmax);

        % run over ftmp and locate zero values
        msk=ftmp==0;

        msk=1-msk; % msk is 1 where there is data, 0 where the data are 0

        [ii,jj]=size(ftmp); % get the size of ftmp
        ic=.5*(1+ii);jc=.5*(1+jj); % get the center of ftmp i and j

        [I,J]=ndgrid(1:ii,1:jj); % 2-D i and j for building the weight

        I=I-ic;J=J-jc; % relative to the center of ftmp
        wgt=exp(-(I.^2+J.^2)/i37^2); % build the weight

        den = sum(sum(msk.*wgt)); % find the weighted averaging denominator
        if den>0 % only average if there is data to use
           fnew(i,j)=sum(sum(msk.*wgt.*ftmp))/den; % weighted average
        end

        %fprintf(' i %g j %g chk %g \n',i,j,sum(sum(msk)))


    end
end

% now handle parity in r about the origin

if parity==1  % odd about r=0

    % we will reload i=2:4 and j=j-step:j+step
    for j=1:jmax

        iimin=2;iimax=4;
        jjmin=max(j-step,1);
        jjmax=min(j+step,jmax);

        ftmp=f(iimin:iimax,jjmin:jjmax); % pull out the data

        % run over ftmp and locate zero values
        msk=ftmp==0;

        msk=1-msk; % 1 where there is data, 0 where there is not

        [ii,jj]=size(ftmp); % get the size of ftmp
        jc = (1+jj)*.5; % center of ftmp in j

        [I,J]=ndgrid(1:ii,1:jj); % 2-D i and j for building the weight
        J=J-jc; % relative to the center of ftmp
```

```
        wgt=exp(-(J.^2)/i37^2); % build the weight in j only

    % build a 2-d array of r-values for building the radial fitting
    % coefficients
    r=(I-.5)*dr;


    % redefine msk to include the weight
    msk=msk.*wgt;
    % least-squares fitting coefficients
    S2=sum(sum(msk.*r.^2));
    S4=sum(sum(msk.*r.^4));
    S6=sum(sum(msk.*r.^4));
    Sfr=sum(sum(msk.*ftmp.*r));
    Sfr3=sum(sum(msk.*ftmp.*r.^3));

    % odd parity, f=ar+br^3;
    a=(Sfr*S6-Sfr3*S4)/(S2*S6-S4^2);
    b=(Sfr3*S2-Sfr*S4)/(S2*S6-S4^2);

    % now load the smoothed data at points iimin:iimax at this j
    % with the fitting function, f = a + br^2
    fnew(iimin:iimax,j)=a*r(1:iimax-1,1)+b*r(1:iimax-1,1).^3;


    end

    % ghost points tacked onr

    fnew(1,:)=-fnew(2,:);

end % end of even parity if block

if parity==2  % even about r=0

    % we will reload i=2:4 and j=j-step:j+step
    for j=1:jmax

        iimin=2;iimax=4;
        jjmin=max(j-step,1);
        jjmax=min(j+step,jmax);

        ftmp=f(iimin:iimax,jjmin:jjmax); % pull out the data

        % run over ftmp and locate zero values
        msk=ftmp==0;

        msk=1-msk; % 1 where there is data, 0 where there is not

        [ii,jj]=size(ftmp); % get the size of ftmp
        jc = (1+jj)*.5; % center of ftmp in j
```

```
        [I,J]=ndgrid(1:ii,1:jj); % 2-D i and j for building the weight
        J=J-jc; % relative to the center of ftmp
        wgt=exp(-(J.^2)/i37^2); % build the weight in j only

    % build a 2-d array of r-values for building the radial fitting
    % coefficients
    r=(I-.5)*dr;


    % redefine msk to include the weight
    msk=msk.*wgt;
    % least-squares fitting coefficients
    S0=sum(sum(msk));
    S2=sum(sum(msk.*r.^2));
    S4=sum(sum(msk.*r.^4));
    Sf=sum(sum(msk.*ftmp));
    Sfr2=sum(sum(msk.*ftmp.*r.^2));

    % even parity, f=a+br^2;
    a=(Sf*S4-Sfr2*S2)/(S0*S4-S2^2);
    b=(Sfr2*S0-Sf*S2)/(S0*S4-S2^2);

    % now load the smoothed data at points iimin:iimax at this j
    % with the fitting function, f = a + br^2
    fnew(iimin:iimax,j)=a+b*r(1:iimax-1,1).^2;


    end

    % ghost points tacked onr

    fnew(1,:)=fnew(2,:);

end % end of even parity if block


return
```

6.1.2.2 DiffusionTemp

This function calculates the Fuller-Schettler-Giddings diffusion constant at each point on the simulation grid for each species.

```
function [ FSGDiff ] = DiffusionTemp( temp,m1,m2,va,vb )
```

```
%Calculate diffusion coefficient based on temperature at each point using
%the Fuller-Schettler-Giddings equation.

FSGDiff=(0.001*temp.^1.75*(1/m1+1/m2)^0.5)/((va^(1/3)+vb^(1/3))^2);


end
```

6.1.2.3 Leftedge

This function calculates the densities of the species on the left edge of the simulation to serve as a boundary condition.

```
function [a,b,d,ee,f,g,h,k,l,m]= leftedge(N2,N2ion,N4ion,...
   H2O,H2Oion,H2O2,H2O3,H2O4,H2O5,H3O,Heion,He2ion,Hem,He1,e)
%Determine the densities of the species on the left edge of the simulation

%Define Rate Constants
kN2ion=7.1*10^-11*1e-6;
kH2OionN2=2.8*10^-9*1e-6;
kN4ion=1.4*10^-29*1e-12;
kN2recomb=3.5*10^-7*1e-6;
kN4recomb=2.60*10^-6*1e-6;
kH2OionN4=1.9*10^-9*1e-6;
kH2O2He=6.65e-28*1e-12;
knegH2O2N2=7e-26*1e-6;
knegH2O2He=1.37e-26*1e-6;
rateH2O3He=1.51e-26*1e-12;
negrateH2O3He=4e-17*1e-6;
rateH2O4He=1.5e-27*1e-12;
negrateH2O4He=4e-15*1e-6;
rateH2O5He=1e-29*1e-12;
negrateH2O5He=2e-10*1e-6;
kH3Oion=1.67e-9*1e-6;
kHemH2Oion=1.4e-9*1e-6;
kH2O2N2=3.4e-27*1e-6;
rateH2O3N2=2.3e-27*1e-12;
negrateH2O3N2=7e-18*1e-6;
rateH2O4N2=2.4e-27*1e-12;
negrateH2O4N2=4e-14*1e-6;
rateH2O5N2=2.5e-27*1e-12;
negrateH2O5N2=4e-10*1e-6;
kHeionN2=1.6e-9*1e-6;
kHeionH2O=5.6e-10*1e-6;
kHe2ionN2=1.3e-9*1e-6;
kHe2ionH2O=8e-10*1e-6;
kHeionrHem=3e-20*1e-12;
kHeionrHe=3e-20*1e-12;
```

```
kHe2ionrHem=8.9e-9*1e-12;
kHeionHe2=1.1e-31*1e-12;
kHemHeion=1.5e-9*1e-6;
kHemHe2ion=1.5e-9*1e-6;
kN4ionN2=2.5e-15*1e-6;
kH3Or=1.0e-6*1e-6;
kH2O2r=2.2e-6*1e-6;
kH2O3r=3.8e-6*1e-6;
kH2O4r=4.9e-6*1e-6;
kH2O5r=6.0e-6*1e-6;

%Conservation law for water, nitrogen, and helium.
H2O=H2O-H2Oion-H3O-2.*H2O2-3.*H2O3-4.*H2O4-5.*H2O5;
N2=N2-N2ion-2.*N4ion;
He1=He1-Hem-Heion-2.*He2ion;


a=zeros(14*2,1);
b=a;d=a;ee=a;f=a;g=a;h=a;k=a;l=a;m=a;


j=1;%Left Edge
   for i=2:14*2;

      %No Hem C and D Matrices
      A=[-kHeionN2*N2(i,j)-kHeionH2O*H2O(i,j)-kHeionrHem*e(i,j)^2-kHeionrHe*e(i,j)^2-
kHeionHe2*He1(i,j)^2 0;...
         kHeionHe2*He1(i,j)^2 -kHe2ionN2*N2(i,j)-kHe2ionrHem*e(i,j)-kHe2ionH2O*H2O(i,j)];
      Arhs=-[kHemHeion*Hem(i,j)^2;kHemHe2ion*Hem(i,j)^2];
      y=A\Arhs;
      a(i,j)=abs(y(1));
      b(i,j)=abs(y(2));


      A=[ -kH2OionN2*H2O(i,j)-kN4ion*N2(i,j).^2-kN2recomb*e(i,j)
kN4ionN2*N2(i,j)+kN4ion*He1(i,j) 0;
         kN4ion*N2(i,j).^2 -kN4recomb*e(i,j)-kH2OionN4*H2O(i,j)-kN4ionN2*N2(i,j)-
kN4ionN2*He1(i,j) 0;
         kH2OionN2*H2O(i,j) kH2OionN4*H2O(i,j) -kH3Oion*H2O(i,j)];
      Arhs=-
[(kN2ion*Hem(i,j)*N2(i,j)+kHeionN2*N2(i,j)*a(i,j));0;(kHemH2Oion*Hem(i,j)*H2O(i,j)+kHeionH2O*
H2O(i,j)*a(i,j)+kHe2ionH2O*H2O(i,j)*b(i,j))];
      y=A\Arhs;
      d(i,j)=abs(y(1));
      ee(i,j)=abs(y(2));
      f(i,j)=abs(y(3));



      A=[-kH2O2He*H2O(i,j)*He1(i,j)-kH2O2N2*H2O(i,j)*N2(i,j)-kH3Or*e(i,j)
(knegH2O2N2*N2(i,j)+knegH2O2He*He1(i,j)) 0 0 0;
```

```
        kH2O2He*H2O(i,j)*He1(i,j)+kH2O2N2*H2O(i,j)*N2(i,j) -rateH2O3He*H2O(i,j)*He1(i,j)-
rateH2O3N2*H2O(i,j)*N2(i,j)-knegH2O2N2*N2(i,j)-knegH2O2He*He1(i,j)-kH2O2r*e(i,j)...
        negrateH2O3He*He1(i,j)+negrateH2O3N2*N2(i,j) 0 0;
        0 rateH2O3He*H2O(i,j)*He1(i,j)+rateH2O3N2*H2O(i,j)*N2(i,j) (-negrateH2O3He*He1(i,j)-
negrateH2O3N2*N2(i,j)-rateH2O4He*H2O(i,j)*He1(i,j)-rateH2O4N2*H2O(i,j)*N2(i,j)-kH2O3r*e(i,j))...
        negrateH2O4He*He1(i,j)+negrateH2O4N2*N2(i,j) 0;
        0 0 rateH2O4He*H2O(i,j)*He1(i,j)+rateH2O4N2*H2O(i,j)*N2(i,j) (-negrateH2O4He*He1(i,j)-
negrateH2O4N2*N2(i,j)-rateH2O5He*H2O(i,j)*He1(i,j)-rateH2O5N2*H2O(i,j)*N2(i,j)-kH2O4r*e(i,j))...
         negrateH2O5He*He1(i,j)+negrateH2O5N2*N2(i,j);
        0 0 0 (rateH2O5He*H2O(i,j)*He1(i,j)+rateH2O5N2*H2O(i,j)*N2(i,j)) -negrateH2O5He*He1(i,j)-
negrateH2O5N2*N2(i,j)-kH2O5r*e(i,j)];
      Arhs=-[kH3Oion*H2O(i,j)*f(i,j);0;0;0;0];



      y=A\Arhs;
      g(i,j)=abs(y(1));
      h(i,j)=abs(y(2));
      k(i,j)=abs(y(3));
      l(i,j)=abs(y(4));
      m(i,j)=abs(y(5));



   end   % bottom of radial loop

   % tack on the i=1,2 boundary conditions
    a(1)=a(2);
    b(1)=b(2);
    d(1)=d(2);
    ee(1)=ee(2);
    f(1)=f(2);
    g(1)=g(2);
    h(1)=h(2);
    k(1)=k(2);
    l(1)=l(2);
    m(1)=m(2);

end
```

6.1.2.4 S0res

This function calculates the source term for He_m and He^+ based on the experimental data for the density of He_m.

```
function [S0Hem, S0Heion]=S0res(Hem,Heion,He2ion,e,N2,H2O)
%Calculates the source term for Hem and Heion for the space in the nozzle
%of the DC discharge.

%Define the radius and the axial distance from the beginning of the nozzle
r=0.001;
Z=0:0.125e-3/2:0.0045;
%Load the necessary rate constants
kHeionrHem=3e-20*1e-12;
kHe2ionrHem=8.9e-9*1e-12;
kN2ion=7.1*10^-11*1e-6;
kHemH2Oion=1.4e-9*1e-6;
kHemHeion=1.5e-9*1e-6;
kHemHe2ion=1.5e-9*1e-6;
%Calculate S0Hem based on the density of Hem from the experimental data.
%These values are not used in the simuation
S0Hem=Hem*0;
for i=2:17*2+1
   for j=2:33*2+1

S0Hem(i,j)=Hem(i,j)*(kN2ion.*N2(i,j)+kHemH2Oion.*H2O(i,j)+(kHemHeion+kHemHe2ion)*Hem(i,j))
...
   -(kHeionrHem.*Heion(i,j).*e(i,j).^2+kHe2ionrHem.*He2ion(i,j).*e(i,j));
   end
end

%Tack on the exponential decay of the source term in the nozzle.
for n=34*2:70*2
   %S0Hem(2:9,n)=S0Hem(2:9,33);
   S0Hem(2:19,n)=S0Hem(2:19,66).*exp(-2.4*Z(n-67)./r);
end

%Calculate S0Heion based on the expected relative densities of Heion and
%Hem
S0Heion=0.01*S0Hem;

return
```

6.1.2.5 CDoperator

This function calculates the amount that each species will convect and diffuse.

```
function [LCDn] =  CDoperator(istart,iend,jstart,jend,dr,dz,vr,vz,D,n,mask,north,east,west)

% Evaluate the convection-diffusion operator for the incoming density n

% istart is the first radial grid point to include in the iteration
% iend is the last radial grid point to include in the iteration
% jstart is the first axial grid point to include in the iteration
% jend is the last axisl grid point to include in the iteration
```

```
% dr is the radial grid spacing, cell center grid, r(i)=(i-1.5)*dr
% dz is the axial grid spacing, cell edge grid, z(j)=(j-1)*dz
% DAir is the diffusion coefficient (r,z) for species n in air
% DHe is the diffusion coefficient (r,z) for species n in helium
% n is the density of the species being solved for
% N2 is the air (nitrogen) density
% He is the helium density
% mask is 0 at metal points and at metal neighbor points, 1 at computation points
% D is the background density weighted diffusion coefficient
% north is 0 except at mask=1 points where the i+1 neighbor is metal
% east is 0 except at mask=1 points where the j+1 neighbor is metal
% west is 0 except at mask=1 points where the j-1 neighbor is metal

facrz = 0.5/(1/dr^2+1/dz^2);
fourdr2i=.25/dr^2;
fourdz2i=.25/dz^2;

r=zeros(iend+1,1);
r=((1:iend+1)-1.5)*dr;
rplus=r+0.5*dr;
rminus=r-0.5*dr;
rfac=1./(2*r*dr);
zfac=1/(2*dz);
dr2i=1/dr^2;
dz2i=1/dz^2;


gradDr=0.*D;gradDz=gradDr;Dr=gradDr;Dz=gradDz;vrp=gradDr;
LCDn=0.*D;
[isize,jsize]=size(D);

[imax,jmax]=size(D);

ii=2:(imax-1);jj=2:(jmax-1);
gradDr(ii,jj)=(D(ii+1,jj)-D(ii-1,jj))/(2*dr);
gradDz(ii,jj)=(D(ii,jj+1)-D(ii,jj-1))/(2*dz);
gradDz(ii,1)=gradDz(ii,2); % load the j=1 case, approximation
% one more factor in the denominator for computing grad(D).grad(n)
gradDr=gradDr/(2*dr);
gradDz=gradDz/(2*dz);


Drfacplus=(1+.5*dr./r);
Drfacminus=(1-.5*dr./r);


vrp=(vr(2,:)+3*vr(3,:))/(5*dr); % least squares fitting coefficient
                        % to vr(r) = vrp*r

% istart had better be 2 for the radial boundary condition below to work
if istart~=2
```

```
   disp(' istart is not 2 in convection-diffusion function CD')
   pause
end


% evaluate LCD(n)


   for i=iend:-1:istart % sweep toward Neumann boundary
   % for i=istart:iend


       % for j=jstart:jend  % j for loop

      j=jstart:jend;
      jm=j-1;
      if jstart==1
        jm(1)=1;
      end

       % build the two grad(D)grad(n) terms

        Dr(i,j)=gradDr(i,j).*(n(i+1,j)-n(i-1,j));
        Dz(i,j)=gradDz(i,j).*(n(i,j+1)-n(i,jm));
        % fix the j=1 point
        Dz(i,1)=Dz(i,2);


         % calculate the right hand side of the iteration and the
         % new density.

         % treat i=2 near the origin as a special case

         if i>2


               LCDn(i,j) = -rfac(i).*( r(i+1).*n(i+1,j).*vr(i+1,j)-r(i-1).*n(i-1,j).*vr(i-1,j))...
               -zfac*(n(i,j+1).*vz(i,j+1)-n(i,jm).*vz(i,jm))...
               +D(i,j).*( (n(i+1,j)-2.*n(i,j)+n(i-1,j) )*dr2i + ( n(i,j+1)-2*n(i,j)+n(i,jm) )*dz2i )...
               +D(i,j).*rfac(i).*(n(i+1,j)-n(i-1,j))...
               + Dr(i,j)+Dz(i,j);
               LCDn(i,j)=LCDn(i,j).*mask(i,j); % don't update in metal
               LCDn(i,1)=LCDn(i,2); % j=1 bandaid

         else  % this is the i=2 case

             LCDn(2,j) = (18*LCDn(3,j)+8*LCDn(4,j)-7*LCDn(5,j))/19;



         end   % end of i>2 if
```

```
      %  end % end of axial sweep

   end % end of radial sweep

   % tack on the boundary conditions
   LCDn(1,:)=LCDn(2,:);  % zero derivative at r=0
   LCDn(end,:)=2*LCDn(end-1,:)-LCDn(end-2,:);  % linearly extrapolate at iend
   LCDn(:,end)=2*LCDn(:,end-1)-LCDn(:,end-2);  % linearly extrapolate at jend
   % don't touch the left edge


   for i=iend:-1:istart  % sweep again to load the metal neighbor points from the updated interior points

      LCDn(i,j) = LCDn(i,j).*(1-north(i,j)).*(1-east(i,j)).*(1-west(i,j)) + ( LCDn(i-1,j).*north(i,j)...
            + LCDn(i,j+1).*west(i,j) + LCDn(i,jm).*east(i,j) )./(north(i,j)+east(i,j)+west(i,j)+1e-14);
          LCDn(35,67)=LCDn(35,67);
   end



   % tack on the boundary conditions
   LCDn(1,:)=LCDn(2,:);  % zero derivative at r=0
   LCDn(end,:)=2*LCDn(end-1,:)-LCDn(end-2,:);  % linearly extrapolate at iend
   LCDn(:,end)=2*LCDn(:,end-1)-LCDn(:,end-2);  % linearly extrapolate at jend
   LCDn(:,1)=2*LCDn(:,2)-LCDn(:,3); % copy the j=2 row into the  j=1 row so that we can use
                % implicitsolver on the j=1 radial row
end
```

6.1.2.6 Implicitsolverres

This function solves the chemistry for each species at each point on the simulation grid. It incorporates the factors obtained from CDoperator.

```
function [a,b,c,d,ee,f,g,h,k,l,m,error]= implicitsolverres(dt,N2,N2ion,N4ion,...
   H2O,H2Oion,H2O2,H2O3,H2O4,H2O5,H3O,Heion,He2ion,Hem,He1,...
   LCDHeion,LCDHe2ion,LCDHem,LCDN2ion,LCDN4ion,LCDH2Oion,LCDH3O,...
   LCDH2O2,LCDH2O3,LCDH2O4,LCDH2O5,e,S0Hem,S0Heion)
Nx=721;

%Define Rate Constants
kN2ion=7.1*10^-11*1e-6;
kH2OionN2=2.8*10^-9*1e-6;
kN4ion=1.4*10^-29*1e-12;
kN2recomb=3.5*10^-7*1e-6;
kN4recomb=2.60*10^-6*1e-6;
```

```
kH2OionN4=1.9*10^-9*1e-6;
kH2O2He=6.65e-28*1e-12;
knegH2O2N2=7e-26*1e-12;
rateH2O3He=1.51e-26*1e-12;
negrateH2O3He=4e-17*1e-6;
rateH2O4He=1.5e-27*1e-12;
negrateH2O4He=4e-15*1e-6;
rateH2O5He=1e-26*1e-12;
negrateH2O5He=2e-10*1e-6;
kH3Oion=1.67e-9*1e-6;
kHemH2Oion=1.4e-9*1e-6;
kH2O2N2=3.4e-27*1e-6;
rateH2O3N2=2.3e-27*1e-12;
negrateH2O3N2=7e-18*1e-6;
rateH2O4N2=2.4e-27*1e-12;
negrateH2O4N2=4e-14*1e-6;
rateH2O5N2=2.5e-27*1e-12;
negrateH2O5N2=4e-10*1e-6;
kHeionN2=1.6e-9*1e-6;
kHeionH2O=5.6e-10*1e-6;
kHe2ionN2=1.3e-9*1e-6;
kHe2ionH2O=8e-10*1e-6;
kHeionrHem=3e-20*1e-12;
kHeionrHe=3e-20*1e-12;
kHe2ionrHem=8.9e-9*1e-12;
kHeionHe2=1.1e-31*1e-12;
kHemHeion=1.5e-9*1e-6;
kHemHe2ion=1.5e-9*1e-6;
kN4ionN2=2.5e-15*1e-6;
kH3Or=1.0e-6*1e-6;
kH2O2r=2.2e-6*1e-6;
kH2O3r=3.8e-6*1e-6;
kH2O4r=4.9e-6*1e-6;
kH2O5r=6.0e-6*1e-6;

%Conservation law for water, nitrogen, and helium.
H2O=H2O-H2Oion-H3O-2.*H2O2-3.*H2O3-4.*H2O4-5.*H2O5;
N2=N2-N2ion-2.*N4ion;
He1=He1-Hem-Heion-2.*He2ion;

%Make sure that H2O, N2, and He don't go negative
H2O=max(H2O,0);
N2=max(N2,0);
He1=max(He1,0);

for j=2:67;
        for i=35:-1:3;
    %No Hem C and D Matrices

    C1=[-kHeionN2.*N2(i,j)-kHeionH2O.*H2O(i,j)-kHeionrHem.*e(i,j).^2-kHeionrHe.*e(i,j).^2-
kHeionHe2.*He1(i,j).^2 0 0 0 0 0 0 0 0 0;
```

```
        kHeionHe2.*He1(i,j).^2 -kHe2ionN2.*N2(i,j)-kHe2ionrHem.*e(i,j) 0 0 0 0 0 0 0 0;
        kHeionN2.*N2(i,j) 0  -kH2OionN2.*H2O(i,j)-kN4ion.*N2(i,j).^2-kN2recomb.*e(i,j)
kN4ionN2.*N2(i,j)+kN4ion.*He1(i,j) 0 0 0 0 0 0;
        0 0 kN4ion.*N2(i,j).^2 -kN4recomb.*e(i,j)-kH2OionN4.*H2O(i,j)-kN4ionN2.*N2(i,j)-
kN4ionN2.*He1(i,j) 0 0 0 0 0 0;
        kHeionH2O.*H2O(i,j) kHe2ionH2O.*H2O(i,j) kH2OionN2.*H2O(i,j) kH2OionN4.*H2O(i,j) -
kH3Oion.*H2O(i,j) 0 0 0 0 0;
        0 0 0 0 kH3Oion.*H2O(i,j) -kH2O2He.*H2O(i,j).*He1(i,j)-kH2O2N2.*H2O(i,j).*N2(i,j)-
kH3Or.*e(i,j) knegH2O2N2.*N2(i,j) 0 0 0;
        0 0 0 0 0 kH2O2He.*H2O(i,j).*He1(i,j)+kH2O2N2.*H2O(i,j).*N2(i,j) -
rateH2O3He.*H2O(i,j).*He1(i,j)-rateH2O3N2.*H2O(i,j).*N2(i,j)-knegH2O2N2.*N2(i,j)-kH2O2r.*e(i,j)...
        negrateH2O3He.*He1(i,j)+negrateH2O3N2.*N2(i,j) 0 0
        0 0 0 0 0 0 rateH2O3He.*H2O(i,j).*He1(i,j)+rateH2O3N2.*H2O(i,j).*N2(i,j) (-
negrateH2O3He.*He1(i,j)-negrateH2O3N2.*N2(i,j)-rateH2O4He.*H2O(i,j).*He1(i,j)-
rateH2O4N2.*H2O(i,j).*N2(i,j)-kH2O3r.*e(i,j))...
        negrateH2O4He.*He1(i,j)+negrateH2O4N2.*N2(i,j) 0;
        0 0 0 0 0 0 0 rateH2O4He.*H2O(i,j).*He1(i,j)+rateH2O4N2.*H2O(i,j).*N2(i,j) (-
negrateH2O4He.*He1(i,j)-negrateH2O4N2.*N2(i,j)-rateH2O5He.*H2O(i,j).*He1(i,j)-
rateH2O5N2.*H2O(i,j).*N2(i,j)-kH2O4r.*e(i,j))...
        negrateH2O5He.*He1(i,j)+negrateH2O5N2.*N2(i,j);
        0 0 0 0 0 0 0 0 rateH2O5He.*H2O(i,j).*He1(i,j)+rateH2O5N2.*H2O(i,j).*N2(i,j) -
negrateH2O5He.*He1(i,j)-negrateH2O5N2.*N2(i,j)-kH2O5r.*e(i,j)];


D1=[kHemHeion*Hem(i,j)^2;kHemHe2ion*Hem(i,j)^2;kN2ion*Hem(i,j)*N2(i,j);0;kHemH2Oion*Hem(
i,j)*H2O(i,j);0;0;0;0;0];
    %Solve Implicitly

n=[Heion(i,j);He2ion(i,j);N2ion(i,j);N4ion(i,j);H2Oion(i,j);H3O(i,j);H2O2(i,j);H2O3(i,j);H2O4(i,j);H2O5
(i,j)];

LCD=[LCDHeion(i,j);LCDHe2ion(i,j);LCDN2ion(i,j);LCDN4ion(i,j);LCDH2Oion(i,j);LCDH3O(i,j);...
        LCDH2O2(i,j);LCDH2O3(i,j);LCDH2O4(i,j);LCDH2O5(i,j)];


    A=eye(10,10)-C1*dt;
    B=(n+D1*dt+LCD*dt);
    n=A\B;

    Heion(i,j)=n(1);
    He2ion(i,j)=n(2);
    N2ion(i,j)=n(3);
    N4ion(i,j)=n(4);
    H2Oion(i,j)=n(5);
    H3O(i,j)=n(6);
    H2O2(i,j)=n(7);
    H2O3(i,j)=n(8);
    H2O4(i,j)=n(9);
    H2O5(i,j)=n(10);
      end
end
```

```
for j=68:140;
        for i=19:-1:3;
    %Hem C and D Matrices

    C2=[-kHeionN2.*N2(i,j)-kHeionH2O.*H2O(i,j)-kHeionrHem.*e(i,j).^2-kHeionrHe.*e(i,j).^2-
kHeionHe2.*He1(i,j).^2 0 kHemHeion*Hem(i,j) 0 0 0 0 0 0 0 0;
        kHeionHe2.*He1(i,j).^2 -kHe2ionN2.*N2(i,j)-kHe2ionrHem.*e(i,j) kHemHe2ion*Hem(i,j) 0 0 0 0
0 0 0 0;
        kHeionrHem.*e(i,j).^2 kHe2ionrHem.*e(i,j) -kN2ion.*N2(i,j)-kHemH2Oion.*H2O(i,j)-
(kHemHeion+kHemHe2ion)*Hem(i,j) 0 0 0 0 0 0 0 0;
        kHeionN2.*N2(i,j) kHe2ionN2.*N2(i,j) kN2ion.*N2(i,j) -kH2OionN2.*H2O(i,j)-
kN4ion.*N2(i,j).^2-kN2recomb.*e(i,j) kN4ionN2.*N2(i,j)+kN4ion.*He1(i,j) 0 0 0 0 0 0;
        0 0 kHemH2Oion.*H2O(i,j) kN4ion.*N2(i,j).^2 -kN4recomb.*e(i,j)-kH2OionN4.*H2O(i,j)-
kN4ionN2.*N2(i,j)-kN4ionN2.*He1(i,j) 0 0 0 0 0 0;
        kHeionH2O.*H2O(i,j) kHe2ionH2O.*H2O(i,j) 0 kH2OionN2.*H2O(i,j) kH2OionN4.*H2O(i,j) -
kH3Oion.*H2O(i,j) 0 0 0 0 0;
        0 0 0 0 0 kH3Oion.*H2O(i,j) -kH2O2He.*H2O(i,j).*He1(i,j)-kH2O2N2.*H2O(i,j).*N2(i,j)-
kH3Or.*e(i,j) knegH2O2N2.*N2(i,j) 0 0 0;
        0 0 0 0 0 0 kH2O2He.*H2O(i,j).*He1(i,j)+kH2O2N2.*H2O(i,j).*N2(i,j) -
rateH2O3He.*H2O(i,j).*He1(i,j)-rateH2O3N2.*H2O(i,j).*N2(i,j)-knegH2O2N2.*N2(i,j)-kH2O2r.*e(i,j)...
        negrateH2O3He.*He1(i,j)+negrateH2O3N2.*N2(i,j) 0 0
        0 0 0 0 0 0 0 rateH2O3He.*H2O(i,j).*He1(i,j)+rateH2O3N2.*H2O(i,j).*N2(i,j) (-
negrateH2O3He.*He1(i,j)-negrateH2O3N2.*N2(i,j)-rateH2O4He.*H2O(i,j).*He1(i,j)-
rateH2O4N2.*H2O(i,j).*N2(i,j)-kH2O3r.*e(i,j))...
        negrateH2O4He.*He1(i,j)+negrateH2O4N2.*N2(i,j) 0;
        0 0 0 0 0 0 0 0 rateH2O4He.*H2O(i,j).*He1(i,j)+rateH2O4N2.*H2O(i,j).*N2(i,j) (-
negrateH2O4He.*He1(i,j)-negrateH2O4N2.*N2(i,j)-rateH2O5He.*H2O(i,j).*He1(i,j)-
rateH2O5N2.*H2O(i,j).*N2(i,j)-kH2O4r.*e(i,j))...
        negrateH2O5He.*He1(i,j)+negrateH2O5N2.*N2(i,j);
        0 0 0 0 0 0 0 0 0 rateH2O5He.*H2O(i,j).*He1(i,j)+rateH2O5N2.*H2O(i,j).*N2(i,j) -
negrateH2O5He.*He1(i,j)-negrateH2O5N2.*N2(i,j)-kH2O5r.*e(i,j)];

    D2=[S0Heion(i,j);0;S0Hem(i,j);0;0;0;0;0;0;0;0];

    %Solve Implicitly

n=[Heion(i,j);He2ion(i,j);Hem(i,j);N2ion(i,j);N4ion(i,j);H2Oion(i,j);H3O(i,j);H2O2(i,j);H2O3(i,j);H2O4(
i,j);H2O5(i,j)];

LCD=[LCDHeion(i,j);LCDHe2ion(i,j);LCDHem(i,j);LCDN2ion(i,j);LCDN4ion(i,j);LCDH2Oion(i,j);LC
DH3O(i,j);...
        LCDH2O2(i,j);LCDH2O3(i,j);LCDH2O4(i,j);LCDH2O5(i,j)];


    A=eye(11,11)-C2*dt;
    B=(n+D2*dt+LCD*dt);
    n=A\B;

    Heion(i,j)=n(1);
    He2ion(i,j)=n(2);
```

```
        Hem(i,j)=n(3);
        N2ion(i,j)=n(4);
        N4ion(i,j)=n(5);
        H2Oion(i,j)=n(6);
        H3O(i,j)=n(7);
        H2O2(i,j)=n(8);
        H2O3(i,j)=n(9);
        H2O4(i,j)=n(10);
        H2O5(i,j)=n(11);
          end
end
error=0;
for j=141:Nx-1;
          for i=100:-1:3;%Ny-1;
        %Hem C and D Matrices

        C3=[-kHeionN2.*N2(i,j)-kHeionH2O.*H2O(i,j)-kHeionrHem.*e(i,j).^2-kHeionrHe.*e(i,j).^2-
kHeionHe2.*He1(i,j).^2 0 kHemHeion*Hem(i,j) 0 0 0 0 0 0 0 0;
          kHeionHe2.*He1(i,j).^2 -kHe2ionN2.*N2(i,j)-kHe2ionrHem.*e(i,j) kHemHe2ion*Hem(i,j) 0 0 0 0
0 0 0 0;
          kHeionrHem.*e(i,j).^2 kHe2ionrHem.*e(i,j) -kN2ion.*N2(i,j)-kHemH2Oion.*H2O(i,j)-
(kHemHeion+kHemHe2ion)*Hem(i,j) 0 0 0 0 0 0 0 0;
          kHeionN2.*N2(i,j) kHe2ionN2.*N2(i,j) kN2ion.*N2(i,j) -kH2OionN2.*H2O(i,j)-
kN4ion.*N2(i,j).^2-kN2recomb.*e(i,j) kN4ionN2.*N2(i,j)+kN4ion.*He1(i,j) 0 0 0 0 0 0;
          0 0 kHemH2Oion.*H2O(i,j) kN4ion.*N2(i,j).^2 -kN4recomb.*e(i,j)-kH2OionN4.*H2O(i,j)-
kN4ionN2.*N2(i,j)-kN4ionN2.*He1(i,j) 0 0 0 0 0 0;
          kHeionH2O.*H2O(i,j) kHe2ionH2O.*H2O(i,j) 0 kH2OionN2.*H2O(i,j) kH2OionN4.*H2O(i,j) -
kH3Oion.*H2O(i,j) 0 0 0 0 0;
          0 0 0 0 0 kH3Oion.*H2O(i,j) -kH2O2He.*H2O(i,j).*He1(i,j)-kH2O2N2.*H2O(i,j).*N2(i,j)-
kH3Or.*e(i,j) knegH2O2N2.*N2(i,j) 0 0 0;
          0 0 0 0 0 0 kH2O2He.*H2O(i,j).*He1(i,j)+kH2O2N2.*H2O(i,j).*N2(i,j) -
rateH2O3He.*H2O(i,j).*He1(i,j)-rateH2O3N2.*H2O(i,j).*N2(i,j)-knegH2O2N2.*N2(i,j)-kH2O2r.*e(i,j)...
          negrateH2O3He.*He1(i,j)+negrateH2O3N2.*N2(i,j) 0 0
          0 0 0 0 0 0 0 rateH2O3He.*H2O(i,j).*He1(i,j)+rateH2O3N2.*H2O(i,j).*N2(i,j) (-
negrateH2O3He.*He1(i,j)-negrateH2O3N2.*N2(i,j)-rateH2O4He.*H2O(i,j).*He1(i,j)-
rateH2O4N2.*H2O(i,j).*N2(i,j)-kH2O3r.*e(i,j))...
          negrateH2O4He.*He1(i,j)+negrateH2O4N2.*N2(i,j) 0;
          0 0 0 0 0 0 0 0 rateH2O4He.*H2O(i,j).*He1(i,j)+rateH2O4N2.*H2O(i,j).*N2(i,j) (-
negrateH2O4He.*He1(i,j)-negrateH2O4N2.*N2(i,j)-rateH2O5He.*H2O(i,j).*He1(i,j)-
rateH2O5N2.*H2O(i,j).*N2(i,j)-kH2O4r.*e(i,j))...
          negrateH2O5He.*He1(i,j)+negrateH2O5N2.*N2(i,j);
          0 0 0 0 0 0 0 0 0 rateH2O5He.*H2O(i,j).*He1(i,j)+rateH2O5N2.*H2O(i,j).*N2(i,j) -
negrateH2O5He.*He1(i,j)-negrateH2O5N2.*N2(i,j)-kH2O5r.*e(i,j)];

        D3=[S0Heion(i,j);0;S0Hem(i,j);0;0;0;0;0;0;0;0];

        %Solve Implicitly

n=[Heion(i,j);He2ion(i,j);Hem(i,j);N2ion(i,j);N4ion(i,j);H2Oion(i,j);H3O(i,j);H2O2(i,j);H2O3(i,j);H2O4(
i,j);H2O5(i,j)];
```

```
LCD=[LCDHeion(i,j);LCDHe2ion(i,j);LCDHem(i,j);LCDN2ion(i,j);LCDN4ion(i,j);LCDH2Oion(i,j);LC
DH3O(i,j);...
        LCDH2O2(i,j);LCDH2O3(i,j);LCDH2O4(i,j);LCDH2O5(i,j)];

      A=eye(11,11)-C3*dt;
     B=(n+D3*dt+LCD*dt);
     %Determine the error for convergence purposes
     if j>66 && j<600 && i<40 % only look where the densities are interesting
      An=A*n; % density weighted error, Lhs=Rhs==An=B
      cm=An-B;
      cp=An+B;
      err=abs(cm)./abs(cp).*n/sum(n);
      err=max(err);
      error=max(error,err);
     end
      n=A\B;

      Heion(i,j)=n(1);
      He2ion(i,j)=n(2);
      Hem(i,j)=n(3);
      N2ion(i,j)=n(4);
      N4ion(i,j)=n(5);
      H2Oion(i,j)=n(6);
      H3O(i,j)=n(7);
      H2O2(i,j)=n(8);
      H2O3(i,j)=n(9);
      H2O4(i,j)=n(10);
      H2O5(i,j)=n(11);
        end
end

% Put on the i=2 points near the origin by least-squares fitting to points
% i=3,4,5

j=2:Nx;
i=2;
      %Least squares fit to i=3,4, and 5
      Heion(i,j)=(18*Heion(i+1,j)+8*Heion(i+2,j)-7*Heion(i+3,j))/19;
      He2ion(i,j)=(18*He2ion(i+1,j)+8*He2ion(i+2,j)-7*He2ion(i+3,j))/19;
      N2ion(i,j)=(18*N2ion(i+1,j)+8*N2ion(i+2,j)-7*N2ion(i+3,j))/19;
      N4ion(i,j)=(18*N4ion(i+1,j)+8*N4ion(i+2,j)-7*N4ion(i+3,j))/19;
      H2Oion(i,j)=(18*H2Oion(i+1,j)+8*H2Oion(i+2,j)-7*H2Oion(i+3,j))/19;
      H3O(i,j)=(18*H3O(i+1,j)+8*H3O(i+2,j)-7*H3O(i+3,j))/19;
      H2O2(i,j)=(18*H2O2(i+1,j)+8*H2O2(i+2,j)-7*H2O2(i+3,j))/19;
      H2O3(i,j)=(18*H2O3(i+1,j)+8*H2O3(i+2,j)-7*H2O3(i+3,j))/19;
      H2O4(i,j)=(18*H2O4(i+1,j)+8*H2O4(i+2,j)-7*H2O4(i+3,j))/19;
      H2O5(i,j)=(18*H2O5(i+1,j)+8*H2O5(i+2,j)-7*H2O5(i+3,j))/19;
      % adjust the Hemnew data to a parabola near the origin
      Hem(i,j)=(18*Hem(i+1,j)+8*Hem(i+2,j)-7*Hem(i+3,j))/19;
```

```
    % return densities and keep them positive
a=abs(Heion);b=abs(He2ion);c=abs(Hem);d=abs(N2ion);ee=abs(N4ion);f=abs(H2Oion);g=abs(H3O);
h=abs(H2O2);k=abs(H2O3);l=abs(H2O4);m=abs(H2O5);
end
```

6.1.2.7 ImplicitsolverS0

The same as implicitsolver, but allows the He_m and He^+ densities to change in the active discharge region as the impurity and humidity levels are changed.

```
function [a,b,c,d,ee,f,g,h,k,l,m,error]= implicitsolverS0(dt,N2,N2ion,N4ion,...
    H2O,H2Oion,H2O2,H2O3,H2O4,H2O5,H3O,Heion,He2ion,Hem,He1,...
    LCDHeion,LCDHe2ion,LCDHem,LCDN2ion,LCDN4ion,LCDH2Oion,LCDH3O,...
    LCDH2O2,LCDH2O3,LCDH2O4,LCDH2O5,e,S0Hem,S0Heion)
%Implicity chemistry solver for impurity runs
Nx=721;
%Define Rate Constants
kN2ion=7.1*10^-11*1e-6;
kH2OionN2=2.8*10^-9*1e-6;
kN4ion=1.4*10^-29*1e-12;
kN2recomb=3.5*10^-7*1e-6;
kN4recomb=2.60*10^-6*1e-6;
kH2OionN4=1.9*10^-9*1e-6;
kH2O2He=6.65e-28*1e-12;
knegH2O2N2=7e-26*1e-12;
rateH2O3He=1.51e-26*1e-12;
negrateH2O3He=4e-17*1e-6;
rateH2O4He=1.5e-27*1e-12;
negrateH2O4He=4e-15*1e-6;
rateH2O5He=1e-26*1e-12;
negrateH2O5He=2e-10*1e-6;
kH3Oion=1.67e-9*1e-6;
kHemH2Oion=1.4e-9*1e-6;
kH2O2N2=3.4e-27*1e-6;
rateH2O3N2=2.3e-27*1e-12;
negrateH2O3N2=7e-18*1e-6;
rateH2O4N2=2.4e-27*1e-12;
negrateH2O4N2=4e-14*1e-6;
rateH2O5N2=2.5e-27*1e-12;
negrateH2O5N2=4e-10*1e-6;
kHeionN2=1.6e-9*1e-6;
kHeionH2O=5.6e-10*1e-6;
kHe2ionN2=1.3e-9*1e-6;
kHe2ionH2O=8e-10*1e-6;
kHeionrHem=3e-20*1e-12;
kHeionrHe=3e-20*1e-12;
kHe2ionrHem=8.9e-9*1e-12;
kHeionHe2=1.1e-31*1e-12;
```

```
kHemHeion=1.5e-9*1e-6;
kHemHe2ion=1.5e-9*1e-6;
kN4ionN2=2.5e-15*1e-6;
kH3Or=1.0e-6*1e-6;
kH2O2r=2.2e-6*1e-6;
kH2O3r=3.8e-6*1e-6;
kH2O4r=4.9e-6*1e-6;
kH2O5r=6.0e-6*1e-6;

%Conservation law for water, nitrogen, and helium.
H2O=H2O-H2Oion-H3O-2.*H2O2-3.*H2O3-4.*H2O4-5.*H2O5;
N2=N2-N2ion-2.*N4ion;
He1=He1-Hem-Heion-2.*He2ion;
%Make sure H2O, N2, and He don't go negative
H2O=max(H2O,0);
N2=max(N2,0);
He1=max(He1,0);


for j=2:67;
        for i=35:-1:3;
    %C and D Matrices
    C1=[-kHeionN2.*N2(i,j)-kHeionH2O.*H2O(i,j)-kHeionrHem.*e(i,j).^2-kHeionrHe.*e(i,j).^2-
kHeionHe2.*He1(i,j).^2 0 kHemHeion*Hem(i,j) 0 0 0 0 0 0 0 0;
        kHeionHe2.*He1(i,j).^2 -kHe2ionN2.*N2(i,j)-kHe2ionrHem.*e(i,j) kHemHe2ion*Hem(i,j) 0 0 0 0
0 0 0 0;
        kHeionrHem.*e(i,j).^2 kHe2ionrHem.*e(i,j) -kN2ion.*N2(i,j)-kHemH2Oion.*H2O(i,j)-
(kHemHeion+kHemHe2ion)*Hem(i,j) 0 0 0 0 0 0 0 0;
        kHeionN2.*N2(i,j) kHe2ionN2.*N2(i,j) kN2ion.*N2(i,j) -kH2OionN2.*H2O(i,j)-
kN4ion.*N2(i,j).^2-kN2recomb.*e(i,j) kN4ionN2.*N2(i,j)+kN4ion.*He1(i,j) 0 0 0 0 0 0;
        0 0 kHemH2Oion.*H2O(i,j) kN4ion.*N2(i,j).^2 -kN4recomb.*e(i,j)-kH2OionN4.*H2O(i,j)-
kN4ionN2.*N2(i,j)-kN4ionN2.*He1(i,j) 0 0 0 0 0 0;
        kHeionH2O.*H2O(i,j) kHe2ionH2O.*H2O(i,j) 0 kH2OionN2.*H2O(i,j) kH2OionN4.*H2O(i,j) -
kH3Oion.*H2O(i,j) 0 0 0 0 0;
        0 0 0 0 0 kH3Oion.*H2O(i,j) -kH2O2He.*H2O(i,j).*He1(i,j)-kH2O2N2.*H2O(i,j).*N2(i,j)-
kH3Or.*e(i,j) knegH2O2N2.*N2(i,j) 0 0 0;
        0 0 0 0 0 0 kH2O2He.*H2O(i,j).*He1(i,j)+kH2O2N2.*H2O(i,j).*N2(i,j) -
rateH2O3He.*H2O(i,j).*He1(i,j)-rateH2O3N2.*H2O(i,j).*N2(i,j)-knegH2O2N2.*N2(i,j)-kH2O2r.*e(i,j)...
        negrateH2O3He.*He1(i,j)+negrateH2O3N2.*N2(i,j) 0 0
        0 0 0 0 0 0 0 rateH2O3He.*H2O(i,j).*He1(i,j)+rateH2O3N2.*H2O(i,j).*N2(i,j) (-
negrateH2O3He.*He1(i,j)-negrateH2O3N2.*N2(i,j)-rateH2O4He.*H2O(i,j).*He1(i,j)-
rateH2O4N2.*H2O(i,j).*N2(i,j)-kH2O3r.*e(i,j))...
        negrateH2O4He.*He1(i,j)+negrateH2O4N2.*N2(i,j) 0;
        0 0 0 0 0 0 0 0 rateH2O4He.*H2O(i,j).*He1(i,j)+rateH2O4N2.*H2O(i,j).*N2(i,j) (-
negrateH2O4He.*He1(i,j)-negrateH2O4N2.*N2(i,j)-rateH2O5He.*H2O(i,j).*He1(i,j)-
rateH2O5N2.*H2O(i,j).*N2(i,j)-kH2O4r.*e(i,j))...
        negrateH2O5He.*He1(i,j)+negrateH2O5N2.*N2(i,j);
        0 0 0 0 0 0 0 0 0 rateH2O5He.*H2O(i,j).*He1(i,j)+rateH2O5N2.*H2O(i,j).*N2(i,j) -
negrateH2O5He.*He1(i,j)-negrateH2O5N2.*N2(i,j)-kH2O5r.*e(i,j)];

    D1=[S0Heion(i,j);0;S0Hem(i,j);0;0;0;0;0;0;0;0];
```

```
    %Solve Implicitly

n=[Heion(i,j);He2ion(i,j);Hem(i,j);N2ion(i,j);N4ion(i,j);H2Oion(i,j);H3O(i,j);H2O2(i,j);H2O3(i,j);H2O4(
i,j);H2O5(i,j)];

LCD=[LCDHeion(i,j);LCDHe2ion(i,j);LCDHem(i,j);LCDN2ion(i,j);LCDN4ion(i,j);LCDH2Oion(i,j);LC
DH3O(i,j);...
      LCDH2O2(i,j);LCDH2O3(i,j);LCDH2O4(i,j);LCDH2O5(i,j)];


    A=eye(11,11)-C1*dt;
    B=(n+D1*dt+LCD*dt);
    n=A\B;

    Heion(i,j)=n(1);
    He2ion(i,j)=n(2);
    Hem(i,j)=n(3);
    N2ion(i,j)=n(4);
    N4ion(i,j)=n(5);
    H2Oion(i,j)=n(6);
    H3O(i,j)=n(7);
    H2O2(i,j)=n(8);
    H2O3(i,j)=n(9);
    H2O4(i,j)=n(10);
    H2O5(i,j)=n(11);
      end
end




for j=68:140;
      for i=19:-1:3;
    %Hem C and D Matrices

    C2=[-kHeionN2.*N2(i,j)-kHeionH2O.*H2O(i,j)-kHeionrHem.*e(i,j).^2-kHeionrHe.*e(i,j).^2-
kHeionHe2.*He1(i,j).^2 0 kHemHeion*Hem(i,j) 0 0 0 0 0 0 0 0;
      kHeionHe2.*He1(i,j).^2 -kHe2ionN2.*N2(i,j)-kHe2ionrHem.*e(i,j) kHemHe2ion*Hem(i,j) 0 0 0 0
0 0 0 0;
      kHeionrHem.*e(i,j).^2 kHe2ionrHem.*e(i,j) -kN2ion.*N2(i,j)-kHemH2Oion.*H2O(i,j)-
(kHemHeion+kHemHe2ion)*Hem(i,j) 0 0 0 0 0 0 0 0;
      kHeionN2.*N2(i,j) kHe2ionN2.*N2(i,j) kN2ion.*N2(i,j) -kH2OionN2.*H2O(i,j)-
kN4ion.*N2(i,j).^2-kN2recomb.*e(i,j) kN4ionN2.*N2(i,j)+kN4ion.*He1(i,j) 0 0 0 0 0 0;
      0 0 kHemH2Oion.*H2O(i,j) kN4ion.*N2(i,j).^2 -kN4recomb.*e(i,j)-kH2OionN4.*H2O(i,j)-
kN4ionN2.*N2(i,j)-kN4ionN2.*He1(i,j) 0 0 0 0 0 0;
      kHeionH2O.*H2O(i,j) kHe2ionH2O.*H2O(i,j) 0 kH2OionN2.*H2O(i,j) kH2OionN4.*H2O(i,j) -
kH3Oion.*H2O(i,j) 0 0 0 0 0;
      0 0 0 0 0 kH3Oion.*H2O(i,j) -kH2O2He.*H2O(i,j).*He1(i,j)-kH2O2N2.*H2O(i,j).*N2(i,j)-
kH3Or.*e(i,j) knegH2O2N2.*N2(i,j) 0 0 0;
```

```
        0 0 0 0 0 0 kH2O2He.*H2O(i,j).*He1(i,j)+kH2O2N2.*H2O(i,j).*N2(i,j) -
rateH2O3He.*H2O(i,j).*He1(i,j)-rateH2O3N2.*H2O(i,j).*N2(i,j)-knegH2O2N2.*N2(i,j)-kH2O2r.*e(i,j)...
        negrateH2O3He.*He1(i,j)+negrateH2O3N2.*N2(i,j) 0 0
        0 0 0 0 0 0 0 rateH2O3He.*H2O(i,j).*He1(i,j)+rateH2O3N2.*H2O(i,j).*N2(i,j) (-
negrateH2O3He.*He1(i,j)-negrateH2O3N2.*N2(i,j)-rateH2O4He.*H2O(i,j).*He1(i,j)-
rateH2O4N2.*H2O(i,j).*N2(i,j)-kH2O3r.*e(i,j))...
        negrateH2O4He.*He1(i,j)+negrateH2O4N2.*N2(i,j) 0;
        0 0 0 0 0 0 0 0 rateH2O4He.*H2O(i,j).*He1(i,j)+rateH2O4N2.*H2O(i,j).*N2(i,j) (-
negrateH2O4He.*He1(i,j)-negrateH2O4N2.*N2(i,j)-rateH2O5He.*H2O(i,j).*He1(i,j)-
rateH2O5N2.*H2O(i,j).*N2(i,j)-kH2O4r.*e(i,j))...
        negrateH2O5He.*He1(i,j)+negrateH2O5N2.*N2(i,j);
        0 0 0 0 0 0 0 0 0 rateH2O5He.*H2O(i,j).*He1(i,j)+rateH2O5N2.*H2O(i,j).*N2(i,j) -
negrateH2O5He.*He1(i,j)-negrateH2O5N2.*N2(i,j)-kH2O5r.*e(i,j)];

    D2=[S0Heion(i,j);0;S0Hem(i,j);0;0;0;0;0;0;0;0];

    %Solve Implicitly

n=[Heion(i,j);He2ion(i,j);Hem(i,j);N2ion(i,j);N4ion(i,j);H2Oion(i,j);H3O(i,j);H2O2(i,j);H2O3(i,j);H2O4(
i,j);H2O5(i,j)];

LCD=[LCDHeion(i,j);LCDHe2ion(i,j);LCDHem(i,j);LCDN2ion(i,j);LCDN4ion(i,j);LCDH2Oion(i,j);LC
DH3O(i,j);...
        LCDH2O2(i,j);LCDH2O3(i,j);LCDH2O4(i,j);LCDH2O5(i,j)];


    A=eye(11,11)-C2*dt;
    B=(n+D2*dt+LCD*dt);
    n=A\B;

    Heion(i,j)=n(1);
    He2ion(i,j)=n(2);
    Hem(i,j)=n(3);
    N2ion(i,j)=n(4);
    N4ion(i,j)=n(5);
    H2Oion(i,j)=n(6);
    H3O(i,j)=n(7);
    H2O2(i,j)=n(8);
    H2O3(i,j)=n(9);
    H2O4(i,j)=n(10);
    H2O5(i,j)=n(11);
      end
end
error=0;
for j=141:Nx-1;
        for i=100:-1:3;%Ny-1;
    %Hem C and D Matrices

    C3=[-kHeionN2.*N2(i,j)-kHeionH2O.*H2O(i,j)-kHeionrHem.*e(i,j).^2-kHeionrHe.*e(i,j).^2-
kHeionHe2.*He1(i,j).^2 0 kHemHeion*Hem(i,j) 0 0 0 0 0 0 0 0;
```

```
        kHeionHe2.*He1(i,j).^2 -kHe2ionN2.*N2(i,j)-kHe2ionrHem.*e(i,j) kHemHe2ion*Hem(i,j) 0 0 0 0
0 0 0 0;
        kHeionrHem.*e(i,j).^2 kHe2ionrHem.*e(i,j) -kN2ion.*N2(i,j)-kHemH2Oion.*H2O(i,j)-
(kHemHeion+kHemHe2ion)*Hem(i,j) 0 0 0 0 0 0 0 0;
        kHeionN2.*N2(i,j) kHe2ionN2.*N2(i,j) kN2ion.*N2(i,j) -kH2OionN2.*H2O(i,j)-
kN4ion.*N2(i,j).^2-kN2recomb.*e(i,j) kN4ionN2.*N2(i,j)+kN4ion.*He1(i,j) 0 0 0 0 0 0;
        0 0 kHemH2Oion.*H2O(i,j) kN4ion.*N2(i,j).^2 -kN4recomb.*e(i,j)-kH2OionN4.*H2O(i,j)-
kN4ionN2.*N2(i,j)-kN4ionN2.*He1(i,j) 0 0 0 0 0 0;
        kHeionH2O.*H2O(i,j) kHe2ionH2O.*H2O(i,j) 0 kH2OionN2.*H2O(i,j) kH2OionN4.*H2O(i,j) -
kH3Oion.*H2O(i,j) 0 0 0 0 0;
        0 0 0 0 0 kH3Oion.*H2O(i,j) -kH2O2He.*H2O(i,j).*He1(i,j)-kH2O2N2.*H2O(i,j).*N2(i,j)-
kH3Or.*e(i,j) knegH2O2N2.*N2(i,j) 0 0 0;
        0 0 0 0 0 0 kH2O2He.*H2O(i,j).*He1(i,j)+kH2O2N2.*H2O(i,j).*N2(i,j) -
rateH2O3He.*H2O(i,j).*He1(i,j)-rateH2O3N2.*H2O(i,j).*N2(i,j)-knegH2O2N2.*N2(i,j)-kH2O2r.*e(i,j)...
        negrateH2O3He.*He1(i,j)+negrateH2O3N2.*N2(i,j) 0 0
        0 0 0 0 0 0 0 rateH2O3He.*H2O(i,j).*He1(i,j)+rateH2O3N2.*H2O(i,j).*N2(i,j) (-
negrateH2O3He.*He1(i,j)-negrateH2O3N2.*N2(i,j)-rateH2O4He.*H2O(i,j).*He1(i,j)-
rateH2O4N2.*H2O(i,j).*N2(i,j)-kH2O3r.*e(i,j))...
        negrateH2O4He.*He1(i,j)+negrateH2O4N2.*N2(i,j) 0;
        0 0 0 0 0 0 0 0 rateH2O4He.*H2O(i,j).*He1(i,j)+rateH2O4N2.*H2O(i,j).*N2(i,j) (-
negrateH2O4He.*He1(i,j)-negrateH2O4N2.*N2(i,j)-rateH2O5He.*H2O(i,j).*He1(i,j)-
rateH2O5N2.*H2O(i,j).*N2(i,j)-kH2O4r.*e(i,j))...
        negrateH2O5He.*He1(i,j)+negrateH2O5N2.*N2(i,j);
        0 0 0 0 0 0 0 0 0 rateH2O5He.*H2O(i,j).*He1(i,j)+rateH2O5N2.*H2O(i,j).*N2(i,j) -
negrateH2O5He.*He1(i,j)-negrateH2O5N2.*N2(i,j)-kH2O5r.*e(i,j)];

    D3=[S0Heion(i,j);0;S0Hem(i,j);0;0;0;0;0;0;0;0];

    %Solve Implicitly

n=[Heion(i,j);He2ion(i,j);Hem(i,j);N2ion(i,j);N4ion(i,j);H2Oion(i,j);H3O(i,j);H2O2(i,j);H2O3(i,j);H2O4(
i,j);H2O5(i,j)];

LCD=[LCDHeion(i,j);LCDHe2ion(i,j);LCDHem(i,j);LCDN2ion(i,j);LCDN4ion(i,j);LCDH2Oion(i,j);LC
DH3O(i,j);...
        LCDH2O2(i,j);LCDH2O3(i,j);LCDH2O4(i,j);LCDH2O5(i,j)];

    A=eye(11,11)-C3*dt;
   B=(n+D3*dt+LCD*dt);
   %Determine the error for convergence purposes
   if j>66 && j<600 && i<40 % only look where the densities are interesting
    An=A*n; % density weighted error, Lhs=Rhs==An=B
    cm=An-B;
    cp=An+B;
    err=abs(cm)./abs(cp).*n/sum(n);
    err=max(err);
    error=max(error,err);
   end
    n=A\B;

    Heion(i,j)=n(1);
```

```
        He2ion(i,j)=n(2);
        Hem(i,j)=n(3);
        N2ion(i,j)=n(4);
        N4ion(i,j)=n(5);
        H2Oion(i,j)=n(6);
        H3O(i,j)=n(7);
        H2O2(i,j)=n(8);
        H2O3(i,j)=n(9);
        H2O4(i,j)=n(10);
        H2O5(i,j)=n(11);
           end
end

% Put on the i=2 points near the origin by least-squares fitting to points
% i=3,4,5

j=2:Nx;
i=2;
        %Least squares fit to i=3,4, and 5
        Heion(i,j)=(18*Heion(i+1,j)+8*Heion(i+2,j)-7*Heion(i+3,j))/19;
        He2ion(i,j)=(18*He2ion(i+1,j)+8*He2ion(i+2,j)-7*He2ion(i+3,j))/19;
        N2ion(i,j)=(18*N2ion(i+1,j)+8*N2ion(i+2,j)-7*N2ion(i+3,j))/19;
        N4ion(i,j)=(18*N4ion(i+1,j)+8*N4ion(i+2,j)-7*N4ion(i+3,j))/19;
        H2Oion(i,j)=(18*H2Oion(i+1,j)+8*H2Oion(i+2,j)-7*H2Oion(i+3,j))/19;
        H3O(i,j)=(18*H3O(i+1,j)+8*H3O(i+2,j)-7*H3O(i+3,j))/19;
        H2O2(i,j)=(18*H2O2(i+1,j)+8*H2O2(i+2,j)-7*H2O2(i+3,j))/19;
        H2O3(i,j)=(18*H2O3(i+1,j)+8*H2O3(i+2,j)-7*H2O3(i+3,j))/19;
        H2O4(i,j)=(18*H2O4(i+1,j)+8*H2O4(i+2,j)-7*H2O4(i+3,j))/19;
        H2O5(i,j)=(18*H2O5(i+1,j)+8*H2O5(i+2,j)-7*H2O5(i+3,j))/19;
        % adjust the Hemnew data to a parabola near the origin
        Hem(i,j)=(18*Hem(i+1,j)+8*Hem(i+2,j)-7*Hem(i+3,j))/19;

    % return densities and keep them positive
a=abs(Heion);b=abs(He2ion);c=abs(Hem);d=abs(N2ion);ee=abs(N4ion);f=abs(H2Oion);g=abs(H3O);
h=abs(H2O2);k=abs(H2O3);l=abs(H2O4);m=abs(H2O5);

end
```